
UNIVERSIDAD DE GRANADA

DOCTORAL THESIS

# ANALYSIS OF THE BEHAVIOR OF IMPERMEABLE AND PERMEABLE BREAKWATERS

*Author:*
María Victoria Moragues Gómez

*Supervisor:*
María Clavero Gilabert

Doctoral Programme: Biogeochemical Fluid Dynamics and their Applications

Environmental Fluid Dynamics Research Group

Department of Structural Mechanics and Hydraulic Engineering
University of Granada

May, 2021

UNIVERSIDAD DE GRANADA

Dinámica Ambiental
UNIVERSIDAD DE GRANADA

DOCTORAL THESIS

# ANALYSIS OF THE BEHAVIOR OF IMPERMEABLE AND PERMEABLE BREAKWATERS

*Author:*
María Victoria Moragues Gómez

*Supervisors:*
María Clavero Gilabert

Doctoral Programme: Biogeochemical Fluid Dynamics and their Applications

Environmental Fluid Dynamics Research Group

Department of Structural Mechanics and Hydraulic Engineering
University of Granada

May, 2021

Editor: Universidad de Granada. Tesis Doctorales
Autor: María Victoria Moragues Gómez
ISBN: 978-84-1306-965-4
URI: http://hdl.handle.net/10481/69898

San Juan de Gaztelugatxe

Iskander Gutierrez (@iskandergg)

*"'What do you connect with the sea?' [...]*
*'With constant movement, she answered after a pause. With change.*
*And with riddles, with mystery, with something I cannot grasp,*
*which I might be able to describe in a thousand different ways, in a*
*thousand poems, never actually reaching the core, the heart of the*
*matter. Yes, thats it.' "*

*"- ¿Qué te sugiere el mar? [...]*
*- Eterno movimiento. - Respondió al cabo. - Cambio. Y misterio,*
*secretos, algo que no soy capaz de abarcar, que podría describir de mil*
*formas en mil versos sin alcanzar jamás su corazón. Su verdadero*
*ser. Sí, creo que eso. "*

Andrzej Sapkowski

*A mi ama y aita, por quererme y apoyarme*
*como solo unos padres pueden hacerlo.*

*A Miguel, por inspirarme y ayudarme cada día.*
*Un paso más juntos.*

*A Tábor y Auri, por su compañía incondicional*
*durante las largas jornadas de trabajo.*

***Asko maite zaituztet***.

# *Acknowledgements*

First of all, I would like to thank María Clavero, not only for being the advisor of this Thesis, because without her help and guidance it would not have been possible to complete, but also for being the one who introduced me to the laboratory during my Master Thesis and showed me the beauty of research.

I would also like to thank Miguel Ortega for his guidance during the first steps of this work as first advisor, having trusted me to do the Thesis and introducing me as part of the GDFA group.

This Thesis would not have been possible without the help of Miguel Losada, who with his patience, his proximity and dedication, has taught me to be curious and critical, to be patient, to read and write articles and, in short, to be a good researcher.

I would like to thank all my colleagues of the Environmental Fluid Dynamics Research Group of the University of Granada, both present and past, who in some way, have done their bit in this work by lending me their help; and especially María Jiménez with whom I have shared so many hours at the lab, and outside it, that, besides being colleagues, we have become almost sisters.

I would also like to thank Pedro Lomónaco for hosting me during my stay at Oregon State University and allowing me to participate in the projects carried out in the laboratory. I would also like to thank Meaghan Wengrove, Jack Puleo, Daniel Cox, Rusty Feagin and the rest of colleagues, for letting me take part in the NSF DUNE3 project.

Finally, I would like to thank my parents, to whom I dedicate this thesis, for all their motivation, unconditional support, affection and lots of love. Also to all my friends who, being near or thousands of miles away, have supported me all the way.

And of course, my biggest thanks to Miguel, for accompanying me during the whole process, from the initial tranquility, to the nerves and the final stress, for making me see things with perspective, for encouraging me to keep working or making me aware of the need to rest as well. Words will never be enough to express my gratitude and thanks.

This thesis has been done with funding provided by the research group TEP-209 (Junta de Andalucia) and the projects VIVALDI (BIA2015-65598- P), PROTOCOL (917PTE0538), SUSME (PCI2019-103565) and ROMPEOLAS (PID2019-107509GB-I00). I wish to acknowledge the mobility grant given by the Campus of International Excellence of the Sea (CEIMAR).

# *Abstract*

The main maritime structure used for the protection of ports and coasts are breakwaters. The different types of breakwaters appear mainly according to their way of dealing with the incident wave energy. Therefore, their design must be optimized to guarantee their operability and functionality at the lowest cost. The sloped rubblemound breakwater typology is the most used on the Spanish coasts mainly due to its great capacity to dissipate the incident energy. This dissipation occurs through several processes: by the vortex generated during wave breaking on the slope; by the turbulence generated inside the pores of the main armor; or by the turbulence generated within the porous medium of the core. Dissipation caused by porous medium is well described by the Forcheimer equation, however, dissipation caused by the breaking waves does not have an equivalent computational model. The use of the Iribarren number as a dynamic similarity parameter for the classification of breaker types is widely used and practically all formulations for the calculation of failure modes of sloped breakwaters are performed as a function of $Ir$. The results show that it is a good variable to describe the processes only for values $Ir < 1.5$, producing much scatter in the data thereafter. In this Thesis a new analysis of the breaker types has been carried out, identifying six typologies. This study has been subsequently used to study the flow characteristics (run-up and run-down) on different slopes. To achieve these objectives, experimental and numerical tests have been carried out, and data provided by other authors have been used.

First, the dimensionless variables on which the wave-structure interaction processes depend on smooth impermeable, impermeable with armor or permeable slopes were identified by means of dimensional analysis. Once the variables had been identified, tests were carried out on a 1:10 smooth and impermeable slope for the study of breaker typologies. In this way, only dissipation by breaking waves occurs and allows local quantification. The breakers identified were spilling, weak plunging, strong plunging, strong bore, weak bore and surging. An experimental space has been proposed, generated from the incident wave steepness and relative depth, allowing to quickly identify where the tests are located and what type of breaking they would have. As a product of both variables, an alternative similarity parameter, *chi*, has been formulated and the locations of the transitions between breaks in a 1:10 slope have been located.

Secondly, based on the dimensional analysis, the parameter $\chi$ has been proposed to describe the run-up and run-down in a smooth and impermeable slope. These characteristics are directly related to the types of breakage, as well as the mean water level in the slope, so to avoid the influence of the slope, the total water excursion $(Ru + |Rd|)$ has been proposed as a descriptor of the flow characteristics and has been directly related to the energy transformation ($D^*$ or $K_R$). This methodology has been employed for impermeable structures with a protective armor, the flow depending then on $\chi$ and the relative diameter of the mantle $(D_a/H)$; and for structures consisting of a porous core and a protective mantle, depending then also on the relative diameter of the core $(D_c/L)$.

Finally, throughout all the analyses, the flow characteristics have been related to the energy dissipation, proposing a global dimensionless coefficient $(B_S)$, as a function of incident wave train characteristics such as celerity, group celerity, wave height or period. This coefficient is directly dependent on $\chi$, namely, on the breaker types. When adding porosity, either in the armor or in the core, the defining variables $(D_a/H, D_c/L)$, also modify the values of $B_S$.

# *Resumen*

La principal estructura marítima empleada para la protección de puertos y costas son los diques de abrigo. Las diferentes tipologías de diques aparecen principalmente en función de su forma de tratar la energía del oleaje incidente. Por ello, su diseño debe estar optimizado para garantizar su operatividad y funcionalidad al menor coste. La tipología de dique en talud es la más empleada en las costas españolas debido principalmente a su gran capacidad para disipar dicha energía. Esta disipación ocurre a través de varios procesos: por los vortices generados durante la rotura del oleaje sobre el talud; por la turbulencia generada entre los huecos del manto principal; o por la turbulencia generada dentro del medio poroso del núcleo. La disipación causada por los medios porosos está bien descrita a través de la ecuación de Forcheimer, sin embargo, la disipación causada por rotura no tiene un modelo de cálculo equivalente. El uso del número de Iribarren como parámetro de similitud dinámica para la clasificación de los tipos de rotura está ampliamente extendido y prácticamente todas las formulaciones para el cálculo de los modos de fallo de los diques en talud se realiza en función de $Ir$. Los resultados muestran que es una buena variable para describir los procesos únicamente para valores $Ir < 1.5$, produciendo mucha dispersión de los datos a partir de ahí. En esta Tesis se ha realizado un nuevo análisis de los tipos de rotura, identificando seis tipologías. Este estudio se ha utilizado posteriormente para estudiar las características del flujo (run-up y run-down) sobre diferentes taludes. Para lograr estos objetivos se han realizado ensayos experimentales y numéricos, y se han utilizado datos proporcionados por otros autores.

En primer lugar, se han identificado, mediante análisis dimensional, las variables adimensionales de las que dependen los procesos de interacción ola-estructura sobre taludes lisos impermeables, impermeables con manto o permeables. Una vez identificadas las variables, para el estudio de las tipologías de roturas se han realizado ensayos sobre un talud 1:10 liso e impermeable. De esta manera solo se da la disipación por rotura y permite cuantificarla de forma local. Las roturas identificadas han sido spilling, weak plunging, strong plunging, strong bore, weak bore y surging. Se ha propuesto un espacio experimental, generado a partir del peralte del oleaje incidente y la profundidad relativa, permitiendo identificar rápidamente donde se encuentran localizados los ensayos y qué tipo de rotura tienen. Producto de ambas variables, se ha formulado un parámetro de similitud alternativo, $\chi$, y se han localizado donde se dan las transiciones entre las roturas en un talud 1:10.

En segundo lugar y basándose en el análisis dimensional, se ha propuesto el parámetro $\chi$ para describir el run-up y run-down en un talud liso e impermeable. Estas características están directamente relacionadas con los tipos de rotura, al igual que el nivel medio del agua en la pendiente, por lo que para evitar la influencia del mismo, se ha propuesto la excursión total de agua $(Ru + |Rd|)$ como descriptor de las características de flujo y se ha relacionado directamente con la transformación de la energía $(D^*$ o $K_R)$. Esta metodología se ha empleado para estructuras impermeables con manto de protección, dependiendo el flujo de $\chi$ y del diámetro relativo del manto $(D_a/H)$; y para estructuras formadas por un núcleo poroso y un manto de protección, dependiendo entonces también del diámetro relativo del núcleo $(D_c/L)$.

Por último, a lo largo de todos los análisis, se han relacionado las características de flujo con la disipación de la energía, proponiendo un coeficiente adimensional global ($B_S$), en función de las características del tren de onda incidente como la celeridad, la celeridad de grupo, la altura de ola o el período. Este coeficiente depende directamente de $\chi$, es decir, de los tipos de rotura. Al añadir porosidad, ya sea en el manto o en el núcleo, las variables que las definen ($D_a/H$, $D_c/L$), también modifican los valores de $B_S$.

# Contents

# List of Figures

# List of Tables

# 1 Introduction

*"Nobody wants to spend money to build a more resilient city because nobody owns the risk."*

Jeff Goodell

## 1.1 General overview

Coastal areas have been habitats for a great deal of human activity. Since the $20^{th}$ century, their use has increased dramatically and so has the population that inhabits them. Currently, around 40% of the world's population lives less than 100 km from the sea and according to the IPPC (2019), 23% of the total lives less than $100m$ above sea level. In the particular case of Spain, this percentage rises to almost 50% of the population. The progressive rise of the sea level, caused by climate change, makes the protection of these areas essential to prevent the displacement of millions of people.

The main structure to protect coastal areas, whether they are protected waters from a port or to prevent erosion of a beach, are breakwaters, capable of dissipating, reflecting or transmitting energy depending on their geometrical characteristics. According to Takahashi (1996), there are three main types of breakwaters: the sloped breakwater, characterized by its great energy dissipating capacity; the vertical breakwater, characterized by its great reflecting capacity (including the composite and horizontally composite subgroups); and the special types, the most common being the non-gravity ones such as pile, floating or pneumatic ones.

In Spain, the design, construction and maintenance of breakwaters is carried out following the guidelines set by the Recommendations for Maritime Works (ROM). The series includes recommendations for the calculation of structures, calculation of project actions, maritime climate atlas, geotechnical recommendations, etc. ROM 0.0-01 (2001) and ROM 1.1-18 (2018) are those related to the construction of breakwaters and their protection against marine dynamics.

FIGURE 1.1: Different run-up heights on a rubble mound breakwater with crown wall and overtopping due to a higher run-up.

According to ROM 0.0-01 (2001), in Spain the most commonly used type of breakwater is the sloped breakwater. Its main mission is to break the waves and therefore dissipate the energy of the incident wave train. The overall dissipation in the structure depends on the transport of turbulent kinetic energy (TKE) and comes from

different mechanisms at different scales: (1) from wave breaking that generates turbulent vortices whose scale depends on the type of breaking, (2) by friction generated by the main and secondary armors, whose scale is related to the size of the armor pieces and their thickness, and (3) in the porous core, whose scale depends on the grain size.

The Forchheimer equation provides information on local dissipation in the porous medium, both in the amor and in the core, through the Reynolds and Keulegan-Carpenter numbers (Van Gent, 1995). However, the dissipation produced by shoaling and eventual wave breaking does not have an equivalent theoretical model, making it impossible to calculate local dissipation. In general, the dissipation calculation is performed through the energy conservation equation, calculating the global dissipation coefficient.

The variability found at both the wave and state levels are directly related to the wave transformation processes in its propagation on the slope. These processes can be adequately calculated in a control volume since their values are interdependent, but their values are not, in general, in local equilibrium, and the dissipative processes can be substantially modified, affecting the flow characteristics, as well as the rest of the failure modes. When a wave train interacts with a breakwater, its behavior depends on the transformation process that dominates the spatio-temporal evolution of the wave train that propagates onto the slope and porous core. These modes of wave-train transformation and their related breaker types are the following: (1) dissipative mode typical of spilling breakers; (2) reflective mode for surging breakers; and (3) transitional modes.

The interdependence of the reflection and the dissipative processes (the slope reflects the energy that is not dissipated) causes the irregular regime of water flow along the slope, in particular of its maximum values, i.e., run-up. This is why the most correct way to deal with this variability is to analyze its causes and then describe it using statistical techniques. With this tool, the uncertainty can be bounded and the risk due to run-up and potential overtopping can be quantified.

On the other hand, according to the most advanced technical guidelines, the breakwaters must be designed and projected under a dual optimization system: technical-economic of the work subject to safety and operability requirements, and economic-financial investment subject to a sensitivity analysis and an acceptable level of risk (Figure 1.2). To meet this requirement, it is necessary to analyze and design the work as a set, a vision that is not currently available since each mode of failure of the work is studied independently. Battjes (1974) proposed using the Iribarren number (Iribarren and Nogales, 1949) , $Ir = tan\alpha/\sqrt{H/L}$, as the dynamic similarity parameter to analyze wave train behavior on an indefinite impermeable flat slope, slope angle $\alpha$, where $L$ is the characteristic wavelength. He also conjectured that the value of $Ir$ identified breaker type as spilling, plunging, collapsing, or surging.

Since Battjes (1974), the research carried out in order to propose formulas for wave run-up, run-down, overtopping and stability of the main armor layer (Bruun and Günbak, 1977b; Losada and Giménez-Curto, 1981; Zanuttigh and Meer, 2008; Burcharth et al., 2010; Gómez-Martín and Medina, 2014; Vílchez et al., 2016b) show that in the domain $Ir > 1.5$, the Iribarren number reveals the general tendency of reflection and transmission coefficients. However, the values tend to scatter as the value of $Ir$ increases, depending on the slope angle.

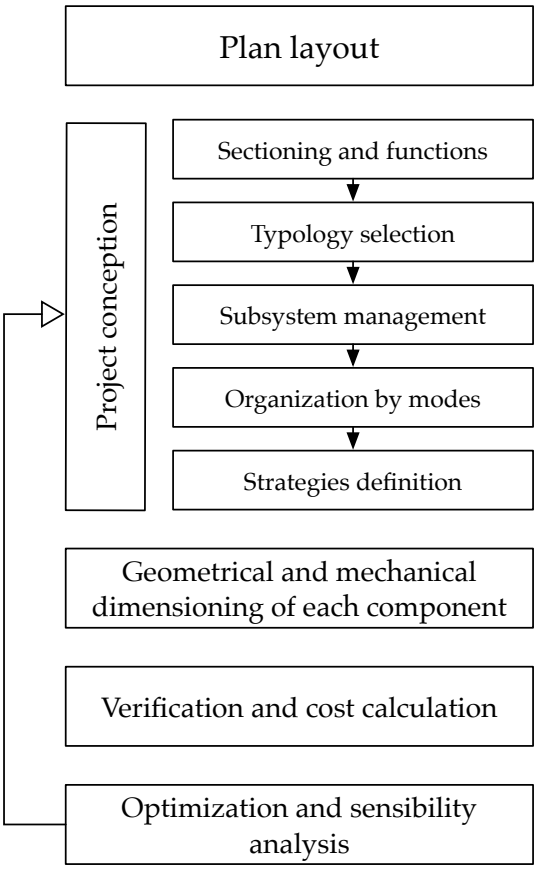


FIGURE 1.2: General sequence for the conception and design of a breakwater (Adapted from ROM (1.1-18, 2018)).

In addition, due to the randomness of the flow design parameters as well as the wave parameters, the use of statistical parameters (Mase, 1989) and their subsequent fitting to experimental functions was proposed depending on the wave and breakwater characteristics. In general, most of the formulations use the Iribarren number (Iribarren and Nogales, 1949) as the main variable. As a result, different experimental techniques are found for each laboratory, as well as a variability not useful for practical engineering. To overcome the uncertainty, in recent years, the use of fitting functions and the incorporation of partial fit coefficients, which quantify the statistical variability with a representative value, have been emphasized. This variability must be bounded by knowing and evaluating turbulent dynamics both locally and globally. This is the only way to (1) design breakwaters with less uncertainty and delimit the risk, (2) verify whether or not the current breakwaters are oversized, and (3) develop new design concepts for both new construction and repair of the breakwater.

## Environmental Fluid Dynamics Research Group (GDFA) background

The Environmental Flow Dynamics group at the University of Granada has been studying and analyzing the behavior of breakwaters for many years.

López (1998) analyzed the influence of reflection processes on the stability of a slope breakwater. Benedicto (2004) analyzed the influence of the main and secondary layers in the bulk dissipation and analyzed the stability of rubble mound breakwaters. She concluded that knowledge of reflection processes allows designing experiments as well as relating stability to wave action. These results were used by Clavero (2007) to characterize the overtopping on a sloped breakwater, relating it to dissipation processes. In addition, Clavero (2007) proposed a joint methodology of three failure modes ascribed to ultimate limit state of a sloped breakwater and calculated the joint failure probability in the case of mutually exclusive modes.

Pérez-Romero (2008) analyzed the flow resistance in a vertical porous breakwater, as well as the laws of pressures and suppressions on a mixed breakwater. Pérez-Romero et al. (2009) and Clavero et al. (2012) certified that the 1D scattering parameter $B/L$ controls the wave propagation inside the porous medium (Dalrymple et al., 1991). As the time passes, the porous material inside the core saturates, increasing its dissipation and decreasing the reflection. This behaviour depends on the relative with of the core $B/L$ (Requejo et al., 2002) and its relative diameter $D_{n50,c}/L$ (Pérez-Romero et al., 2009). However, for breakwaters consisting of different parts and units, it is more convenient to define a $2D$ scattering parameter, $A_{eq}/L^2$, where $A_{eq}$ is the area per unit section under the S.W.L. (Vílchez et al., 2016b).

Pérez-Romero et al. (2009) and Vílchez et al. (2016a) proved that the flow regime inside the porous medium depends on the breakwater type and geometry, mainly on the relative diameter of the granular material, $Dk$, where $D$ is the diameter and $k = 2\pi/L$ is the wave number.

Vílchez (2016) studied 6 typologies of breakwaters (vertical, sloped and mixed) to study their hydrodynamic behavior. Her experiments confirmed that it depends on the dimensions and properties of each part of the breakwater. She proposed the

2D scattering parameter as the main variable to unify the calculations. She also developed a formula for the theoretical estimation of the total wave height in front of the structure as a function of the energy transformation. Vílchez et al. (2016b) established the relation between the cause (incident wave train) and the effect (oscillation in front of the breakwater depending on the interaction wave-breakwater), so that any response of the breakwater (overtopping, stability...) can be identified as a function of the cause. All the non-dimensional monomia that influence the interaction wave-breakwater were identified on a parametric map.

Díaz-Carrasco (2020), using dimensional analysis for impermeable and permeable structures, proposed the variables on which the energy transformation depends as a function of the wave and breakwater characteristics, demonstrating that the Iribarren number is not a dynamic similarity parameter. Clavero et al. (2020) concluded that the bulk dissipation depends on the product of the relative water depth and the incident wave steepness, the relative size of the armor diameter, the relative thickness, the shape and specific placement criterion, the characteristics of the porous core and the slope angle of the breakwater.

All these works are a basis and a starting point for this thesis.

## 1.2 Objectives

The main objective of this thesis is to find a methodology for the integrated analysis of the processes occurring in the wave-structure interaction in a sloped breakwater. These specific processes are the energy transformation, specifically the dissipation, and the flow characteristics, run-up and run-down. To achieve this objective, the maritime infrastructure must be studied as a complex system with different and simultaneous failure modes. Nowadays, design methods are developed under the hypothesis that there is spatial and temporal independence between failure modes. Henceforth, there is a lack of knowledge in the development and application of design methods based on the simultaneity of failure modes.

In order to achieve this objective, the following specific objectives have been defined:

1. To apply dimensional analysis in a global way to obtain all the variables on which the hydraulic performance of the breakwater depends, on impermeable and permeable structures.
2. To analyze the breaking processes on a smooth and impermeable slope to avoid dissipation in porous media and use the dimensionless variables identified in the dimensional analysis to identify and classify them.
3. To study the prevalence and progression of each breaker type and link them to the most common used experimental techniques and derive a bulk dissipation coefficient that depends on the types of breaking and is able to characterize them.
4. To study the flow characteristics (run-up, run-down and total excursion) on a smooth impermeable slope, estimating the local dissipation caused only by the breaking waves.

5. To analyze the flow characteristics on armored impermeable slope and permeable slopes depending on the non-dimensional variables obtained from the dimensional analysis, and to find the parameters on which the dissipation depends for each type of structure.

## 1.3 Thesis outline

From the next Chapter, this Thesis is organized as follows:

In Chapter 2, after a description of the processes involved in the wave-structure interaction, a global dimensional analysis is performed using the Buckingham's $\pi$-Theorem. The instantaneous dimensionless variables on which the flow characteristics depend, are identified for each type of structure: smooth impermeable slope, armored impermeable slope or permeable slope.

Chapter 3 presents the analysis of the breaking types, presenting new physical experiments on a 1:10 impermeable slope and previously done physical tests; and identifies the parameter to identify them.

The following, Chapter 4, analyzes the progression of the breaker types and evaluate the different experimental techniques most commonly used in laboratories.

Chapter 5 evaluates the flow characteristics on an impermeable smooth slope, where the dissipation only occurs due to wave breaking. A sigmoid function has been fitted to the data, so as to be capable of predicting the total water excursion as a function of the bulk dissipation, or viceversa.

In the same way, Chapter 6 studies the flow characteristics in an armored impermeable slope. The run-up values are defined depending on the breaker types and the characteristics of the main armor. A sigmoid function has been fitted to both parameters.

Chapter 7 does the same for an armored permeable slope, taking into account the characteristics of the core. A bulk dissipation coefficient is presented depending on the incident characteristics of the wave train.

Lastly, in Chapter 8 the main conclusion of the Thesis and some future research lines are presented.

## 1.4 Publications derived from this thesis

The work done throughout this thesis has resulted in the following publications:

**Journal Papers**

- Díaz-Carrasco, P.; **Moragues, M.V.** ; Clavero, M. and Losada, M.A. "2D water-wave interaction with permeable and impermeable slopes: dimensional analysis and experimental overview". In: Coastal Engineering, Volume 158, 2020, 103682.

- **Moragues, M.V.**; Clavero, M. and Losada, M.A. "Wave breaker types on a smooth and impermeable 1:10 slope". In: Journal of Marine Science and Engineering, 2020, 8(4), 296.
- **Moragues, M.V.**; and Losada, M.A. "Progression of Wave Breaker Types on a Plane Impermeable Slope, Depending on Experimental Design". In: Journal of Geophysical Research - Oceans, 2021, 126, e2021JC017211.
- Losada M.A.; **Moragues, M.V.**; and Clavero, M. (2021). "Flow characteristics on steep, plane and impermeable slopes and beaches. The dependence on the alternate slope similarity parameter and relative wave height: $\chi$ and $\gamma$". Submitted to: Journal of Geophysical Research - Oceans.

**International Conferences**

- Díaz-Carrasco, P., **Moragues, M.V.**, Clavero, M., M. Ortega-Sánchez,M. and Losada M.A. (2017). "Wave overtopping on mixed breakwaters and design curves". In: Proceedings of the 8th International Conference on Applied Coastal Research. Santander, Spain. (Díaz-Carrasco et al., 2017)
- Díaz-Carrasco, P., **Moragues, M.V.**, Clavero, M., Ortega-Sánchez, M. and Losada M.A. (2018). "Similarity on rubble mound breakwaters tests: analysis and discussion". In: Proceedings of the 7th International Conference of the Application of Physical Modelling in Coastal and Port Engineering and Science. Santander, Spain.
- Folgueras, P., del Rosal, J., **Moragues, M.V.**, López, J.D.., and Losada M.A. (2018). "Accumulated damage evolution and investment costs of breakwaters". In: Proceedings of the 36th International Conference in Coastal Engineering. Baltimore, USA. (Folgueras et al., 2018)
- **Moragues, M.V.**, Díaz-Carrasco, P., Clavero, M., Ortega-Sánchez, M. and Losada M.A. (2019). "Climate change impact on the hydraulic performance of breakwaters". In: Proceedings of the 38th International Association for Hydro - Environment Engineering and Research World Congress. Panama City, Panama. (Moragues et al., 2019a)
- **Moragues, M.V.**, Clavero, M., Díaz-Carrasco, P., and Losada M.A. (2020). "Bulk dissipation and flow characteristics in cube armored breakwaters". In: Proceedings of the virtual International Conference in Coastal Engineering (vICCE). (Moragues et al., 2020a)

**National Conferences**

- **Moragues, M.V.**, P. Díaz-Carrasco, P., Clavero, M., Ortega-Sánchez, M. and Losada M.A. (2018). "Análisis del rebase sobre diques de abrigo". In: III Congreso transfronterizo sobre el Cambio Climático y Litoral - UHINAK. Irún, Spain. (Moragues et al., 2018)
- **Moragues, M.V.**, P. Díaz-Carrasco, P., Clavero, M. and Ortega-Sánchez, M. (2018). "Efecto de la subida del nivel del mar en la estabilidad y rebase de los diques de abrigo". In: Congreso de Jóvenes Investigadores del Mar. Cádiz, Spain.
- **Moragues, M.V.**, P. Díaz-Carrasco, P., Clavero, M. and Losada M.A. (2019). "Sobre el máximo remonte y rebase potencial en los diques rompeolas". In:

Proceedings of the 15th National Conference of Jornadas Españolas de Puertos y Costas. Málaga, Spain. (Moragues et al., 2019b)

- Díaz-Carrasco, P., **Moragues, M.V.**, Clavero, M. and Losada M.A. (2019). "Semejanza dinámica de los diques en talud: 2D re-análisis". In: Proceedings of the 15th National Conference of Jornadas Españolas de Puertos y Costas. Málaga, Spain.
- Losada, M.A., Díaz-Carrasco, P., **Moragues, M.V.**, Clavero M. (2019). "Variabilidad intrínseca en el comportamiento de los diques rompeolas". In: Proceedings of the 15th National Conference of Jornadas Españolas de Puertos y Costas. Málaga, Spain. (Losada et al., 2019)

**Other publications**

- Innocenti, R.A., Feagin R.A.; Charbonneau, B.R.; Figlus, J.; Lomónaco, P.; Wengrove, M.; Puleo, J.; Huff, T.P.; Rafati, Y.; Hsu, T.J.; **Moragues, M.V.**; Tsai, B.; Boutton, T.; Pontiki, M. and Smith, J. (2021) "The effects of plant structure and fluid properties on the physical response of coastal foredune plants to wind and wave run-up". In: Estuarine, Coastal and Shelf Science (Under review YECSS-D-20-00341)

# 2 Dimensional Analysis: Buckingham's $\pi-$Theorem

**Comment**

All the variables are defined in the Nomeclature section.

*"Scientists investigate that which already is; Engineers create that which has never been."*

Albert Einstein

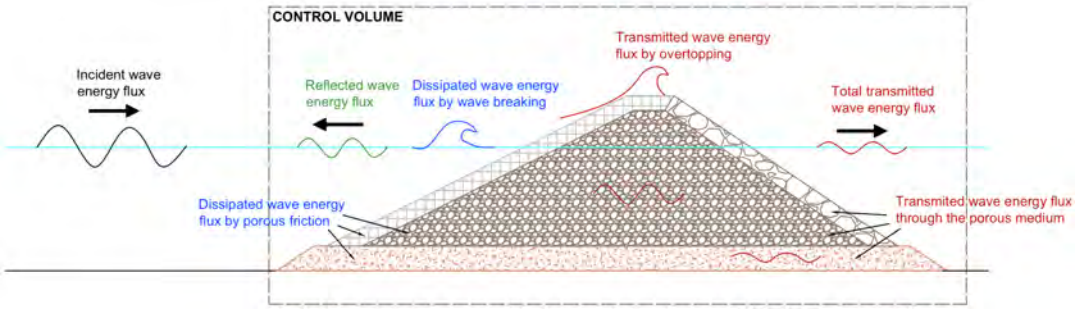


FIGURE 2.1: Scheme of the wave energy distribution in the wave-structure interaction.

Sloped breakwaters are the most common structure for coastal protection due to their ability to transform the incident wave energy into (a) reflected energy and returned to the sea, (b) through the breakwater (if it is permeable), or over the breakwater (if it is overtoppable), spreading to landward side; (c) energy that is global dissipated and thus extinguished and (d) energy transferred to other oscillatory modes (0.0-01, 2001; 1.1-18, 2018).

The input and output energy fluxes and the dissipation processes (Figure 2.1), if evaluated inside a control volume of one unit of width, can analyze the energy transformation through the energy conservation equation (Equation 2.1) when linear theory is applied and the energy to higher harmonics is considered negligible (Losada et al., 1997).

$$F_I - F_R - F_T - D'_* = 0 \tag{2.1}$$

where $F_I$, $F_R$ and $F_T$ represent the incident, reflected and transmitted energy fluxes respectively, and $D'_*$ evaluates the dissipation per time unit inside the control volume (Equation 2.2). $i = I, R, T$ represents the energy flux. $E_i$ is the total mean energy (kinetic and potential), per unit of horizontal surface of the wave train.

$$F_i = E_i C_{g,i} = \frac{1}{8}\rho_w g H_i^2 C_{g,i} \tag{2.2}$$

The energy propagation velocity of the wave movement ($C_g$) can be calculated through the phase velocity ($C$) and the wave number ($k$).

$$C_{g,i} = \frac{1}{2} C_i \left(1 + \frac{2k_i h}{sinh(2k_i h)}\right) \tag{2.3}$$

The phase velocity can be estimated as $C_i = L_i/T_{z,i} = \sigma_i/k_i$. The wave number ($k_i = 2\pi/L_i$) and the water depth ($h$) are related to the angular frequency ($\sigma_i = 2\pi/T_z$) by means of the dispersion equation.

$$\sigma_i^2 = g k_i tanh(k_i h) \tag{2.4}$$

The energy conservation equation inside the control volumen can be written as a function of the reflection ($K_R = H_R/H_I$), transmission ($K_T = H_T/H_I$) and dissipation ($D^* = D'_*/(1/8\rho_w g H_I^2 C_g)$) coefficients.

$$K_R^2 + K_T^2 + D^* = 1 \tag{2.5}$$

Usually, the estimation of the bulk dissipation coefficient is performed globally using Equation 2.5 since the reflection and transmission coefficients can be calculated by free surface measurements with two or more sensors (Goda and Suzuki, 1976; Mansard and Funke, 1980; Hughes, 1993; Lin and Huang, 2004).

The three main processes involved in the wave - strucutre interaction in a non-overtoppable breakwater, reflection, transmission and dissipation, can be determined globally in a control volume. Their values are interdependent, but locally, they may not be in equilibrium. The wave train reflects and dissipates locally during its propagation along the slope, main and secondary mantles, core and when leaving the section.

The bulk dissipation of the incident wave train propagating on permeable slope depends, among other things, on the transport of turbulent kinetic energy (TKE) from the following sources: (a) wave breaking causing advection and diffusion of turbulence, generating a vortex dependent on the breaking type; (b) the armor layer whose vortex depends on the characteristic diameter of the armor unit; and (c) the porous core whose turbulence scale depends on the grain size.

Based on this background, it is concluded that the hydraulic performance of a breakwater and its wave regime resulted from the interacction between an incident wave train and the structure depends on the breakwater typology, its geometrical characteristics, the granular material and the incoming wave train characteristics.

The Darcy-Frocheimer equation (Equation 2.6) is generally used for estimating the flow resistance force inside the porous medium (Sollitt and Cross, 1972; Dalrymple et al., 1991; Van Gent, 1995). This equation includes a linear term representing the laminar flow, a non-linear term representing the turbulent flow and an inertial term accounting for the added mass effect due to transient effects.

$$F_{NL} = aun + bu|u|n^2 + c_A \frac{d(un)}{dt} \tag{2.6}$$

Where $u$ is the velocity through the voids, $n$ is the porosity and $a, b$ and $C_A$ are local coefficients.

The 1D scattering parameter $B/L$ controls the wave propagation in the porous medium (Dalrymple et al., 1991; Pérez-Romero et al., 2009; Clavero et al., 2012). As the experiment progresses, the reflection inside the core decreases, increasing dissipation as the porous material becomes saturated. This behavior depends on the relative width of the core, $B/L$ (Requejo et al., 2002) and its relative diameter, $D_{n50,c}/L$ (Pérez-Romero et al., 2009). However, for breakwaters consisting of different parts and units, it is more convenient to define a 2D scattering parameter, $A_{eq}/L^2$, where $A_{eq}$ is the area per unit section under the S.W.L. (Vílchez et al., 2016b).

As proved by Pérez-Romero et al. (2009) and Vílchez et al. (2016a), the flow regime inside the porous medium depends on the breakwater type and geometry, mainly on the relative diameter of the granular material, $Dk$, where $D$ is the diameter and $k = 2\pi/L$ is the wave number.

The influence of the frictional resistance forces ($f_L$, laminar, $f_T$, turbulent and $f_I$, intertial) changes the flow inside the porous medium. This influence can be analyzed through the non-dimensional parameters Reynolds number, $Re = UD/\nu$, being $U$ the volume-average ensemble-average velocity and $\nu$ the kinematic viscosity; and Keaulegan-Carpenter number, $KC_p = UT/D$, being $T$ the wave period. Burcharth and Andersen (1995) identified 4 hydraulic flow regimes, depending on the Reynolds number: (1) Darcy flow regime ($Re < 1$), (2) Forchheimer flow regime ($1 < Re < 150$), (3) Transitional flow regime ($150 < Re < 300$), and (4) Fully turbulent flow regime ($Re > 300$). Usually, in breakwaters the flow is fully turbulent and the effect of $Re$ and $KC_p$ can be neglected.

In summary, with laboratory measurements, the reflection and global transmission in a vertical porous medium can be accurately calculated. By applying the potential theory of the porous medium (Forchheimer equation and the Lorentz equivalent work conjecture), numerical methods and collection in specific laboratory experiments, the main monomials that determine the local dissipation and reflection, $h/L$, $A_{eq}/L^2$, $D_p/L$, $R_{e,Dp}$, $H/D_p$, $n_p$, i.e. relative depth, area and diameter, Reynolds numbers and grain KC and porosity, have been identified. From this data, the overall dissipation is estimated reasonably well.

However, there is no equivalent to estimate the local dissipation due to wave breaking processes. Despite the numerous studies done in the recents years (numerical and physical), the main parameter to study the wave breaking remains to be the Iribarren number (Iribarren and Nogales, 1949) or surf similarity parameter (Battjes, 1974).

The objective of this research is to apply the method of dimensional analysis to reduce the number of experimental variables affecting the wave-slope interaction and to improve the scalability of the results. Furthermore, to correlate those variables with the outputs of the experimental tests, namely the flow characteristics (run-up, run-down and mean water level) and the transformation of the incident wave energy flux (reflected and transmitted flux) . Although the application is general it is developed specifically for three different natural or man-made sloping coastal structures: (1) a flat impermeable slope with smooth and rough surface; (2) a rock and armor layer over a flat impermeable slope; (3) a rock and armor sloping layer over a permeable core of finite width. All the slopes are non-overtoppable and there is not a toe berm.

The hydrodynamic performance of each of the structures depends on (1) the incoming wave train; and (2) their geometry and the characteristics of the materials. It can be evaluated applying the three conservation equations, mass, momentum and energy in a Control Volume which includes the structure.

Because the flow characteristics are related with the evolution of wave breaker types breaking on the slope and the overall energy dissipation (Moragues et al., 2020b; Moragues and Losada, 2021), the application of the method of dimensional analysis is inspired by the energy conservation equation of the the incident, reflected and transmitted of wave energy fluxes and the overall energy dissipation rate.

## 2.1 Buckingham's $\pi-$Theorem

In order to describe the phenomena that surround us, it is necessary to first determine the magnitudes that can be useful, those that have a primordial in-flow in their development; then we are interested in knowing relationships between them or laws.

The dynamic similarity between two systems, that only differ in a scale factor of their measures, is defined as the condition that leads to determine the mechanical behavior of one of the systems under certain conditions, knowing the values of the properties of the other. In experimental fluid mechanics, one system is known as a prototype, which will go into operation, and the other is the scaled model.

It is possible to ensure dynamic similarity between two systems if they share the equality in value of certain dimensional factors, for example Reynolds' number, Froude's number, etc. Among the benefits of knowing their values is:

- Ensure dynamic similarity.
- Simplify the mathematical expressions that relate the magnitudes at stake by taking limiting cases.
- The summary presentation of the experimental data.

There are two practical cases where these dimensional factors can be obtained:

- Dividing the terms of the equation or equations, which govern the dynamic behavior of the system by an appropriate dimensional factor, in such a way that it leaves them non-dimensional. In this case, it is necessary to know the mathematical models, boundary conditions or even the constitutive equations that describe the particular physical situation.
- If the equations are not known, very common in research, these non-dimensional factors can be obtained through a dimensional analysis.

The Buckingham $\pi-$Theorem (Buckingham, 1914) is the fundamental theorem of dimensional analysis. This theorem provides a method of constructing dimensionless parameters, even when the form of the equation is unknown, although the choice of dimensionless parameters is not unique and the theorem does not provide information on which are more suitable. Therefore, there is an ambivalence in what these new parameters are $\Pi$.

In addition to the construction of the dimensionless parameters, this theorem states that any physical law is independent of the system of units in which it is expressed.

The theorem states that if $q_1, q_2, , q_n$ are $n$ physical magnitudes or variables involved in a particular problem and if between them exists a functional relationship of form:

$$f(q_1, q_2, , q_n) = 0 \tag{2.7}$$

And if those variables are expressed in terms of $k$ quantities belonging to the fundamental magnitudes (length, mass and time) then the original equation can be written equivalently as an equation with a series of $n-k$ non-dimensional numbers constructed with the original variables.

Each non-dimensional variable is called $\Pi$ o non-dimensional factor. The symbol $\Pi$ is used due to the non-dimensional variables can be written as a product of the variables $q_1, q_2, , q_n$ elevated to some power. So, Equation 2.7 can be written as the functional relationship:

$$\phi(\Pi_1, \Pi_2, ..., \Pi_{n-k}) = 0 \tag{2.8}$$

The equation that allows to calculate these $\Pi_n$, is:

$$\Pi_i = V_{Di} \prod_{j=1}^{k} V_{Fj}^{aj} \tag{2.9}$$

$$\text{with: } i = 1, 2, ..., n-k$$

Where $V_D$ are the physical variables relevant for the problem, $V_F$ are the dynamic variables that act as fundamental variables (repeated variables) and $a_j$ are chosen in such a way that each $\Pi_i$ is dimensionless. Finally, a relationship can be established between the $\Pi_i$, of the form:

$$\Pi_0 = f(\Pi_1, \Pi_1, ..., \Pi_{n-k}) \tag{2.10}$$

The arbitrary way of choosing the repeated variables leads to different sets of dimensionless factors; however, in each case $n-k$ are independent and in the words of the linear algebra, they form a complete set.

## 2.2 Flat impermeable slope with smooth and rough (fixed) surface

The principal variables that intervene in the transformation of the wave-slope interaction are: (1) slope angle, $\alpha$; (2) water depth at the toe of the slope, $h$; (3) incident wave height, $H_I$, and (4) wave period, $T_Z$, (or wave length, $L$); (5) gravity acceleration, $g$; (6) dynamic viscosity, $\mu_w$; (7) water density, $\rho_w$; (8) surface tension, $\tau_w$; (9) density of the slope material, $\rho_s$; and (10) equivalent roughness (or sand grain size) of the bed, $k_N$.

Regarding that the effect of water compressibility is negligible, a complete set of independent variables that govern the incident wave transformation over the slope is:

$$X = f\left(g, \rho_w, \mu_w, h, L, H_I, \tau_s, \rho_s, k_N\right) \tag{2.11}$$

where $X = (X_1, X_2, ...X_q)$ are $q$ dependent variables output of the experiment, some of them are measured, like $Ru$ and $Rd$ (run up and run down over the slope). Others are derived quantities, first and second kind, defined and calculated from the records, like the wave height of the reflected wave train $(H_R)$, and the dissipation rate applying the conservation energy equation, respectively. The slope angle $(\alpha)$ is not included in the set complete set of independent quantities. The experimental design for a given slope is carried on in test series, and the calculated functional relationships between input and output variables are specific of a given experimental slope.

Thus, the complete set has $n = 9$ independent quantities, and can be split in two subsets of independent quantities. The first one, $n_F = 5$, $(\rho_w, g, h, L, \tau_s)$. Accordingly, $(\rho_w, g, L)$, $k_F = 3$, is a complete subset of dimensionally independent quantities, and the dimensionless independent quantities are $n_F - k_F = 2$: $(h/L, \tau_s/\rho_w g L^2)$. Then, the original complete set can be reduced to $n - (n_F - k_F) = 7$ independent quantities:

$$X = f\left(\mu_w, H_I, \rho_s, k_N, \rho_w, g, L\right) \tag{2.12}$$

A complete subset of dimensionally independent quantities is $k = 3$, $(\tau_w, H_I, \rho_s)$, and the set of dimensionless independent quantities are $nk - (n_F - k_F) = 4$:

$$X = f\left(\frac{L}{H_I}, \frac{k_N}{H_I}, Re, \frac{\rho_w}{\rho_s}\right) \tag{2.13}$$

Accordingly, the observed experimental non-dimensional magnitudes are:

$$\frac{X}{H_I} = \left(\frac{Ru}{H_I}, \frac{Rd}{H_I}, \frac{\eta_m}{H_I}\right) \tag{2.14}$$

Gathering all the previous results:

$$\frac{X}{H_I} = f\left(\frac{Ru}{H_I}, \frac{Rd}{H_I}, \frac{\eta_m}{H_I}\right) = \left(\frac{L}{H_I}, \frac{k_N}{H_I}, Re, \frac{h}{L}, \frac{\tau_s}{\rho_w g L^2}, \frac{\rho_S}{\rho_w}\right) \tag{2.15}$$

If a characteristics amplitude $a_b$ is computed at the toe of the slope,

$$a_b = \frac{H_I}{2sinh\frac{2\pi h}{L}} \tag{2.16}$$

the Reynolds number determine the experimental hydrodynamic regime and is defined at the toe of the slope,

$$Re = \frac{2\pi}{T}\frac{a_b^2}{\nu_w} = \frac{\pi}{2T}\frac{H_I}{\nu_w\left(sinh\frac{2\pi h}{L}\right)^2} \tag{2.17}$$

being $\nu_w = \mu_w/\rho_w$ the kinematic viscosity of the water. To avoid scale effects, the value of this Reynold's number must be $Re > 10^4$.

The wave energy conservation equation is formulated in a Control Volume, (CV), extending landwards from the toe of the slope to the shoreline: the spatial variation in the CV of the time-averaged wave energy fluxes is equal to the amount of wave-averaged energy dissipated per unit area, $(D^*)_{CV}(J/m^2s)$, in the CV (Baquerizo et al., 1998).

$$(F_I - F_R)_x + (D^*)_{CV} = 0 \tag{2.18}$$

where $F = EC_g = EC_n = E\omega kf(kh)$ $(J/ms)$, is the time-averaged wave energy flux per unit surface at the toe of slope,

$x_{toe}$, and the subindexes $I$ and $R$ denote the incident and the reflective wave train, respectively. Only the energy of the most progressive incident and reflective wave trains were considered. The equation can be expressed in non-dimensional quantities,

$$1 - K_R^2 + d^* = 0 \tag{2.19}$$

where $K_R^2$ is the module of the reflection coefficient for the most progressive mode in the wave train, defined as the quotient of the reflected and incident wave energy fluxes per unit surface area, and $d^*$ is the non-dimensional energy dissipation rate. $(D^*)_{CV}$ can be split in two parts: (1) due to the wave breaking process and the production and dissipation of turbulence; (2) bed friction in the wave boundary layer developed by the up- and dowh-rush flow over the slope. If the bed particle can be transported, then the wave energy dissipation rate over the slope (Bagnold and Taylor, 1946) has to be considered. Herein, the case of smooth and rough fixed bed is considered. Thus the relative particle density $(\rho_s/\rho_w)$ can be discarded.

Furthermore, herein the relative roughness of the bed of this geometry of slope is small $(k_N/H_I < 0.1)$. Kamphuis (1975) showed that on an horizontal or midly sloped sandy bottom the friction factor, $f_e \approx (k_N/a_b)^{3/4}$, and the time-averaged rate of wave energy dissipation due to bed friction is given by Jonsson (1966):

$$d_{bs} \approx \frac{2}{3\pi}\rho_w f_e \left(a_b \frac{2\pi}{T}\right)^3 \tag{2.20}$$

where $a_b$ is the amplitude of the water particle excursion parallel to the bed outside the boundary layer. The nondimensional parameter $(k_N/a_B)$ is related to the non-dimensional quantity:

$$\frac{k_N}{a_b} = 2sinh\left(\frac{2\pi h}{L}\right)\frac{k_N}{H_I} \tag{2.21}$$

This term is almost negligible in comparison to the dissipation by breaking for weak and strong plunging. However, it starts to be significative for strong and weak bore and surging breaker types. That is for wave energy transformation which strongly depends on the wave reflection process on the slope. Under such conditions the dependence of the relative run-up and run-down on the relative roughness of the bed, $k_N/a_b$, cannot be ignored.

Finally, if the surface tension term is negligible ( $10^{-6}$), the bed is fixed and the Reynolds number is ($Re > 10^4$), for each slope angle the following functional relationship is obtained:

$$\left(\frac{Ru}{H_I}, \frac{Rd}{H_I}, \frac{\eta_m}{H_I}\right) = f_\alpha\left(\frac{H_I}{L}, \frac{h}{L}, 2sinh\left(\frac{2\pi h}{L}\right)\frac{k_N}{H_I}\right) \tag{2.22}$$

## 2.3 An armor layer over a flat impermeable slope

In addition to the given principal variables that intervene in the above impermeable slope, the actual transformation of the wave-slope interaction depends also on: (11) a characteristic of the rock (or amor unit) diameter $D_{a,n50}$, and (12) layer thickness, $e$, which usually is calculated as proportional to the rock diameter. A complete set of independent variables that govern the incident wave transformation over the slope is:

$$X = f\left(g, \rho_w, \mu_w, h, L, H_I, \tau_s, \rho_s, e, D_{a,n50}\right) \tag{2.23}$$

For this sloping structure, the dependent variables of the experiment are determined according to $n = 10$ independent variables. Again, the complete set can be split in two subsets of independent quantities. The first one, with $n_F = 5$, is formed by $(\rho_w, g, h, L, \tau_s)$. Accordingly, $(\rho_w, g, L)$, with $k_F = 3$, is a complete subset of the dimensionally independent quantities, and the dimensionalness independent quantities are $n_F - k_F = 2$: $(h/L, \tau_s/\rho_w g L^2)$. Then, the original complete set can be reduced to $n - (n_F - k_F) = 8$ independent quantities:

$$X = f\left(\mu_w, H_I, \rho_s, e, D_{a,n50}, \rho_w, g, L\right) \tag{2.24}$$

A complete subset of dimensionally independent quantities is $k = 3$: $(\mu_w, H_I, \rho_s)$, and the set of dimensionless independent quantities are $nk - (n_F - k_F) = 5$:

$$\frac{X}{H_I} = f\left(\frac{D_{a,n50}}{H_I}, \frac{L}{H_I}, \frac{\rho_s}{\rho_w}, Re, Re_p\right) \tag{2.25}$$

where $Re_p$ is the pore size based Reynolds number, which evaluates the wave energy damping due to percolation and viscous.

$$Re_p = \frac{\pi e}{n_e T}\frac{H_I}{\nu_w\left(sinh\frac{2\pi h}{L}\right)} \tag{2.26}$$

and $n_e$ ne is the porosity of the rock layer of thickness $e$.

Accordingly, the observed experimental non-dimensional magnitudes are, gathering all the previous results:

$$\frac{X}{H_I} = \left(\frac{Ru}{H_I}, \frac{Rd}{H_I}, \frac{\eta_m}{H_I}\right) = f_\alpha\left(\frac{L}{H_I}, \frac{D_{a,n50}}{H_I}, Re, \frac{h}{L}, \frac{\tau_s}{\rho_w g L^2}, \frac{\rho_s}{\rho_w}, Re_p\right) \tag{2.27}$$

As before, $(D^*)_{CV}$ can be split in two parts: (1) due to the wave breaking process and the production and dissipation of turbulence; (2) percolation and viscous damping due to work done by the pressure and the shear stress in the rock layer during the up- and dowh-rush flow over the slope. If the rock units are tilting or displaced then an additional wave energy dissipation rate over the slope (Bagnold and Taylor, 1946) has to be considered. Herein, the case of non-moving rock units is considered. Thus the relative particle density $(\rho_s/\rho_w)$, can be discarded.

Finally, if the surface tension term is negligible ( $10^{-6}$), the $Re > 10^4$, for each slope the following functional relationship is obtained:

$$\left(\frac{Ru}{H_I}, \frac{Rd}{H_I}, \frac{\eta_m}{H_I}\right) = f_\alpha \left(\frac{H_I}{L}, \frac{h}{L}, \frac{D_{a,n50}}{H_I}, Re_p\right) \tag{2.28}$$

## 2.4 An armor layer over a permeable core

In addition to the given principal variables that intervene in the above impermeable slope structures, the wave transformation while interacting with a sloping permeable layer over a permeable core depends also on some characteristics of the core: (13) the diameter of the core material, $D_{c,n50}$; (14) its density, $\rho_{s,c}$; and (15) core width, $B$. Then, the complete set of independent variables that govern the incident wave transformation over the slope is:

$$X = f\left(g, \rho_w, \mu_w, h, L, H_I, \tau_s, \rho_s, e, D_{a,n50}, D_{c,n50}, \rho_{s,c}, B\right) \tag{2.29}$$

For this sloping permeable structure, the dependent variables of the experiment are determined according to $n = 13$ independent variables. Again, the complete set can be split in two subsets of independent quantities. The first one, $n_F = 8$, $(\rho_w, g, h, L, \tau_s, D_{c,n50}, \rho_{s,c}, B)$. Accordingly, $(\rho_w, g, L)$, $k_F = 3$, is a complete subset of the dimensionally independent quantities, and the dimensionalness independent quantities are, $n_F - k_F = 5$: $(h/L, \tau_s/\rho_w g L^2, B/L, D_{c,n50}/L, \rho_{s,c}/\rho_w)$. Then, the original complete set can be reduced to $n - (n_F - k_F) = 8$ independent quantities:

$$X = f\left(\mu_w, H_I, \rho_s, e, D_{a,n50}, \rho_w, g, L\right) \tag{2.30}$$

A complete subset of dimensionally independent quantities is $k = 3$, $(\mu_w, H_I, \rho_s)$, and the set of dimensionless independent quantities are $nk - (n_F - k_F) = 5$:

$$\frac{X}{H_I} = f\left(\frac{D_{a,n50}}{H_I}, \frac{L}{H_I}, \frac{\rho_s}{\rho_w}, Re, Re_p\right) \tag{2.31}$$

where, $R_{e,p}$ is the pore size based Reynolds number, which evaluates the wave energy damping due to percolation and viscous in the main rock layer (Equation 2.26).

Accordingly, the observed experimental non-dimensional magnitudes are, gathering all the previous results:

$$\begin{aligned}\frac{X}{H_I} &= \left(\frac{Ru}{H_I}, \frac{Rd}{H_I}, \frac{\eta_m}{H_I}\right) \\ &= f_\alpha\left(\frac{L}{H_I}, \frac{D_{a,n50}}{H_I}, Re, \frac{h}{L}, \frac{\tau_s}{\rho_w g L^2}, \frac{\rho_s}{\rho_w}, Re_p, \frac{B}{L}, \frac{D_{c,n50}}{L}, \frac{\rho_{s,c}}{\rho_w}\right)\end{aligned} \tag{2.32}$$

As before, $(D^*)_{CV}$ can be split in three parts: (1) due to the wave breaking process and the production and dissipation of turbulence; (2) percolation and viscous damping due to the work done by the pressure and the shear stress in the rock layer during the up- and dowh-rush flow over the slope; and (3) wave transformation in the secondary layers (if any) and porous core.

Herein, non-moving rock units and non-erosion of the core material are assumed. Thus, the relative particle densities, $\rho_s/\rho_w$ and $\rho_{s,c}/\rho_w$ can be discarded. Finally, the surface tension term is negligible ( $10^{-6}$), and only input wave characteristics with the $Re > 10^4$ are analyzed. Then, for each slope, the following functional relationship is obtained:

$$\left(\frac{Ru}{H_I}, \frac{Rd}{H_I}, \frac{\eta_m}{H_I}\right) = f_\alpha\left(\frac{H_I}{L}, \frac{h}{L}, \frac{D_{a,n50}}{H_I}, Re_p, \frac{B}{L}, \frac{D_{c,n50}}{L}\right) \tag{2.33}$$

Then, the flow characteristics over the slope depend on the input characteristics at the toe of the slope, and the set of experimental output should to be organized on intervals of $D_{a,n50}/H_I$. For experiments where the wave energy dissipation inside the main layer is significative, (strong-weak bore and surging), the data should be identified in function of $R_{e,p}$. Furthermore, the values of the relative core width $(B/L > 0.25)$ should help to identify the set of experimental data where the saturation of wave reflection inside the core ocurred (Requejo et al., 2002; Díaz-Carrasco et al., 2020).

# 3 Wave breaker types on impermeable slopes

**Comment**

The results of this section are integrated in the following works:

**Moragues, M.V.**, Clavero, M. and Losada, M.A. (2020) "Wave breaker types on a smooth and impermeable 1:10 slope". In: Journal of Marine Science and Engineering, 8(4), 296.
DOI: https://doi.org/10.3390/jmse8040296

**Moragues, M.V.** and Losada, M.A. (2021) "Progression of wave breaker types on a plane impermeable slope, depending on experimental design". In: Journal of Geophysical Research: Oceans, 126, e2021JC017211.
DOI: https://doi.org/10.1029/2021JC017211

*"The sea is a desert of waves, A wilderness of water."*

Langston Hughes

*In this Chapter, firstly, an analysis of the current state of art on wave breaking on impermeable slopes is done. Secondly, the types of wave breaker on a non-overtoppable, smooth and impermeable 1:10 slope under regular waves are identified. For this purpose, experimental tests were carried out in the Atmosphere-Ocean Interaction Flume of the Andalusian Institute for Earth System Research (University of Granada). Using the experimental space* $[log(h/L) - log(H/L)]$ *and the alternate slope similarity parameter* $\chi = (h/L)(H/L)$*, a complete set of breaker types was identified. The results showed that the value of the Iribarren number was not sufficient to predict the expected type of wave breaker on the slope.*

## 3.1 Introduction

As described through the dimensional analysis, the bulk dissipation of the incident wave train propagating on permeable slope depends on the transport of turbulent kinetic energy (TKE) from the following sources: (a) wave breaking causing advection and diffusion of turbulence, generating a vortex dependent on the breaking type; (b) the armor layer whose vortex depends on the characteristic diameter of the armor unit; and (c) the porous core whose turbulence scale depends on the grain size.

The Darcy-Frocheimer equation is used for estimating the flow resistance force inside the porous medium. However, despite the fact that there is some research in the literature about dissipation due to wave breaking (Rapp and Melville, 1990; Agrawal et al., 1992; Babanin, 2009; Babanin, 2011; Iafrati, 2011), it is mostly focused on wind breaking waves and not in the wave-structure interaction. Thus the local dissipation produced by the shaoling and wave breaking on the slope does not have a theoretical equivalent model, making it hard to estimate it.

For this reason, the main objective of this chapter was to analyze the progression of the extended breaker types on plane impermeable slopes. Using dimensional analysis to reduce the number of experimental variables affecting the wave-slope interaction. This research is a natural continuation and logical extension of Galvin (1968), Battjes (1974) and Díaz-Carrasco et al. (2020), *inter alia*. A breaker type classification may eventually be useful in coastal protection design against coastal risks such as flooding (Del-Rosal-Salido et al., 2019), coastal hazard from extreme storms (Grilli et al., 2020), human interaction with large-scale coastal morphological evolution (Baquerizo and Losada, 2008) and uncertainty in the assessment of coastline changes (Kroon et al., 2020), among others.

### 3.1.1 State of art on breaking analysis

Iversen (1952) conducted two sets of experiments to examine the breaker type details and the transformations in during the shaoling in plane impermeable slopes with different angles. He defined three breaker types: spilling, plunging and surging, and he concluded that they were affected by the slope angle, wave height and wave period.

Galvin (1968) identified and quantified nine breaker types obtained from recordings of the experimental tests on three laboratory smooth and impermeable slopes. Neglecting the breaker types (6-9 from Figure 3.1) that were strongly affected by the experimental conditions (reflected and secondary waves), Galvin's classification

includes the following breaker types: (1) spilling, (2) plunging, (3) well developed plunging, (4) collapsing and (5) surging.

Tables 6 and 7 from Galvin's paper show the transition values between breaker types, Surging-Plunging and Plunging-Spilling, for his inshore and offshore parameters for slopes 1:10 and 1:20, concluding that there is a continuous gradation in type of breaking from spilling to plunging to surging.

| Code | Type of Breaking | Description |
|---|---|---|
| 1 | Spilling | Bubbles and turbulent water spill down front face of wave. The upper 25% of the front face may become vertical before breaking. |
| 2 | Well-developed plunging | Crest curls over a large air pocket. Smooth splash-up usually follows. |
| 3 | Plunging | Crest curls less and air pocket smaller than in 2. |
| 4 | Collapsing | Breaking occurs over lower half of wave. Minimal air pocket and usually no splash-up. Bubbles and foam present. |
| 5 | Surging | Wave slides up beach with little or no bubble production. Water surface remains almost plane except where ripples may be produced on the beach face during runback. |
| 6 | Plunging altered by reflected wave | Small waves reflected from the preceding wave peak up the breaking crest. Breaking otherwise unaffected. |
| 7 | Plunging altered by secondary wave | Primary may ride in on secondary immediately before it, or secondary immediately behind rides in on primary in front. First kind difficult to distinguish from 8. |
| 8 | Surging altered by secondary wave | Plunging secondary may break just in front of surging primary. Difficult to distinguish from 7. |
| 9 | Secondary wave washed out | Runback from previous primary carries the secondary wave offshore, where it may break out of field of view or just disappear. |

FIGURE 3.1: Table 3 from Galvin (1968) with his classification and description of the observed breaker types.

Over the last years, several numerical studies have been published on different breaker types on a smooth and impermeable slope (Ting and Kirby, 1995; Ting and Kirby, 1996; Christensen and Deigaard, 2001; Lara et al., 2008; Zhang and Liu, 2008; Madsen and Fuhrman, 2008; Gislason et al., 2009; Lakehal and Liovic, 2011). The level of detail in these studies make it possible to identify transitions between the four breaker types proposed by Galvin (1968) and adopted by Battjes (1974).

With the relevant differences between weak and strong bore (Zhang and Liu, 2008); weak and strong plunging (Ting and Kirby, 1995; Lakehal and Liovic, 2011); and weak bore and surging (Gislason et al., 2009), the classification can be extended into six breaker types: (1) spilling, (2) weak plunging, (3) strong plunging, (4) strong bore, (5) weak bore and (6) surging.

To estimate when and how a wave is going to break, the most used criteria is a geometric one, based on the wave steepness and local wave geometry. One of the most known breaking criterion was stablished by Miche (1944), who defined a breaking criterion, valid for horizontal beds, which related the breaking wave steepness with the breaking relative water depth.

$$\frac{H_I}{L} \geq 0.14 tanh\left(2\pi\frac{h}{L}\right) \tag{3.1}$$

Iribarren and Nogales (1949) introduced the Iribarren number as an empirical non-dimensional parameter capable of describing the breaker type ($Ir$ or $\xi$).

$$Ir = \frac{tan(\alpha)}{\sqrt{H/L}} \tag{3.2}$$

Galvin (1968) proposed two classifying parameters depending on the slope angle, wave height and wave period: the deep-water steepness divided by the square of the beach slope $(H_o/(L_o m^2))$ and the breaker steepness squared divided by the slope $(H_b/(gmT^2))$.

Battjes (1974) followed and extended Galvin's work. Through dimensional analysis, he assumed that for waves breaking on the slope, the value of the relative depth in front of the slope was not important, and that the Reynolds number was usually larger than some minimum value, which did not significantly affect the resultant motion. He thus obtained the reduced approximated relationship shown in Equation 3.3, where $X$ is a dimensionless variable (output) for many overall properties of the breaking waves, and $\xi$ is a surf similarity parameter (Equation 3.2). With this assumption, he declared that the value of $\xi$ gives and indication of how the waves break: surging, collapsing, plunging or spilling (Iversen, 1952; Galvin, 1968) and he redefined Miche (1951)'s hypothesis that the reflection coefficient from waves breaking on a steep slope was proportional to the ratio of the critical wave steepness to the incident wave steepness, proposing the surf similarity parameter to analyze the behavior of a wave train interacting with a rigid, plane, impermeable slope.

$$X \approx f(\alpha, \frac{H}{L_0}) \approx f(\xi) \tag{3.3}$$

Recently, for deep and intermediate water depths, Barthelemy et al. (2018) proposed a breaking criterion based on the local incident energy flux velocity and introduced a breaking onset threshold parameter. This was later applied by Derakhti et al. (2020), who investigated the framework for predicting the wave breaking onset for surface gravity waves in an arbitrary water depth. They numerically calculated the progression of regular waves over a plane impermeable beach with different slopes. By increasing $\xi_0$, Derakhti et al. (2020) (their Figure 3a,c,e,g,i), found that there was a progression/transition from spilling to collapsing and surging. In their study, given that $\xi_0$ was defined by using the wave steepness, $H_0/L_0$, in deep water, it thus followed that $\xi_0 \neq \xi$.

## 3.2 Experimental setup

### 3.2.1 CIAO

The Atmosphere-Ocean Interaction Flume (CIAO) is part of the Environmental Fluid Dynamics Laboratory and focuses on the study of the coupling processes between the sea and the atmosphere. The wave generation system (wave flume), has

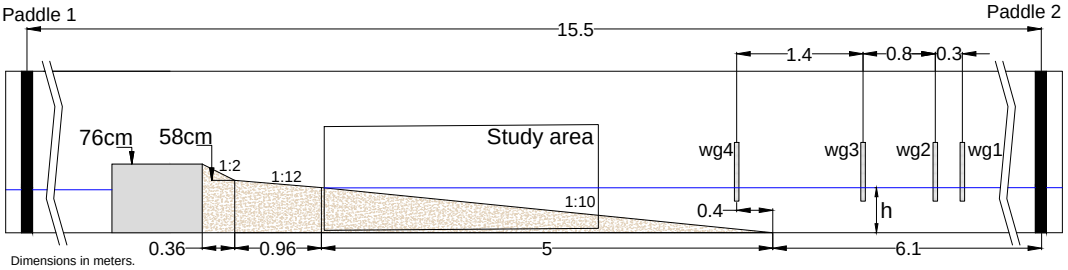


FIGURE 3.2: Diagram of the CIAO wave flume, the tested model and the wave gauges position (measurements in meters).

a width of $1m$, a designed water depth of $0.70m$ and $15m$ length. The system can generate waves with periods between 1 and $5s$ and heights up to $30cm$. One of its main features is the presence of two paddles on opposite sides, which are controlled by a software program, for the complete absorption or partial reflection of waves, including a possible phase shift of the reflected wave (Andersen et al., 2016; Addona et al., 2018; Lira-Loarca et al., 2019).

For this study, an impermeable wooden ramp, with a slope angle of 1:10 (Figure 3.2) was used. Test conditions are summarized in Table 5.1. The free surface elevation was measured using four resistance wave gauges placed along the flume before the ramp (Figure 3.2). Video cameras were used in the study section for recording and photographing the breaking waves. The three-gauge method of Baquerizo (1995) was applied to separate the incident wave train and reflected wave train. The zero-upcrossing mean wave height was estimated from the incident wave train.

The values of $H_I$ and $T_z$ used in the results were the r.m.s. wave height and the mean wave period at the toe of the ramp. While the mean periods coincided with the input periods, the incident wave height was usually lower than the input value. $L$ is the wave length, calculated with the linear dispersion equation (Equation 2.4).

TABLE 3.1: Test characteristics carried on in the CIAO wave flume. Parameters $H$ and $T$ are input values, namely, the values given to the generation system. $T_z$, $L$ and $H_I$ are the zero-upcrossing mean wave period, wavelength, and incident wave height, respectively.

| $\tan(\alpha)$ | $H(m)$ | $T(s)$ | $T_z(s)$ | $h/L$ | $H_I/L$ |
|---|---|---|---|---|---|
| 1:10 | 0.005-0.3 | 0.98-4.8 | 1.1006-5.0011 | 0.0457 - 0.3525 | 0.0009 - 0.1990 |

### 3.2.2 Data from other authors

#### Galvin (1968)

Galvin (1968) conducted a total of 75 experimental tests at the U.S. Army Coastal Engineering Research Center. He focused on three smooth and impermeable slopes (1:5, 1:10, 1:20) under regular waves. The test conditions are summarized in Table 3.2. Analyzing a series of ten consecutive regular waves, a classification of the types of wave breakers was set. A clear relationship was found between the onset of wave breaking and the type of breakers and (1) the deep water steepness ($H_o/L_o$) and (2) the "breaker steepness" parameter ($\sqrt{H_b/gT^2}$). Both parameters are dependent on the slope, indicating the importance of separating the data according to the slopes.

TABLE 3.2: Test characteristics of Galvin (1968). Parameters H and T are input values, namely, the values given to the generation system and L the wave length.

| $\tan(\alpha)$ | $H(m)$ | $T(s)$ | $h/L$ | $H/L$ |
|---|---|---|---|---|
| 1:5 | 0.024 - 0.092 | 1.00 - 8.00 | 0.0191 - 0.2627 | 0.0049 - 0.0505 |
| 1:10 | 0.024 - 0.109 | 1.00 - 8.00 | 0.0191 - 0.2627 | 0.0049 - 0.0505 |
| 1:20 | 0.054 - 0096 | 1.00 - 6.00 | 0.0033 - 0.2627 | 0.0053 - 0.0505 |

**Derakhti et al. (2020)**

Derakhti et al. (2020) conducted 27 numerical tests (LES/VOF and FNPF-BEM) simulating a planar beach under different wave trains. Regular wave trains were run with a constant wave period and few constant water heights. Six of them have information about the breaker type. Conditions for these six tests are summarized in Table 3.3.

TABLE 3.3: Test characteristics of Derakhti et al. (2020). Parameters H and T are input values, namely, the values given to the generation system and L the wave length.

| $\tan(\alpha)$ | $H(m)$ | $T(s)$ | $h/L$ | $H/L$ |
|---|---|---|---|---|
| 1:5 | 0.18, 0.24 | 4.00, 4.00 | 0.0577, 0.0577 | 0.0208, 0.0277 |
| 1:10 | 0.15 | 4.00 | 0.0577 | 0.0173 |
| 1:20 | 0.15 | 4.00 | 0.0577 | 0.0173 |
| 1:40 | 0.15 | 4.00 | 0.0577 | 0.0173 |
| 1:200 | 0.12 | 4.00 | 0.0443 | 0.0173 |

## 3.3 Breakers definition

The classification and description of the wave breakers is somewhat subjective and clearly dependent on the observation technique. Galvin (1968) identified and classified his experimental breakers based on an overall description of the wave transformation on the slope, focusing on the steepness and roller of the wave front and its spatial evolution on the slope. In this research the classification of Galvin (1968) (surging, collapsing, plunging and spilling) is extended with Moragues et al. (2020b) in: surging, weak bore, strong bore, strong plunging, weak plunging and spilling.

The transition from a non-breaking wave to a visible breaking process at the crest of the wave (spilling breaker) seawards the slope, in constant depth, the criterion of Derakhti et al. (2020) can be adopted once the maximum wave steepness at the toe of the slope fulfills Miche (1944)'s criterion (Equation 3.1).

On the other hand, the transition from a surging wave to a standing full reflective wave might be identified once the collapse of the toe of the wave has ceased to occur (Derakhti et al., 2020) and/or the wave tip on the slope is no longer turbulent (Gislason et al., 2009).

The analysis of the photographs and videos taken at the CIAO wave flume (Figure 3.3) showed that the characteristics of each transition between the different breakers were the following:

- Surging: The wave trains oscillate (like a standing wave), generating no turbulence in the profile. The period of the water rising and falling along the slope is considerably larger than the wave period (Figure 3.3(a-b)).
- Weak bore: The inclined plane becomes more vertical, becomes unbalanced and collapses in the middle or bottom of the water column without volute (Figure 3.3(c-d)).
- Strong bore: There is an attempt to plunge, but, before it can finish the plunge, the front collapses, generating an inclined plane, mixing water and air bubbles generating a lot of turbulence. The water surface behind the crest is almost plane (Figure 3.3(e-f)).
- Strong plunging: The wave volute appears impacting the slope, hitting it and bouncing back. There is a lot of splashed water and the wave loses a lot of energy. The development of a bump on the leeside of the wave causes the strong jet (Figure 3.3(g-h)).
- Weak plunging: The wave volute appears and impacts on the wave itself, around the mean level, generating a roller which propagates with the wave (Figure 3.3(i-j)).
- Spilling: The wave volute begins, but disappears in turbulence before it impacts the slope or the wave. The jet evolves at the crest of the wave, above the mean level (Figure 3.3(k-l)).

The differences between strong bore and weak bore found by Zhang and Liu (2008) in the numerical model and the differences between strong and weak plunging metioned by Ting and Kirby (1995) and Lakehal and Liovic (2011) in a physical and numerical model respectively, are also visible in the physical flume.

## 3.4 Experimental space

By applying the method of dimensional analysis (Chapter 2) for a given slope angle, it was possible to obtain a functional relationship between the flow characteristics on a plane impermeable slope and the non-dimensional variables, $h/L$ and $H_I/L$. The $\pi$-theorem does not provide the form of the functional relationship. This form can only be obtained by physical or numerical experimentation or by theoretically solving the problem (Sonin, 2001). Based on experimental evidence that flow characteristics and breaker types are two facets of the same process, it was expected that for each slope, $m = \tan\alpha$, there would be a functional relationship between the wave breaker types and the non-dimensional variables, $h/L$ and $H_I/L$, determined at the toe of the structure.

Galvin's experimental data pertain to three slopes: (a) $m = 1{:}5$; (b) $m = 1{:}10$; and (c) $m = 1{:}20$. For each one, the stroke, $S_w$, of the generator and the wave period, $T$, varied. Following linear theory (Dean and Dalrymple, 1991), the pair of values $(H_I, L)$ at the toe of the structure were computed. Figure 3.4 (a, b, and c) show Galvin's experimental data for the three slopes and the reported wave breaker type. The experimental space for each slope is approximately defined by Equation 3.4, where $A$ and $B$ are the parameters of a straight line fitted to experimental points $h/L$ and $H/L$. It should be highlighted that the approximated linear relationship between the value pairs of the log-transform of $h/L$ and $H/L$ determines a very

(a) (b)

(c) (d)

(e) (f)

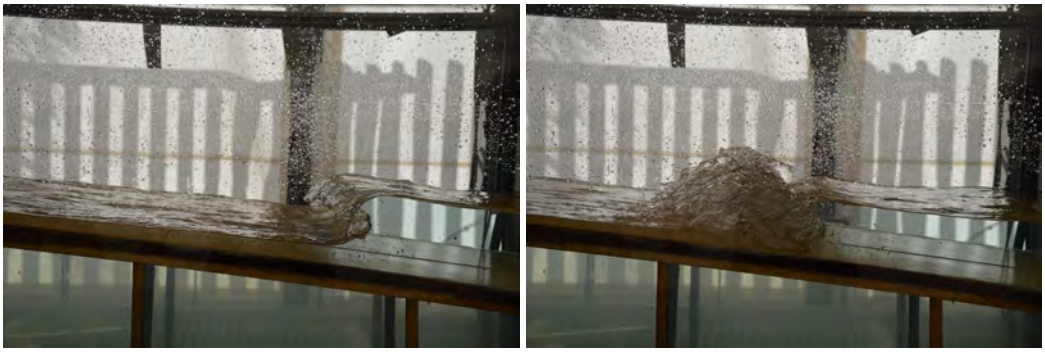

(g) (h)

FIGURE 3.3: Photographs of the progression of the breaker types on an impermeable 1:10 slope. *(cont.)*

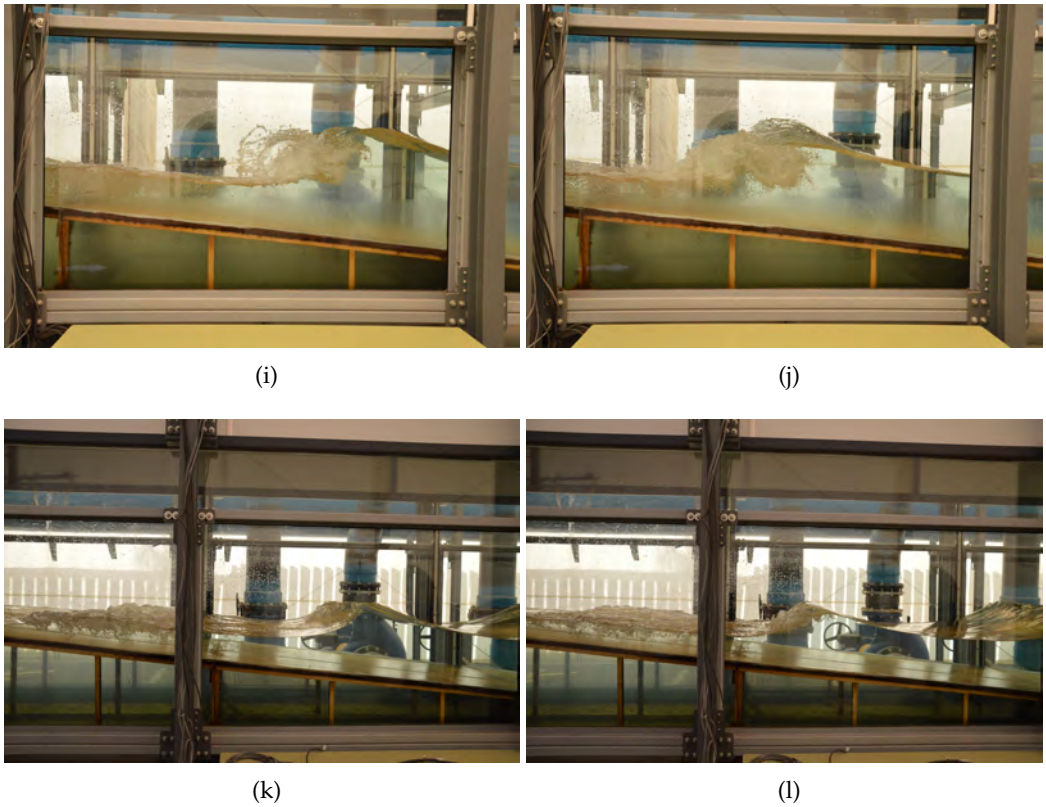

(i) (j)

(k) (l)

FIGURE 3.3: Photographs of the progression of the breaker types on an impermeable 1:10 slope. (a-b) Surging; (c-d) Weak bore; (e-f) Strong bore; (g-h) Strong plunging; (i-j) Weak plunging; and (k-l) Spilling.

narrow experimental input. The use of the log-transform should help to capture the variability of the experimental output (observed dominant breaker types) under very small changes of the experimental input.

$$\begin{aligned} Y &\approx A \cdot X + B \\ X &= \left(\frac{H}{L}\right) \\ Y &= \left(\frac{h}{L}\right) \end{aligned} \tag{3.4}$$

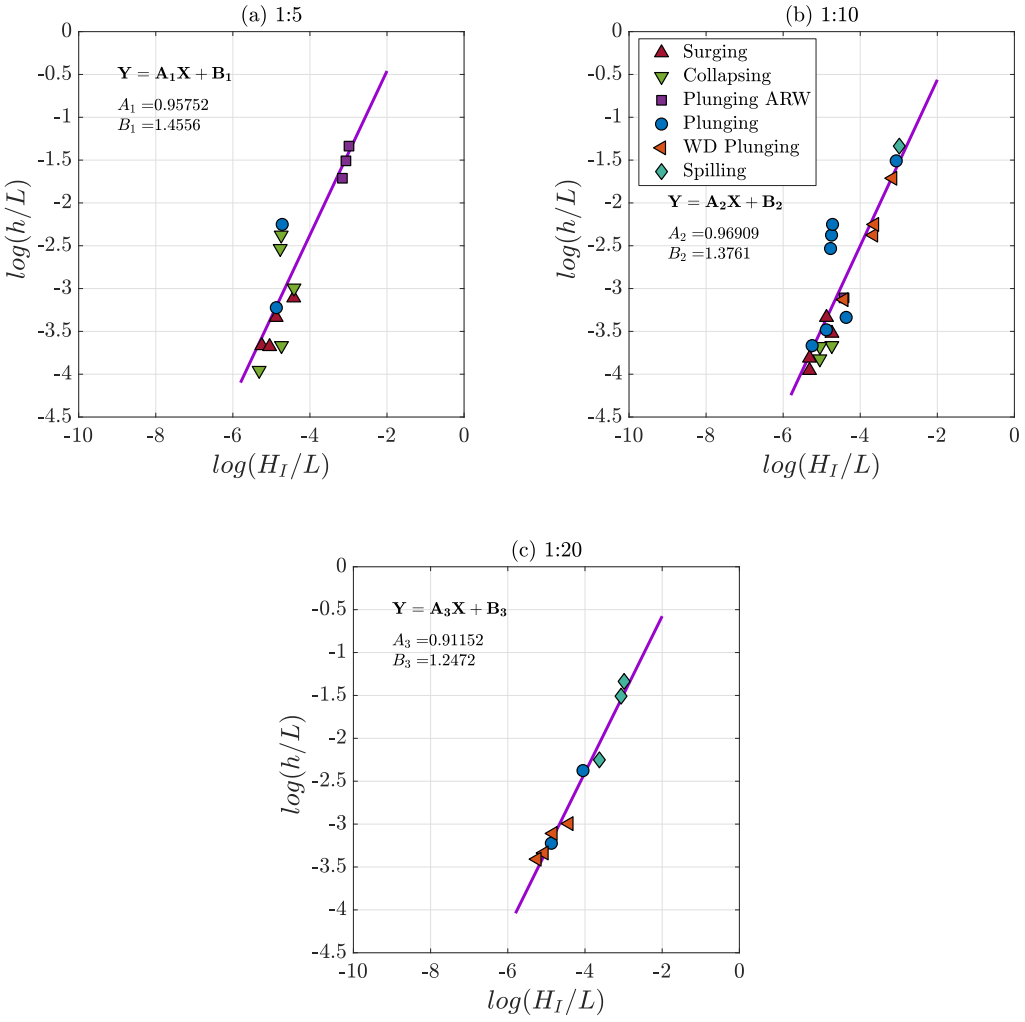


FIGURE 3.4: Experimental space (wave input) $[log(H_I/L)$ versus $log(h/L)]$ and observed output (breaker types) data (Galvin, 1968) for three impermeable smooth slopes: (a) 1:5; (b) 1:10; and (c) 1:20. Breaker types as classified in Table 3 by Galvin (1968). WD plunging and plunging ARW identify well developed plunging and plunging altered by a reflected wave, respectively. For each slope, breaker types evolve with the pair of values, HI/L and h/L; The purple line represents the linear fit to the experimental data (Equation 3.4).

According to Galvin (1968), for each slope the breaker type evolves with the pair of values $H/L$ and $h/L$. For a given water depth, i.e. $log(h/L) \approx -2.4$, the breaker

type evolves with the chosen value of $m$ and $H/L$. And for a given wave steepness, i.e. $log(H/L) \approx -4.8$, the breaker type evolves with the values of $m$ and $h/L$.

Figure 3.5 shows the data of Derakhti et al. (2020) in the numerical experimental space $[log(H_I/L), log(m)]$ under regular waves, (see their Table 1 Input parameters for the simulated cases and the output breaker types in their Figure 3). The value of the incident wave height $H_I$ and of the wave period at the toe of the structure are assumed to be approximately equal to $H_w$, wave height, and wave period, $T_w \approx 4s$, at the wavemaker. Regardless of the value of $\xi_0$, (equal to the inverse of the square root of Galvin's offshore parameter), the values of $H_I/L$ and $h/L$ at the toe of the slope are both approximately constant. For a constant water depth, i.e. $h/L \approx 0.0577$, (0.0443 only for slope 1:200), the breaker type evolves with the chosen value of $m$ and $H_I/L$. And for a given wave steepness, i.e. $log(H_I/L) \approx -4.0$, the breaker type evolves with the values of $m$ and the chosen value of $h/L$. Therefore, this dataset for regular waves only confirms that once a pair of characteristic wave values at the toe of the slope is selected and as $m$ progressively decreases, the six breaker types of the classification can be observed.

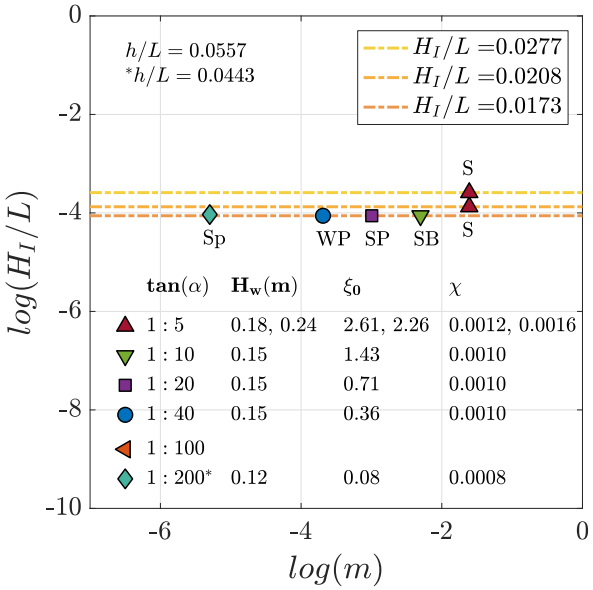


FIGURE 3.5: Experimental numerical space input, slope, and $H_I/L$ from Derakhti et al. (2020) under regular wave trains. Data in their Table 1. The relative water depth is constant ($h/L \approx 0.058$ except for the 1:200 slope $h/L \approx 0.044$). Values of $H_w$ and $\xi_0$ given by Derakhti et al. (2020) in their Figure 3. The wave height and wave period at the toe of the slope are assumed to be approximately equal to the wave height and wave period at the wavemaker, $H_I \approx H_w$ and $T \approx T_w$.

The conventional experimental technique (Galvin, 1968; Van Der Meer, 1988) involves building a ramp with a fixed slope, and running sets of tests with a fixed wave period, while progressively increasing the wave height. Since this study involved a ramp with a constant slope (i.e. $m$ = 1:10), the breaker types depended on the combination of $h/L$ and $H_I/L$ values, Figure 3.6. The pairs of values were thus selected so as to be able to observe the largest possible number of breaker types and their progression, and also to plot them, according to the wave characteristics and the alternate similarity parameter, $\chi$ (Equation 3.5). Díaz-Carrasco et al. (2020) showed that this provides an accurate description of the interplay between the characteristic wave pairs ($h/L$ and $H_I/L$) in the wave energy transformation processes

on a given slope.

$$\chi = \frac{h}{L}\frac{H_I}{L} \tag{3.5}$$

In summary, the dominant breaker types and their progression/gradation depend on three quantities: (1) the characteristics of the incident waves at the toe of the slope, $h/L$ and $H_I/L$; and (2) the slope, $m$. Obviously these three can be used to construct a 3D graph, where the prevalence regions of the different breaker types can be observed. However, the interplay of the three quantities is most accurately and usefully represented by graphic representations in a 2D system in terms of value pairs (taken two by two) while the other quantity remains constant.

Accordingly, it is either possible to combine values of $m$ and $H_I/L$, while $h/L$ remains constant, to combine values of $m$ and $h/L$, while $H_I/L$ remains constant, or to combine values of $h/L$ and $H_I/L$ while $m$ remains constant. In the first option the data can be plotted based on the surf similarity parameter. However, in contrast to Battjes (1974), the dependence of the relative water depth cannot be ignored since for each value of the depth and slope, different sequences of breaker types are obtained. If the wave steepness remains constant and the pairs of $h/L$ and $m$ values are combined, the change in $h/L$ value signifies a change in $H$ (to maintain the wave steepness value), and, consequently, in the progression/transition of breaker types. If $m$ remains constant, the breaker types then depend on the combination of $h/L$ and $H_I/L$ values.

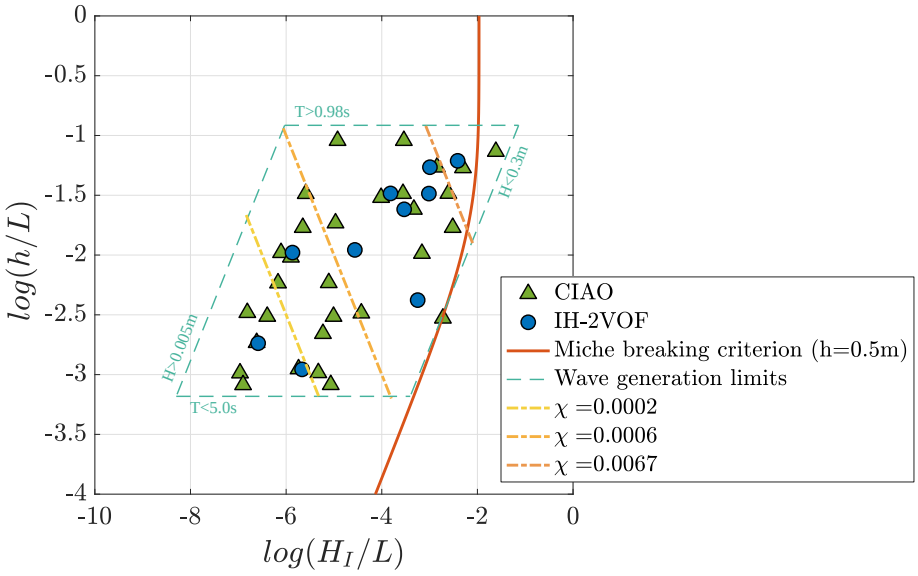


FIGURE 3.6: Numerical (IH-2VOF) and physical (CIAO) experimental space, $h/L$ and $H_I/L$, in a log-transform coordinate system devised for this research study: regular wave train impinging on a plane impermeable slope 1:10. The wave generation limits of the flume are determined by the parallelogram (dashed blue lines). The orange curve shows the maximum wave steepness of a progressive wave train propagating in a constant water depth ($h = 0.50m$), as calculated with Miche (1944)'s equation (Equation 3.1). Lines of the constant value of $\chi$ are shown (yellow dashed lines).

## 3.5 Specification of the input wave characteristic at the toe of the slope

The characteristics of the incident wave train of experiments by Galvin (1968) and Derakhti et al. (2020) were not given at the toe of the slope. To uniquely specify any of the tests, Galvin chose the following four experimental variables: beach slope, depth at the toe of beach, generator stroke, and period. For this research, the generated incident wave height was estimated by applying the linear theory of wave generation (Dean and Dalrymple, 1991). In addition, it was assumed that the estimated wave height near the paddle was representative of the incident wave height at the toe of the depth. This implies that the generation of the incident wave was not affected by the reflected wave train, and also that the energy dissipation down at the bed and the side walls of the flume was negligible.

Table 1 of Derakhti et al. (2020) provides the input parameters, namely, the slope and wave height and wave period of the regular wave train at the wavemaker, the distance of the wavemaker to the toe of the slope L1, and the surf similarity parameter in deep water. For all the simulated cases, P1-r-LV to P6-r-LV, it was considered that L1 = 0. The LES/VOF model specifies the total instantaneous free surface, and the liquid velocity at the model upstream boundary. It was then assumed that the incident wave height and wave period at the toe of the structure were approximately equal to their respective values at the wavemaker. Moreover, the output breaker type was taken from their Figure 3. Note that this model neglects the interfacial surface tension and viscous stress. Moreover, the subgrid-scale (SGS) stress is estimated using an eddy viscosity assumption and the Dynamic Smagorinsky model, which includes water/bubble interaction effects.

The experimental space, depicted in Figures 3.4 and 3.5, shows the progression of breaker types under two different conditions, linear relationship $log(H_I/L) - log(h/L)$, (Galvin, 1968) and constant h/L (Derakhti et al., 2020). Independently of the rough method applied to obtain the wave characteristics at the toe of the slope, the breaker types observed by Galvin (1968) and by Derakhti et al. (2020) follow the derived functional relationship.

## 3.6 Observed and predicted breaker types and their expected variability

The progression of breaker types under a regular wave train on a smooth impermeable slope is based on the extended classification of breaker types (Moragues et al., 2020b). The classification and description of the six breaker types are mainly based on the work by Ting and Kirby (1995) and Ting and Kirby (1996) for spilling and weak and strong plunging, Lakehal and Liovic (2011) for strong plunging, Zhang and Liu (2008) for strong and weak bore, Gislason et al. (2009) for surging, and Galvin (1968) and Derakhti et al. (2020) for spilling, plunging, collapsing and surging. The numerical and physical model by the authors completes the existing database. It is obvious that the adscription of an observation to a breaker type has a subjective component, in particular in the case of the transitions of breaker types.

To minimize the subjectivity, in addition to the classical descriptions reflected in Figure 11 of Galvin (1968) and Figure 3 of Derakhti et al. (2020), some distinctive features of each breaker types are used:

- The jet of a weak plunging hits the front slope of the wave around the mean water level, while in the spilling breaker the jet evolves locally at the crest and above the mean water level.
- The jet of a strong plunging breaker hits the water surface or the return flow landwards of the front slope. The existence of a strong jet is related to the development of a hump on the leeside of the crest. This increases the pressure and strengthens the water circulation from the bottom towards the jet, see Figure 1 of Galvin (1968) and Figure 9 of Lakehal and Liovic (2011). Straight furrows moving parallel to the crest, and behind it, identifying the sequence of developed vortices with horizontal axes.
- This hump is not observed in a strong bore. The water surface behind the crest is almost plane and collapses at different parts of the front above the bottom, see Figure 5 of Zhang and Liu (2008).
- A weak bore develops a turbulent front face and at the toe a slip thin up-rush layer with a turbulent front, see Figure 1 of Galvin (1968) (collapsing breaker) and Figure 3 of Zhang and Liu (2008).
- Surging breaker is almost an oscillatory motion with a very narrow tip with bubbles, see Figure 1 of Galvin (1968) (surging breaker) and Gislason et al. (2009).

## 3.7 Conclusions

The objective of this chapter was to identify the wave breaker types on an impermeable smooth 1:10 slope and to define a parameter able to determine where the transition between breakers occur. This study used dimensional analysis to demonstrate that relative water depth is a key explanatory quantity, and that its omission very likely results in an incorrect dimensional analysis model.

Dimensional analysis was used to show that the dominant breaker types and their progression/transition depend on three quantities: (1) the characteristics of the incident waves at the toe of the slope, $h/L$ and $H_I/L$; and (2) the slope, $m$. The interplay of these three quantities is most accurately and usefully represented by graphic representations in a 2D system in terms of value pairs (taken two by two) while the other quantity remains constant. Accordingly, it is either possible to combine values of $m$ and $H_I/L$ while $h/L$ remains constant, to combine values of $m$ and $h/L$ while $H_I/L$ remains constant, or to combine values of $h/L$, and $H_I/L$ while $m$ remains constant.

New physical and numerical experiments conducted on an impermeable 1:10 slope were conducted to approximately delimit the regions of the experimental space where each of the six breaker types, as described by Moragues et al. (2020b) and Moragues and Losada (2021), occurred most frequently. Based on the analysis of four datasets, Galvin (1968), Derakhti et al. (2020) and the present physical and numerical experiments, this research showed that the breaker types on a given slope

can be well approximated by the log-transform of the alternate similarity parameter $\chi = (h/L)(H_I/L)$.

The use of the experimental space could help to develop the experimental design. It made it possible to forecast the types of breaker, as well as the variability of the flow characteristics, wave energy transformation and structure stability. The types of wave breaker identified previously in the numerical computation were verified with the physical breakers observed in the CIAO flume. For that purpose, the application of the alternative slope parameter $\chi$ was relevant. Thus, with a smaller number of tests, a wider range of results were obtained. The time of the physical experiments was also decreased; and even more importantly, costs were lowered.

# 4 Prevalence and progression of breaker types

**Comment**

The results of this section are integrated in the following work:

**Moragues, M.V.** and Losada, M.A. (2021) "Progression of wave breaker types on a plane impermeable slope, depending on experimental design". In: Journal of Geophysical Research: Oceans, 126, e2021JC017211. DOI: https://doi.org/10.1029/2021JC017211

*"The breaking of a wave cannot explain the whole sea."*

Vladimir Nabokov

*The objective of this research was to analyze the progression of breaker types on plane impermeable slopes. The dominant breaker types depend on the incident wave characteristics at the toe of the slope. Accordingly, it is possible to combine values of H, T and m. The physical experiments of Galvin (1968), recent numerical results, and new experiments, performed on an impermeable 1:10 slope, were used to verify the result. It was thus possible to obtain the progression of breaker types in different sequences of pairs of combined wave H and T values. Once a sequence is defined, the expected progression of breaker types is predictable, and is well approximated by the log-transform of the alternate similarity parameter. Since the classification of breaker types is discontinuous, the data assigned to each type were placed in horizontal lines, based on the value of $log(\chi)$. Given that the breaking of a wave train on a slope should be considered a continuous process, the location of some data was corrected to satisfy this assumption. There is thus a functional relationship between the sets of the experimental space and of the breaker types. This research also derives the non-dimensional energy dissipation on the slope, considering the wave-reflected energy flux on the slope. It is proportional to a dimensionless bulk dissipation coefficient which depends on the breaker type and, therefore, on the value of $\chi$ at the toe of the slope.*

## 4.1 Introduction

In the previous Chapter, Figure 3.3 showed photographs of six breaker types included in the extended classification. It is not unusual for one observer to associate the same breaker type in two wave trains, whose progression shows certain differences, and for another observer to consider them to be two different breaker types. Figure 4.1 shows the photographs of two breaking waves both classified as strong plunging (SPl). The first one is more similar to (or shares characteristics with) a strong bore (SB), whereas the second one is closer to a weak plunging (WPl) breaker. Indeed, the volute of each wave impacts at different points, such as the front slope or the toe of the wave, and both waves show a hump on the sea side of the wave crest (a distinct feature of plunging breakers), although of different dimensions. Nevertheless, both breaker types are classified as SPl. Figure 4.2 shows the location of the photographs in the experimental space.

As previously explained in the experimental space, the transition between breakers does not occur in a fixed value of $\chi$ but it happen progressively. This is the reason why some breakers can be identified as different types by different authors. In Figure 4.1 where two strong plunging are shown, the volute of the first wave (a and b) impacts with the slope with a vertical wall of water and bubbles, while the second one (c and d) impacts in the lower part of the wave front.

One cause of these discrepancies, as discussed further on, is that the classification is based on transitional intervals of the breaker types, whereas observed reality progresses more gradually. Moreover, thanks to the improvement in visual techniques and advanced numerical codes, it is now possible to obtain very detailed information regarding the progression of the kinematics and dynamics of the breaking process, small-scale behaviors, flow features, and the fluid-air interaction (Zhang and Liu, 2008; Derakhti et al., 2020). For this reason, discrepancies regarding interval classification, visual wave channel observation, and the quasi-continuous description of the numerical models will doubtlessly increase.

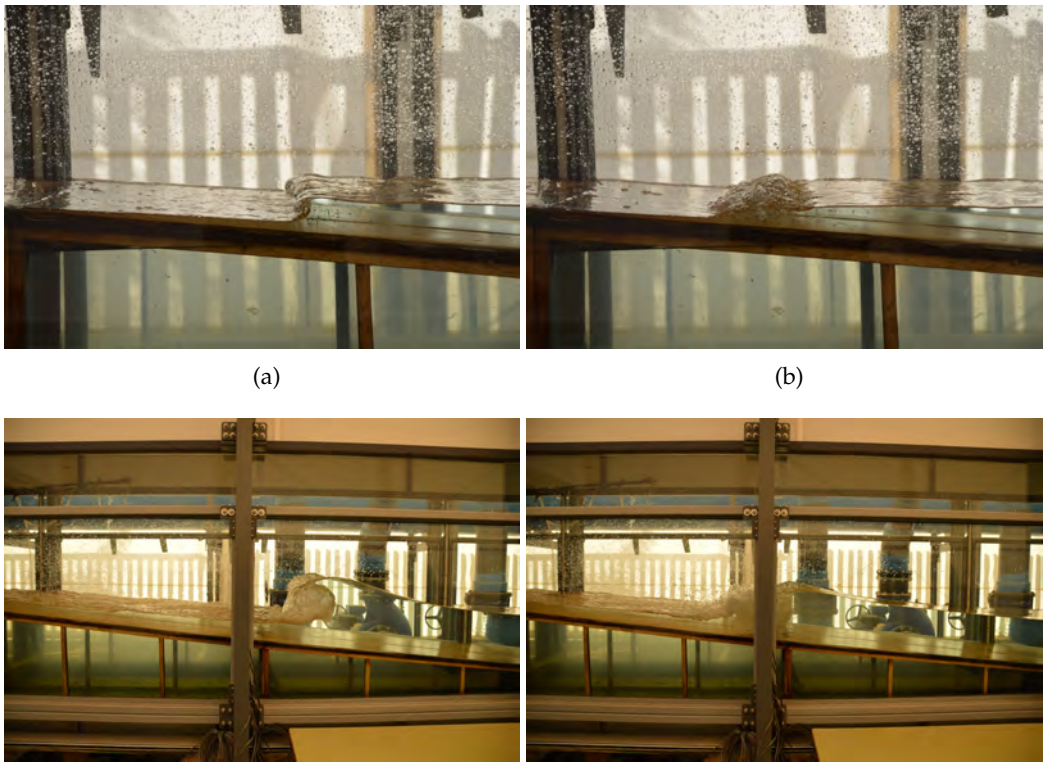

(a) (b)

(c) (d)

FIGURE 4.1: Photographs of a strong plunging: in (a) and (b) closer to a weak bore; and in (c) and (d) closer to a weak plunging.

The objective of this chapter is to show the link between the experimental technique and the expected breaker types and to discuss the implications of the transitional intervals of the breaker type classification for its applicability, based on the continuous hypothesis of the breaker progression.

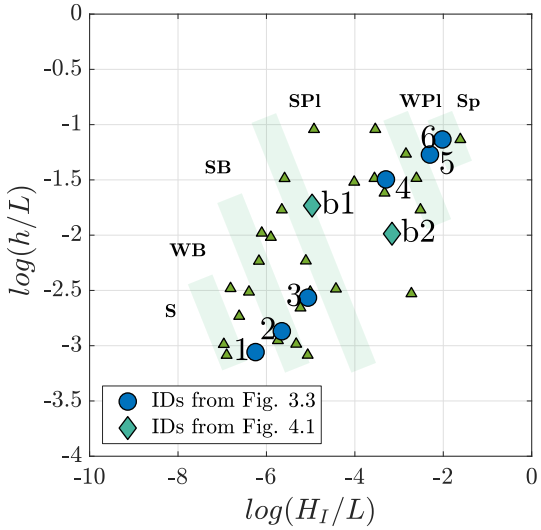


FIGURE 4.2: The ID numbers identify the photographs in Figure 4.1 in the experimental space. (a) strong plunging closer to a strong bore. (b) strong plunging closer to a weak plunging.

## 4.2 Regions of prevalent breaker type

Based on previous work (Díaz-Carrasco et al., 2020; Moragues et al., 2020b) and after the visualization of a large number of photographs, videos, and numerical results, green strips were plotted in the experimental space of the test performed in the CIAO wave flume and with the numerical model IH-2VOF on an impermeable 1:10 slope, Figure 4.3. Each strip signals the border between contiguous breaker types. They mark the boundaries of the regions in the experimental space where each of the six breaker types is prevalent. Their width merely indicates that at the moment, with the current dataset and the intrinsic variability of breaker types, it is difficult to be more precise. It should be highlighted that the strips follow straight lines of the constant value of $\chi = (h/L)(H_I/L)$. This configuration of the regions is specific to the slope with $m$ = 1:10.

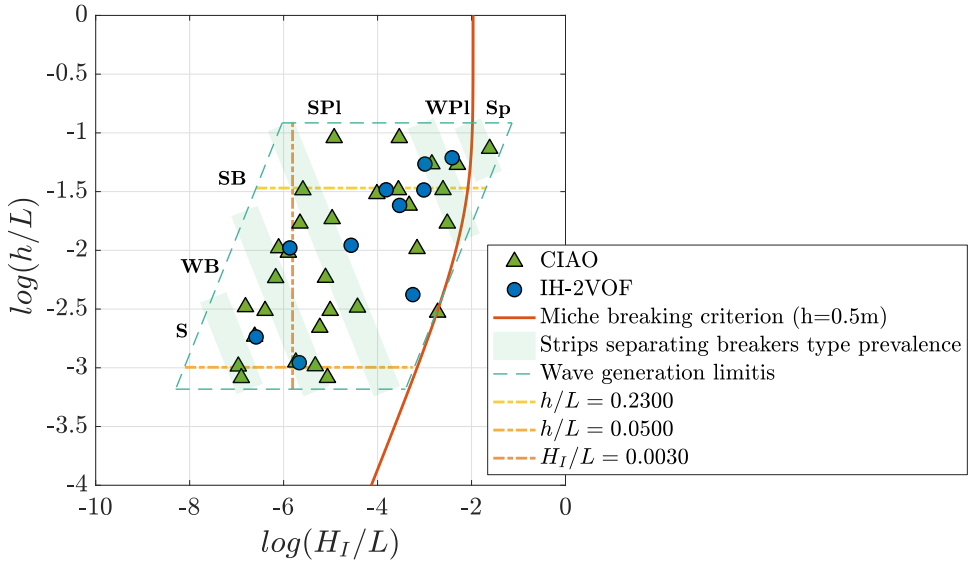


FIGURE 4.3: Experimental wave characteristics of the test performed in the CIAO flume and with the numerical model IH-2VOF on an impermeable 1:10 slope. Green strips indicate the transition between the six breaker types. The breaking criterion from Miche (Equation 3.1) is also plotted.

For a given relative depth, when $log(H_I/L)$ is increased, the line parallel to the x-axis crosses the strips that separate the prevalence regions of some of the six breaker types of Galvin's extended classification: S, WB, SB, SPl, WPl, and Sp. The blue dashed lines determine the sample space of the value pairs $[h/L, H_I/L]$ that can be generated in the CIAO flume. For $h/L \approx 0.23$ ($log(H/L) \approx -1.5$), no wave breaking can be observed in WB and S. And for $h/L \approx 0.05$ ($log(h/L) \approx -3.0$), no wave breaking can be observed in WPl and Sp. Analogously, for a given wave steepness, when $log(h/L)$ decreases from deep water to shallow water, the line parallel to the y-axis crosses the strips that separate the prevalence regions of some of the six breaker types. For $H_I/L \approx 0.003$ ($log(H_I/L) \approx -5.8$), SPl, SB and WB can be observed.

## 4.3 The link between experimental technique, data analysis and progression of breaker types

Figure 4.4 shows one of the common experimental techniques used in many laboratories for testing hydrodynamic performance on sloping structures. It involves maintaining the Iribarren number or wave steepness constant (in this case, for the same 1:10 slope) in the coordinate system $[log(H_I/L), log(h/L)]$. Figure 4.4(a) shows three vertical lines fitted to three experimental datasets, each with a different wave steepness value. For the same three datasets, Figure 4.4(b) shows the corresponding breaker types observed versus the log-transform of the alternate similarity parameter, $\chi$ (Equation 3.5). For each set impinging on a 1:10 slope, only two or three breaker types can be observed.

The white diamonds represent the breaker types observed on some of the sides that delimit the parallelogram of the sample space. The three lines fitted to the three sets of points in Figure 4.4(b) correspond to the three vertical lines in Figure 4.4(a), which link the observations to a constant $H_I/L$. It should be highlighted that in Figure 4.4(a), the points with the same type of wave breaking (e.g. SB and $log(H_I/L) \approx -5$ are located within their region, whereas in Figure 4.4(b) , they are located on a separate horizontal line based on the value of $log(\chi)$.

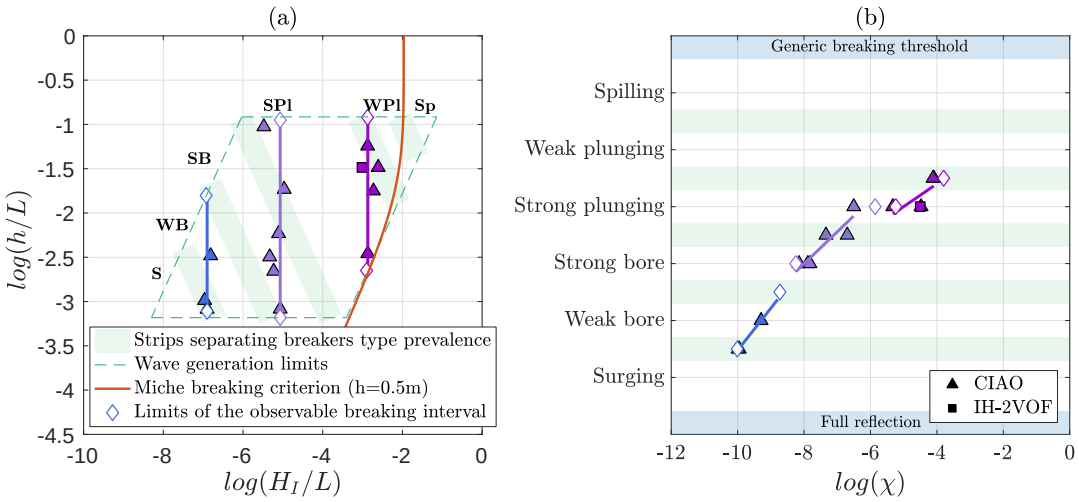


FIGURE 4.4: (a) Log-transformed experimental space with a wave steepness limit (Miches equation) and wave flume generation limits for 1:10 slope. Three lines are fitted to data points following a vertical trend (constant $H/L$ or $Ir$). (b) Breaker types versus $log(\chi)$. White diamonds show the breaker type observed over the sides of the parallelogram experimental space. The fitted straight lines describe the progression of breaker types as a continuous process as a function of $\chi$. Each line corresponds to a fitted line in Figure(a), (with the same color), which satisfies Equation 3.4.

Figure 4.5(a) and (b) shows the experiments conducted with another common experimental technique, which consists in maintaining the water depth and wave period constant. Thus, when the relative water depth remains the same, and the wave height (or steepness) increases, different breaker types can be observed. In the experimental space $[log(H_I/L, log(h/L)]$, Figure 4.5(a) shows three lines fitted to three experimental data-sets within the parallelogram. Figure 4.5(b) shows that for each set impinging on a 1:10 slope at a given relative water depth, three or four breaker types can be observed. As shown in Figure 4.5(a), the points with the same

type of wave breaking (e.g. SPl and $log(h/L) \approx -1.5$ are situated within their region. In Figure 4.5(b), they are located on a horizontal line and are separated, depending on the value of $log(\chi)$.

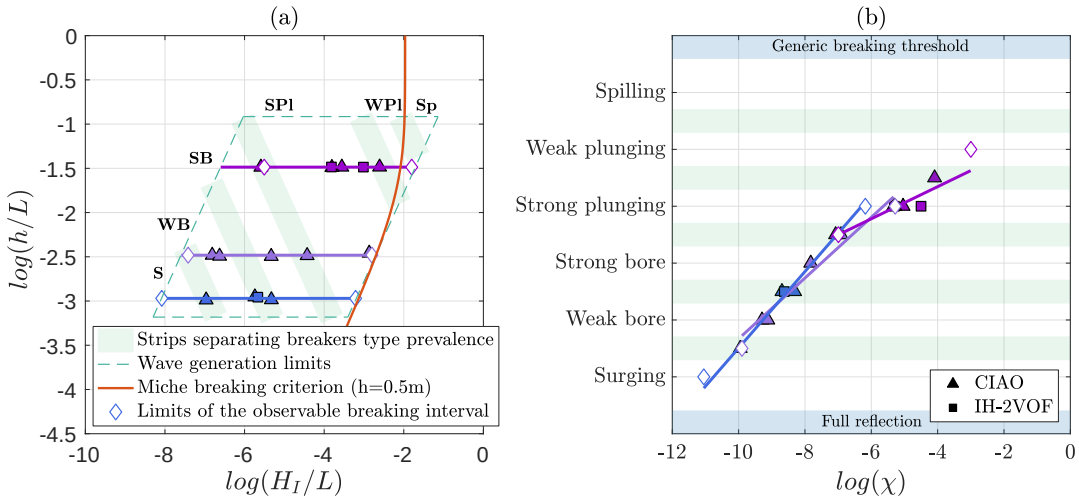


FIGURE 4.5: (a) Log-transformed experimental space with a wave steepness limit (Miches equation) and wave flume generation limits for 1:10 slope. Three lines are fitted to data points following a horizontal trend (constant $h/L$). (b) Breaker types versus $log(\chi)$. White diamonds show the breaker type observed over the sides of the parallelogram experimental space. The fitted straight lines describe the progression of breaker types as a continuous process as a function of $\chi$. Each line corresponds to a fitted line in Figure(a), (with the same color), which satisfies Equation 3.4.

Figure 4.6(a) and (b) shows the experiments in which the water depth remained constant and the wave period and wave height varies. Figure 4.6(a) shows three lines fitted to three experimental datasets within the parallelogram. For the three datasets, Figure 4.6(b) shows the corresponding breaker types versus the log-transform of the alternate similarity parameter, $log(\chi)$ (Equation 3.5). For oblique lines with a positive slope (purple line) and a shallow or intermediate water depth all of the breaker types were observed. However, as the relative water depth increased (blue line), some of the breaker types did not occur. Moreover, for the oblique lines with a negative slope (green line) following a green strip, only one breaker type (strong bore) was observed. As shown in Figure 4.6(a), points with the same breaker type (e.g. SB) are located within their region, whereas in Figure 4.6(b), they are located on a separate horizontal line, depending on the value of $log(\chi)$.

For purposes of comparison, Figure 4.7 shows, for the set of experiments conducted by Galvin (1968) over a 1:10 slope (Figure 3.4), the corresponding breaker types versus the log-transform of the alternate similarity parameter, $\chi$ (Equation 3.5). The breaker types observed by Galvin (1968) are adapted to the classification proposed in Moragues et al. (2020b). Moreover, the straight line fitted to the breaker types observed in the CIAO wave flume (blue line in Figure 4.6b) 1:10 slope is plotted. Thus, the progression of breaker types on a given slope depends on the experimental design and technique, and depends on the interplay of the wave characteristics as described by the alternate similarity parameter, $\chi$.

The link between experimental design and technique, data analysis, and progression of breaker types, is also present when the values of $m$ and $H_I/L$ are combined and $h/L$ remains constant. Thus, for a given relative water depth, the progression of breaker types depend on the interplay of the slope and wave steepness, see Figure

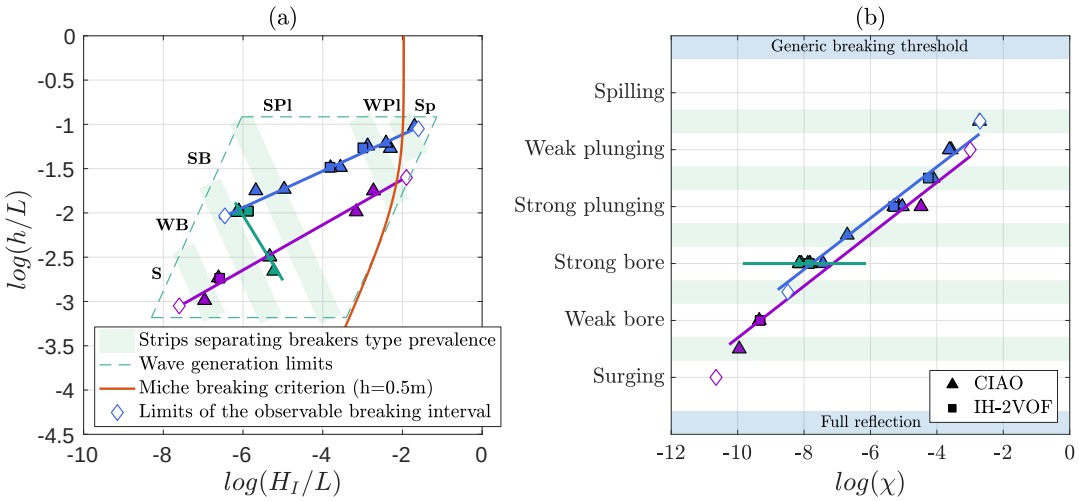


FIGURE 4.6: (a) Log-transformed experimental space with a wave steepness limit (Miches equation) and wave flume generation limits for the 1:10 slope. Three lines are fitted to data points following an oblique trend, Equation 3.4: two with a positive slope (purple and blue lines) and one with a negative slope (green line). (b) Breaker types versus $log(\chi)$. White diamonds show the breaker type observed on the sides of the parallelogram experimental space. The fitted straight lines describe the progression of breaker types as a continuous process as a function of $\chi$. Each line corresponds to a fitted line in Figure(a), (with the same color), which satisfies Equation 3.4.

3.5 with the data by Derakhti et al. (2020). Battjes (1974) proposed the use of the surf similarity parameter Equation 3.2. Although the theoretical $\xi_0 \neq \xi$ varies, the wave steepness at the toe of the slope, when compared with $m$, does not vary excessively, and $\xi$ mimics $m$.

Figure 4.8 shows the observed breaker types, adapted to the classification in Moragues et al. (2020b) versus the log-transform of $m$. Regardless of the fact that the observed dataset is obtained by varying the slope two orders of magnitude, the fitted straight line connecting the data with $\chi \approx 0.001$, describes the progression of breaker types as a continuous process, depending on $log(m)$. Because all those data have the same relative water depth value, the progression of breaker types depends on the interplay of the slope and wave steepness.

## 4.4 The transitional intervals and the continuous hypothesis of breaker type progression

A careful analysis of the photographs in Figure 4.1, reveals that the overturn and plunge of the front jet are slightly different. More specifically, they are stronger and larger for $log(\chi) \approx -6.75$, approaching a strong bore, whereas they are weaker and smaller for $log(\chi) \approx -5$, approaching a weak plunging breaker. However, once the observation is ascribed to a breaker type, its vertical position is determined, and all the observations ascribed to the same breaker type, are located on the corresponding horizontal line. The value of $log(\chi)$ determines their ubication on the x-axes and furthermore the separation between them. The resulting plot is the consequence that the classification is based on transitional intervals of the breaker types, whereas observed reality progresses more gradually.

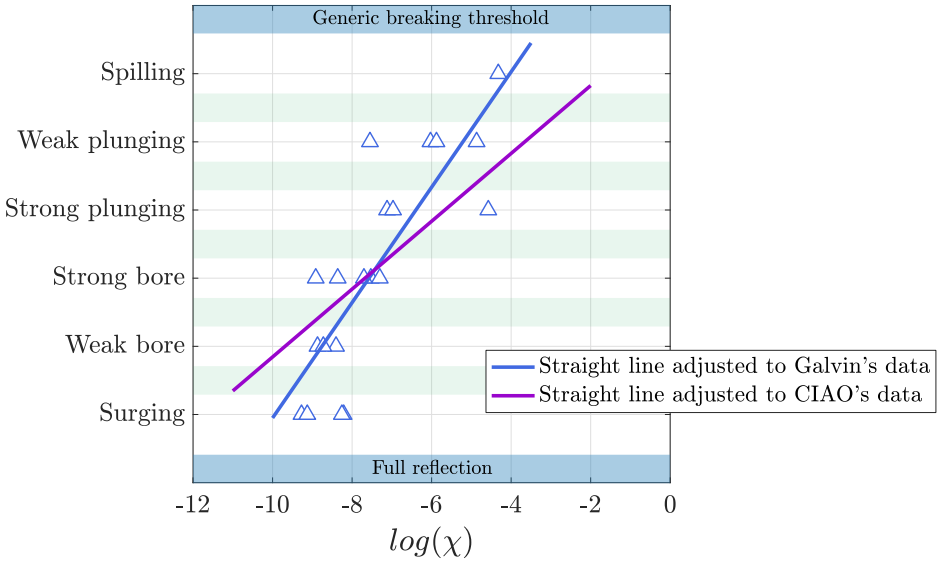


FIGURE 4.7: Specific breaker types from Galvin (1968) for 1:10 slope adapted by Moragues et al. (2020b) (S=S, WB=collapsing, SB=plunging ARW and plunging, SPl=plunging, WPl= WD plunging and Sp=Sp) and the fitted straight line to the data (see Figure 3.4b). For comparison the fitted straight line (see Figure 4.6b) to the CIAO data is included.

The straight lines fitted to the observed breaker types (i.e. Figures 4.4b, 4.5b, and 4.6b) are assumed to be the geometric locus of the continuous process triggered by the corresponding set of experimental input (i.e. Figures 4.4a, 4.5a, and 4.6a). Therefore, to fulfil the continuous hypothesis, the observed breaker types of each dataset (i.e., blue line in Figure 4.6a) should be on a straight line, (i.e., blue line in Figure 4.6b). The position of each datum on the x-axis should not change, as determined by $log(\chi) = log(h/L \cdot H_I/L)$.

Figure 4.9(a) shows the observed breaker types (blue line in Figure 4.6b), displaced up or down depending on their $log(\chi)$ value to locate them on the straight line. Analogously, Figure 4.9(b) shows the breaker types observed by Galvin on a 1:10 slope (blue line in Figure 4.7), moved up or down, depending on their $log(\chi)$ value to locate them on the straight line.

In summary, for a given slope, there is a functional relationship between the fitted line in the experimental space (i.e., Figures 3.4a and 4.6a) and the straight line determining the progression of breaker types in function of $log(\chi)$ (Figures 4.9a and b).

On the other hand, non-dimensional run-up and run-down, and the relative amount of wave energy that can be reflected off a slope are dependent on the breaking processes and the attendant energy dissipation (Battjes, 1974). Díaz-Carrasco et al. (2020) and Moragues et al. (2020b) also verified this dependence for plane permeable, rough slopes. Consequently, if the experimental goal is to model flow characteristics (Bayle et al., 2020) or energy transformation (Baquerizo et al., 1998) while a wave train impinges on the ramp of a given slope, $m$, the experimental design for dimensional analysis should include a complete set of value pairs for $h/L$ and $H_I/L$, which makes it possible to identify the continuous progression of the possible breaker types. Accordingly, the observed progression of breaker types is specific of the value of $m$. Alternatively, the experimental technique can be based on testing

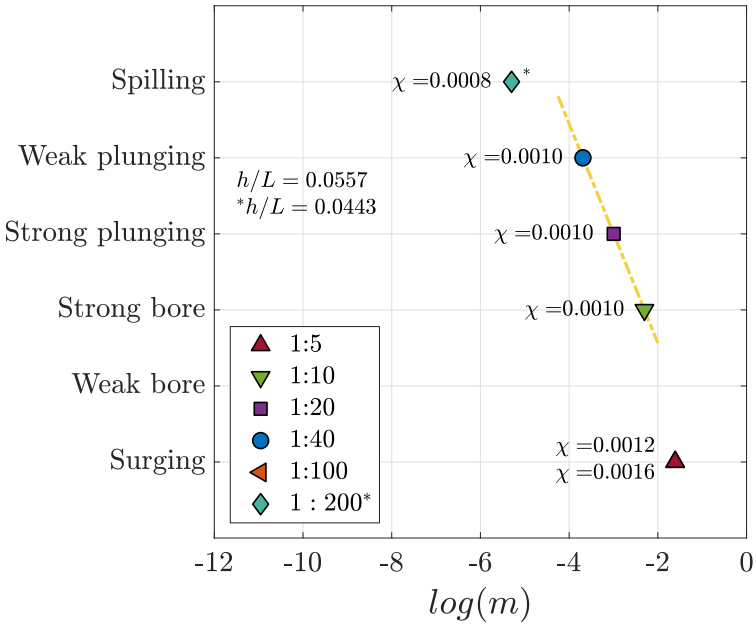


FIGURE 4.8: Breaker types from Derakhti et al. (2020) adapted to Moragues et al. (2020b). The values of $\chi$ are given next to each point. The yellow line connects the three data with constant value of $\chi$.

pairs of values of $m$ and $H_I/L$, for a given $h/L$. The observed progression of breaker types is then specific of the chosen value of $h/L$. The application of this method of experimental design, experimental technique, and data analysis should help to effectively attain those objectives.

## 4.5 Estimated energy dissipation for the observed wave breaker types

The wave energy conservation equation is formulated in a Control Volume (CV) extending landwards from the toe of the slope to the shoreline: the spatial variation in the CV of the time-averaged wave energy fluxes is equal to the amount of wave-averaged energy dissipated per unit area, $(D_*)_{CV}$, $(J/(m^2 s))$ , in the CV (Baquerizo et al., 1998) can be estimated with Equation 4.1.

$$\frac{1}{l}\left(\mathcal{F}_I - \mathcal{F}_R\right)_{x_{toe}} + \left(D_*\right)_{CV} = 0 \tag{4.1}$$

where, $\mathcal{F} = EC_g = ECn = E\frac{\omega}{k}f(kh)$, $(J/(ms))$, is the time -averaged wave energy flux per unit surface at the toe of slope, $x_{toe}$ , and the subindexes $I$ and $R$ denote the incident and the reflective wave train, respectively. The fluxes in and out at the shoreline, $x_{top}$, are assumed to be zero; $l = h\cot\alpha$ is the horizontal length of the CV; and $h$ is the water depth at the toe of the slope. Note that all the tests were carried out with the slope $m$ =1:10. Only the energy of the most progressive incident and reflective wave trains were considered. The equation can be expressed in non-dimensional quantities (Equation 4.2).

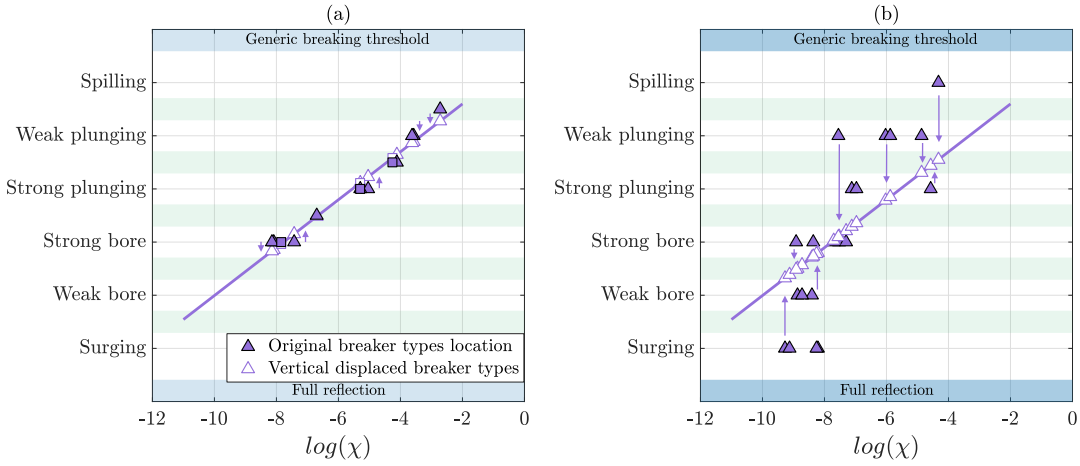


FIGURE 4.9: Breaker types versus $log(\chi)$ for a 1:10 slope, (a) present data (CIAO flume) from Figure 4.6(b), (b) Galvins data, 1:10 slope from Figures 3.4(b). and 4.7. The vertical location of the data are modified to fulfil the continuous hypothesis of breaker type progression. For purposes of comparison, breaker types have been adapted to Moragues et al. (2020b), based on the original descriptions of the authors.

$$1 - K_R^2 + d_* = 0 \tag{4.2}$$

where $K_R^2$ is the module of the reflection coefficient for the most progressive mode in the wave train, defined as the quotient of the reflected and incident wave energy fluxes per unit surface area, and $d_*$ is the non-dimensional energy dissipation rate (Equation 4.3).

$$d_* = \frac{(D_*)_{CV}}{\frac{1}{8}\rho g H_I^2 C_g} l \tag{4.3}$$

Similarly to the wave breaker type analysis, it is hypothesized that $(D_*)_{CV}$ can be described as a function of the characteristics of the incident wave train: the relative water depth and the wave steepness $(h/L,\ H_I/L)$, at the toe of the slope. Thus, $(D_*)_{CV}$ could be parametrized following Duncan (1981) and Martins et al. (2018), but expressing $C$, $C_g$, $H_I$ and $T$ at the toe of the slope (Equations 4.4 and 4.5) where $B_S$ is a bulk dissipation coefficient.

$$(D_*)_{CV} \approx B_S \frac{\rho}{g} C^5 \tag{4.4}$$

$$d_* = B_s \frac{8l}{g^2} \frac{C^5}{H_I^2 C_g} \tag{4.5}$$

Figure 4.10 shows the non-dimensional bulk coefficient, $B_S$ versus $\log(\chi)$. Depending on the wave breaker types, two regions can be identified. For small values of $\log(\chi) \leq -6$, the reflected wave energy flux modulates the wave evolution over the slope. $B_S$ increases slightly as the breaker type progresses from surging to weak

and strong bore. For large values of $\log(\chi) > -6$, the dissipation by breaking prevails over the reflected energy flux. $B_S$ increases its value as the breaker type progresses from strong bore to strong and weak plunging. Unfortunately, there are not enough numerical data for spilling breakers but despite this, the slope of the straight line is not expected to change. The equation for $d_*$ can be modified to make explicit the dependence of the wave period, wave steepness, and relative water depth at the toe of the slope.

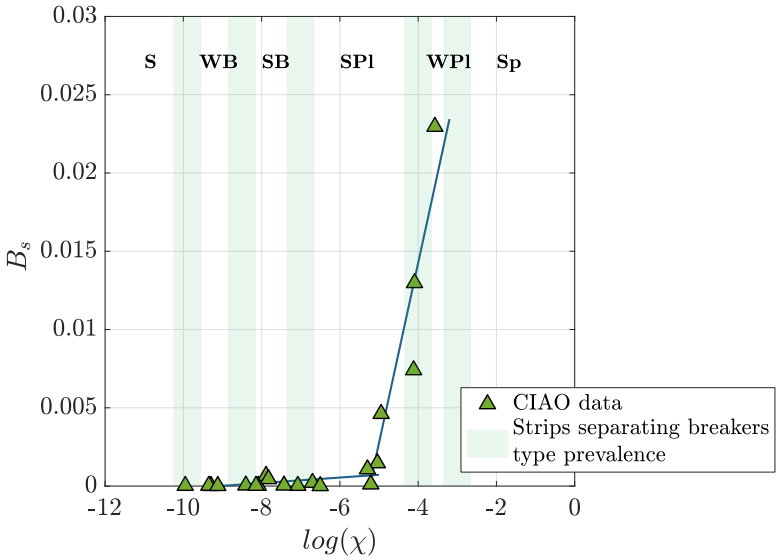


FIGURE 4.10: Bulk dissipation coefficient $(B_S)$ versus $log(\chi)$. Two lines fitted to the data points show the relation between the coefficient and $\chi$. The green lines indicate the transition between breaker types.

## 4.6 Conclusions

The progression of breaker types observed inside the experimental space defined by the parallelogram of blue dashed sides was determined by the curve connecting the experimental wave input. In this Chapter, straight lines (Equation 3.4), drawn in the experimental space, were used. For each input straight line there is a corresponding output straight line, which relates the progression of breaker types and $log(\chi)$. As the wave steepness and relative water depth increases (Figure 4.4a), there is a continuous gradation in the type of breaking from surging to spilling. The actual observation of breaker types depends on the initial value pairs of $h/L$ and $H_I/L$ selected, the experimental space, and the slope of the straight line (Equation 3.4). Furthermore, when wave steepness decreases and relative water depth increases but $\chi$ remains constant, the breaker type does not change (green line in Figure 4.6a). In other words, there is no progression of breaker type.

Since the classification of breaker types is discontinuous, the data assigned to each type were placed on horizontal lines, depending on the value of $log(\chi)$. Because the breaking of a wave train on a smooth slope is assumed to progress continuously, the location of the displaced data was corrected to satisfy that assumption. The line thus obtained establishes, for a given slope ($m$ =1:10), a linear relationship between the continuous progression of breaker types and the value of $log(\chi)$. There is a functional relationship between the sets of the experimental space and those of the

breaker types. Thus, the breaker types included in the extended classification should be considered as milestones in the continuous wave breaking process on a plane impermeable slope.

# 5 Flow characteristics on smooth impermeable slopes

**Comment**

The results of this section had been submitted to *Journal of Geophysical Research: Oceans*:

Losada M.A.; **Moragues, M.V.**; and Clavero, M. (2021). "Flow characteristics on steep, plane and impermeable slopes and beaches. The dependence on the alternate slope similarity parameter and relative wave height: $\chi$ and $\gamma$".

*"Water and air, the two essential fluids on which all life depends, have become global garbage cans."*

Jacques Yves Cousteau

*Based on dimensional analysis, the alternate slope similarity parameter has been used to analyze the flow characteristics on a plane, smooth and rough impermeable slope. This parameter, as mentioned before, is directly related with the breaker types, and it is capable of defining both, run-up and run-down, for a given slope angle. The largest deviations of the experimental data use to occur at the transitions between breakers, mostly between weak bore - strong bore - strong plunging, as they are located in the transition zone. Moreover, a sigmoid function has been fitted to the run-up, run-down and total water excursion, giving a reasonably good result with the variable* $(h/L)(H_I/L)$*, however, a poor fit is obtained when the Iribarren number is taken as the independent variable. In this Chapter the goals to be achieved are (a) to relate the flow characteristics to the breakers types; (b) to be able of predicting those parameters as a function of* $\chi$*; and (c) to relate the total water excursion in the slope with the bulk dissipation coefficient* $(D^*)$ *or its complementary value, the reflection coefficient* $(K_R^2)$.

## 5.1 Introduction

The hydrodynamic performance of natural and man-made sloping coastal structures depends on their interaction with the incident wave train. Generally speaking, its quantification should account for the time-averaged continuity, momentum and energy conservation equations under regular or irregular wave trains. It should provide the flow characteristics above the still water level, wave run-up height ($Ru$), wave run-down height ($Rd$), and mean water level ($\overline{\eta}$) and overtopping, and the wave energy transformation, incident and reflected wave energy fluxes and the time averaged energy dissipation over the slope (Kobayashi et al., 2008).

The maximum height the water reaches over a slope, also called run-up ($Ru$), and its corresponding fall, or run-down ($Rd$), measured vertically from mean water level at rest, define the maximum and minimum height the wave reaches above and below mean level in each wave cycle. Both are relevant factors for the design of breakwaters, due to the damage and costs they can generate. If the maximum run-up is higher than the breakwater crest, the structure will suffer overtopping.

The prediction of the run-up allows us to know the overtopping volume that can, potentially, surpass the structure crest, estimated as the water wedge that exceeds that level. This is important because overtopping is the primary hydraulic factor for the design of the crest level of sea structures. The higher the crest level, the more expensive the structure. That is why an accurate prediction of the run-up is essential to the economic design of breakwaters.

Wave run-up is usually formed by two parts: wave set-up ($\eta$), which is the mean water surface elevation; and the swash (Figure 5.1). Wave set-up is a result of the momentum transfer of the radiation stress cross-shore gradient due to breaking waves, and consists of a mean and an oscillating component (Longuet-Higgins and Stewart, 1964). Set-up varies across the surf zone, being slightly negative at the wave break point and increasing to a maximum above the still water level. The swash is constituted by a part of the incident wave and by another part of the infragravity waves (Pinault et al., 2020).

To analyze wave run-up and run-down without considering the influence of the mean set-up, the parameter *total water excursion* has been proposed. This parameter is the sum of the run-up and absolute value of run-down ($Ru + |Rd|$).

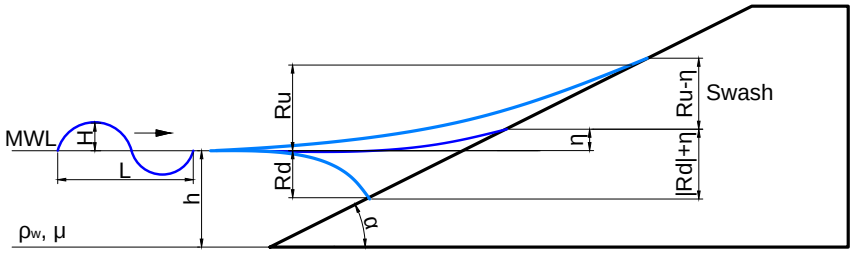


FIGURE 5.1: Scheme of the geometrical parameters affecting run-up and run-down in an impermeable slope.

### 5.1.1 State of art

In practical coastal engineering, the water flow characteristics on a slope are determined by applying semi-empirical formulas. Most of them use the Iribarren number (Iribarren and Nogales, 1949) as an independent variable (Equation 3.2). It has been shown that the breaking type and the flux characteristics occur within certain Iribarren number values (Iversen, 1952; Galvin, 1968; Battjes, 1974). Since Battjes (1974), practically every run-up and run-down formula follows this conjecture (Ahrens and McCartney, 1975; Bruun and Günbak, 1977b; Losada and Giménez-Curto, 1981; Van Der Meer and Stam, 1992).

Nowadays, the formulas used for estimating the run-up and run-down in the idealized scenario of waves breaking on a smooth impermeable slope only use the slope angle and the wave steepness as main variables affecting the processes.

One of the first attempts to estimate the run-up was done by Miche (1944), who proposed a formula for estimating the dimensionless run-up from non-breaking waves. Hunt (1959) proposed an experimental formula for breaking and non-breaking waves, where the run-up is proportional to the Iribarren number (Equation 3.2). Losada and Giménez-Curto (1981), Hughes (2004) and Hsu et al. (2012) proved how this formula work well for lower values of Ir. However, Losada and Giménez-Curto (1981) and Sawaragi et al. (1982) proved it causes high dispersion of the data for values $Ir > 2$.

Losada and Giménez-Curto (1981) came up with three formulas to estimate the run-up on smooth slopes valid for a wider range of $Ir$. They proposed an exponential fit model for the prediction of the maximum run-up for regular wave trains, and through the equivalence hypothesis, obtained that the run-up fits reasonably well into a Rayleigh distribution. The random nature of the flow design parameters ($Ru$ and $Rd$) as well as the set-up ($\eta$), promoted, in practical maritime engineering, the use of statistics obtained on an experimental basis, and their subsequent adjustment of a function depending on the characteristics of the wave and the level, for example $Ru_{2\%}$.

Allsop et al. (1985) identified *"an uncertainty in the prediction of run-up levels on smooth slopes of the order of 30%"*. More than 35 years after, this has not been significantly reduced.

Hughes (2004) proposed to estimate wave run-up on smooth, impermeable slope using the maximum, depth-integrated momentum flux occurring in a wave at the toe of the slope. In the derived general formula, the relative run-up $(Ru/h)$ is directly proportional to the square root of wave momentum flux parameter, i.e. the

maximum wave momentum flux non-dimensionalized with $\rho_w g h^2$. Hughes's formula has three relevant differences with the classical formula depending on Iribarren number: (1) the vertical scale is the water depth at the toe of the slope instead of the wave height, (2) the nondimensional form of wave momentum flux (first order wave theory) is expressed as a function of the relative wave height $(H_I/L)$, and the relative water depth $(h/L)$, and (3) it included an unknown function of slope that needed to be determined empirically for each slope. The weaknesses of Hughes's formula (his figure 7, Ahrens data impermeable smooth slope, irregular waves) is that, (1) data exhibited two distinct trends that seemed to be delineated by the wave steepness, and appears to represent transition of breaker type from nonbreaking/surging breakers to plunging/spilling breakers; and (2) for any given value of the momentum flux parameter, the values of $Ru_{2\%}/h$ varied more than double, and for, small values of the parameter, more than four times.

Madsen and Fuhrman (2008) analyzed the data from Ahrens and McCartney (1975) through the $Ru_{2\%}$. The proposed setting assumes the existence of a maximum value of run-up at $Ir \approx 3$ . However, the scattering observed in the interval $Ir = [2 - 4.5]$ is not acceptable in practical engineering. In order to solve this uncertainty, the adjustment functions have incorporated "partial" coefficients that "quantify" the statistical variability with a representative value (Van Der Meer, 1988; Van Gent, 2001; Melby, 2012; Capel, 2015; Plant and Stockdon, 2015; Arana, 2017; Khoury et al., 2019).

Most of the formulas continue using the Iribarren number as the principal parameter governing the problem and they exhibit good behavior with dissipative wave breaking (spilling and weak plunging breakers), but exhibit poor behavior for dissipative-reflective breakers (strong plunging and strong bore), and reflective wave breakers (weak bore and surging), regardless whether the slope is smooth, rough or armored, impermeable or permeable. Guza et al. (1985) found that run-up on beaches respond to three regimes: (i) a reflective regime; (ii) a saturation regime and (iii) an intermediate regime. Gomes da Silva (2019) adapted these three regimes to describe the incident swash masured on natural beaches.

For the development of present research it is relevant that most of the formulas, in addition to the dependence on $Ir$ (by definition on the slope), include (1) the slope through an specific term yielding run-up parametrization based on Hunt's equation (Hunt, 1959), and, following Battjes's conjecture (2) do not include the flow the relative water depth $(h/L)$.

Equation 5.1 shows the recommended run-up formula for rouble mound breakwaters given by EurOtop (2018), where $\gamma$ are adjustment coefficients depending on the presence of a berm, roughness and the wave angle attack.

$$\frac{Ru_{2\%}}{H_{m0}} = 1.65\, \gamma_b\, \gamma_f\, \gamma_\beta\, \xi_{m-1,0} \tag{5.1}$$

The relation between the run-up, the wave energy transformation process and wave breaker types is implicit in the relationship of these parameters with the Iribarren number. Some authors have mention this relation (Galvin, 1968; Battjes, 1974; Bruun and Günbak, 1977a; Muttray et al., 2006; Buccino et al., 2018), however, it is not yet fully understand or described.

Taking into account the results of Chapter 3 about wave breaker types, this chapter is devoted to analyze the flow characteristics (run-up y run-down) on the slope

through numerical tests and data from previous studies and relate them to the type of wave breaking in an impermeable smooth slope.

## 5.2 Experimental set-up and data from other authors

This study is based on the following experimental data for $Ru$, $Rd$ and $\eta_m$ obtained: (1) from experimental tests done in the CIAO wave flume with an impermeable smooth ramp; (2) from numerical tests carried out in the IH-2VOF model (Lara et al., 2008) on a sloping breakwater with an impermeable, rigid slope; and (3) from other published papers: Mase and Iwagaki (1984), Mase (1989) and Broekhoven (2011).

### 5.2.1 Atmosphere-Ocean Interaction Flume

The Atmosphere-Ocean Interaction Flume (CIAO) is equipped with two piston-type generating paddles, equipped with active systems to absorb reflection and a closed circuit for wind generation. For this study, an impermeable ramp was installed with two slopes angles: 1:5 and 1:10 (in the study area, Figure 5.2). The water depth was keep constant at h=0.5 m. Video and photograph cameras were used to record the different types of breaking. A video camera was installed over the ramp to measure wave run-up and run-down. The test conditions are summarized in Table 5.1.

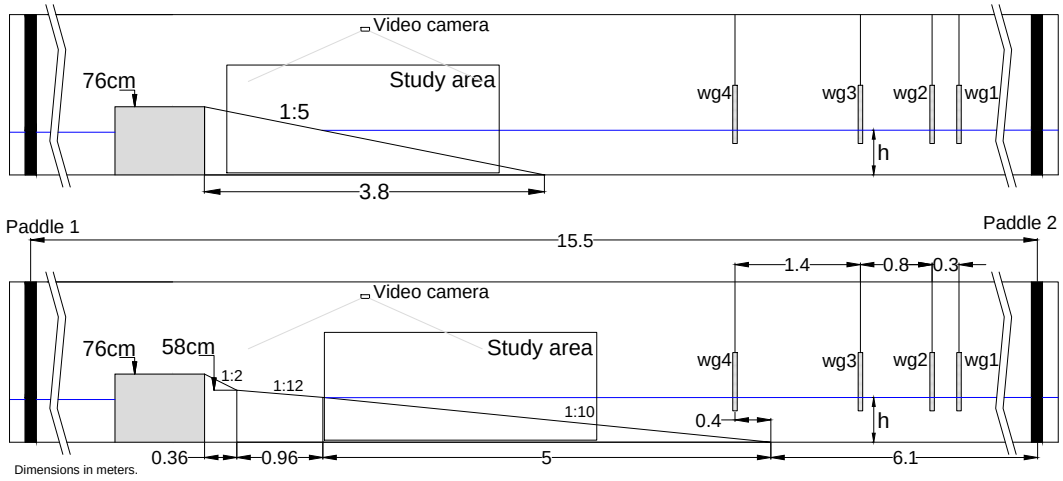


FIGURE 5.2: Diagram of the CAIO wave flume and wave gauges position for the 1:10 slope (measurements in meters).

TABLE 5.1: Summarized test conditions of the tests carried out at the CIAO wave flume. $H_I$ is the incident wave height, $T$ is the mean wave period, $Ir$ is the Iribarren number or surf similarity parameter, $h$ is the water depth at the toe of the structure and $\overline{Ru}$ is the mean run-up value.

| Parameter | A | B |
|---|---|---|
| $\boldsymbol{tan(\alpha)}$ | 1/5 | 1/10 |
| $\boldsymbol{H_I}(m)$ | 0.008 - 0.15 | 0.0050 - 0.1864 |
| $\boldsymbol{T}(s)$ | 0.94 - 5.01 | 0.9494 - 5.0051 |
| $\boldsymbol{H_I/L}$ | 0.0008 - 0.094 | 0.0005 - 0.1041 |
| $\boldsymbol{Ir}$ | 0.3466 - 3.7938 | 0.3058 - 4.1260 |
| $\boldsymbol{h}(m)$ | 0.5 | 0.5 |
| $\overline{\boldsymbol{Ru}}(m)$ | 0.0137 - 0.45000 | 0.0050 - 0.1244 |

### 5.2.2 Numerical set-up

The IH-2VOF numerical model (Lara et al., 2008) is based on the 2DV Reynolds Averaged Navier-Stokes (RANS) equations based on the decomposition of the instantaneous velocity and pressure fields in a two-dimensional domain. The flow inside the estructure is solved using the Volume-Averaged Reynolds Averaged Navier-Stokes (VARANS) equations. These equations are obtained when the RANS equations are integrated in a control volume. The volume of fluid (VOF) method is followed to compute free surface. Wave conditions are introduced in the model, imposing a velocity field and a free surface time evolution on one side of the numerical domain. The IH-2VOF model has been widely validated (Lara et al., 2011; Maza et al., 2013; Guanche et al., 2015; Vílchez et al., 2016a; Formentin and Zanuttigh, 2018).

The current-wave flume of the IISTA laboratory was reproduced in the numerical model. The numerical set-up was calibrated by Vílchez et al. (2016a). It has a uniform grid on the y-axis with a cell size of $5mm$ and three regions on the x-axis: (a) the generation region with a cell size from $8mm$ to $5mm$; (b) the central region (where the slope is located) with a constant cell size of $5mm$; and (c) a third region with a cell size from $5mm$ to $10mm$. The total number of cells in the numerical domain is $2993x201$. All the setups were run with the reflection absorption activated in the generation paddle. Moreover, active wave absorption was used at the generation boundary and at the end of the flume to simulate the dissipation ramp.

A non-overtoppable, smooth and impermeable slope was tested under regular waves. Two different slope angles were simulated: 1:5 and 1:10. The free surface output was recorded with 8 wave gauges located along the flume (Figure 5.3). Tests were performed to cover the maximum area of the experimental space. Tests conditions are summarized in Table 5.2.

### 5.2.3 Data from other authors

#### Mase and Iwagaki (1984) and Mase (1989)

Mase and Iwagaki (1984) and Mase (1989) conducted laboratory tests on smooth slopes in a 27 $m$ long, 0.5 $m$ wide and 0.75 $m$ deep wave flume. They used four slopes between 1:30 and 1:5 under irregular waves generated with a Pierson-Moskowitz spectrum. Their articles do not mention the use of active reflection absorption or

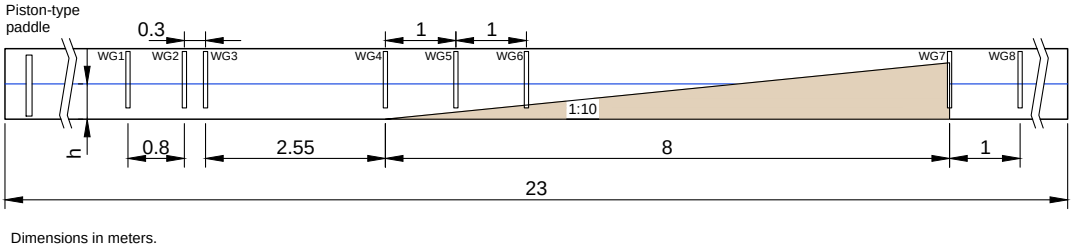


FIGURE 5.3: Diagram of the IH-2VOF tested model and wave gauges position for the 1:10 slope (measurements in meters). The position of the wave gauges for the 1:5 are the same referenced to the toe of the slope.

TABLE 5.2: Summarized test conditions of the tests carried out at the numerical model IH-2VOF. $H_I$ is the incident wave height, $T$ is the mean wave period, $Ir$ is the Iribarren number or surf similarity parameter, $h$ is the water depth at the toe of the structure and $\overline{Ru}$ is the mean run-up value.

| Parameter | A | B |
|---|---|---|
| $\boldsymbol{tan(\alpha)}$ | 1/5 | 1/10 |
| $\boldsymbol{H_I}(m)$ | 0.0116 - 0.1354 | 0.0031 - 0.2131 |
| $\boldsymbol{T}(s)$ | 0.9124 - 5.0019 | 0.8016 - 5.0036 |
| $\boldsymbol{H_I/L}$ | 0.0012 - 0.813 | 0.0008 - 0.0673 |
| $\boldsymbol{Ir}$ | 0.7377 - 6.6288 | 0.4325 - 4.0075 |
| $\boldsymbol{h}(m)$ | 0.5 | 0.35, 0.4 |
| $\overline{\boldsymbol{Ru}}(m)$ | 0.0107 - 0.2220 | 0.0045 - 0.1457 |

second-order wave correction. The test conditions are summarized in Table 5.3. Wave and run-up were recorded with resistance wave gauges. Mase (1989) included several statistics of the signal, such as $Ru_{max}$ and $\overline{Ru}$, among others.

TABLE 5.3: Summarized test conditions of the tests carried out by Mase and Iwagaki (1984) and Mase (1989). $H_{m0}$ is the energy-based wave height, $T_p$ is the peak wave period, $H_{m0}/L_{0p}$ is the wave steepnees, $Ir$ is the Iribarren number or surf similarity parameter, $h$ is the water depth at the toe of the structure and $\overline{Ru}$ is the mean run-up value.

| Parameter | Series A | Series B | Series C | Series D |
|---|---|---|---|---|
| $\boldsymbol{tan(\alpha)}$ | 1/5 | 1/10 | 1/20 | 1/30 |
| $\boldsymbol{H_{m0}}(m)$ | 0.039 - 0.11 | 0.029 - 0.11 | 0.026 - 0.101 | 0.026 - 0.099 |
| $\boldsymbol{T_p}(s)$ | 0.84 - 2.39 | 0.84 - 2.29 | 0.92 - 2.28 | 0.82 - 2.25 |
| $\boldsymbol{H_{m0}/L}$ | 0.004 - 0.058 | 0.004 - 0.059 | 0.003 - 0.063 | 0.004 - 0.066 |
| $\boldsymbol{Ir}$ | 0.83 - 3.02 | 0.41 - 1.65 | 0.20 - 0.85 | 0.13 - 0.56 |
| $\boldsymbol{h}(m)$ | 0.45 | 0.45 | 0.45 | 0.4 |
| $\overline{\boldsymbol{Ru}}(m)$ | 0.03 - 0.107 | 0.026 - 0.058 | 0.026 - 0.035 | 0.0138 - 0.0306 |

**Van Broekhoven (2011)**

Similarly, Broekhoven (2011) conducted a series of experimental tests to study the influence of structure permeability on run-up. Tests were carried out in the wave flume of the water laboratory at Delft University of Technology and it has 45 $m$ long, 0.80 $m$ wide and 0.95 $m$ deep. Four different typologies with different material

sizes and grading of both the core and the armor layer under regular and irregular waves generated with a Jonswap spectrum and active reflection absorption were tested. Test conditions are summarized in Table 5.4. The run-up analysis has been done with the regular waves while the irregular waves have been used to compare them. In this Chapter, the data corresponding to a smooth, impermeable slope has been used. Resistance gauges and simultaneous video camera records were used to measure the run-up. The water depth at the toe of the breakwater was sufficient to ensure that no waves were broken before they propagated on the slope. To separate the incident and reflected wave trains, the n-sensor method by Zelt and Skjelbreia (1992) was applied. The experimental output is the mean run-up of the record.

TABLE 5.4: Summarized test conditions of the tests carried out by Broekhoven (2011). $H_{m0}$ is the energy-based wave height, $T_p$ is the peak wave period, $sH_{m0}/L_{0p}$ is the wave steepnees, $Ir$ is the Iribarren number or surf similarity parameter, $h$ is the water depth at the toe of the structure and $\overline{Ru}$ is the mean run-up value.

| Parameter | Series 1 | Series 2 |
|---|---|---|
| $\boldsymbol{tan(\alpha)}$ | 1/1.5 | 1/2 |
| $\boldsymbol{H(m)}$ | 0.066 - 0.136 | 0.063 - 0.151 |
| $\boldsymbol{T(s)}$ | 1.20 - 2.40 | 0.90 - 3.56 |
| $\boldsymbol{H/L}$ | 0.0138 - 0.0444 | 0.0089 - 0.0705 |
| $\boldsymbol{Ir}$ | 3.30 - 7.60 | 1.90 - 8.42 |
| $\boldsymbol{h(m)}$ | 0.5 | 0.5 |
| $\boldsymbol{\overline{Ru}(m)}$ | 0.110 - 0.350 | 0.123 - 0.366 |

### 5.2.4 Hydrodynamic flow regimes of the analyzed data

The Ursell number (Equation 5.2) is a non-dimensional parameter used to classified the different wave movements. It serves to define the regime to which the waves correspond and, therefore, is usually used to select the wave theory that describes better a wave motion. It is also a measure of the nonlinearity of the waves. A linear wave will have an Ursell parameter such that $Ur = O^1$.

$$Ur = \frac{L^2 H}{h^3} \tag{5.2}$$

The theories describing the waves movement are approximations to reality. They can adequately describe those phenomena whose conditions satisfy the hypotheses adopted in their derivation. Le Méhauté (1976) proposed a graphical representation to analyze the limits of validity for several wave theories depending on three parameters: the wave height $(H)$, the water depth $(h)$ and the wave period $(T)$. The wave theories studied where, among others, the linear theory by Airy (1845) or the non-linear theory proposed by Stokes (1847). Figure 5.4 represents all the analyzed data within the limits of validity for various wave theories (Le Méhauté, 1976).

As it can be seen in the diagram, for waves in shallow areas with a small significant wave height, it is more convenient to use the Cnoidal theory. However, if the wave breaking zone is approached, when the ratio of significant wave height to depth is approximately equal to 0.8, it is more convenient to use the $5^{th}$ order Stokes theory. In intermediate wave zones, it is observed that, depending on the value of the parameters, it is necessary to work with the Linear Theory, the Stokes theory of

$2^{nd}$ order or higher orders. For areas of high relative depth, the most appropriate theory will also depend on the value of the parameters.

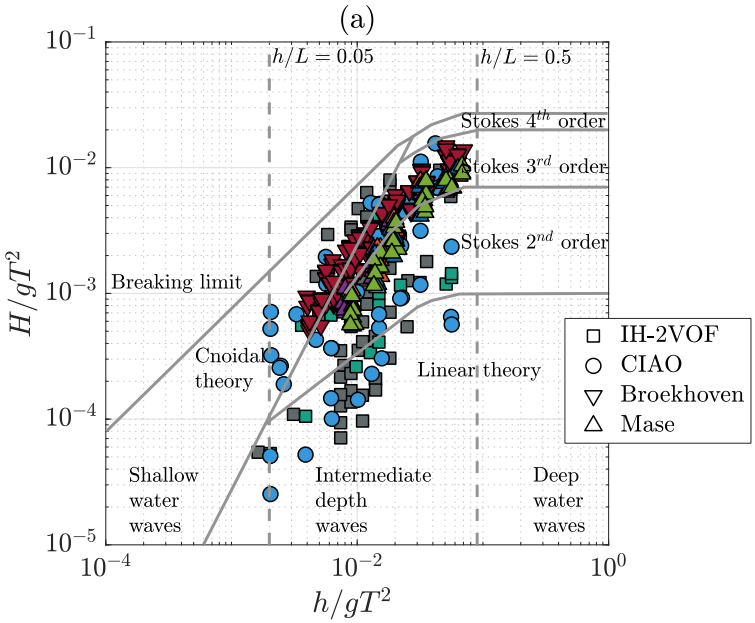


FIGURE 5.4: Data from the experimental tests done at the CIAO wave flume, IH-2VOF numerical model and from the other authors represented together with the limits of validity for various wave theories (Le Méhauté, 1976). Symbols represent each dataset while colors are given for each slope angle.

Figure 5.4 shows that the second and third-order Stokes theory range applied to most of the data from other authors (Broekhoven, 2011; Mase, 1989) and the analytical solution should contain at least the second power term proportional to $H^2$ that is characteristic of the non-linear behavior. The data from the IISTA, both from the CIAO wave flume and from the IH-2VOF numerical model, is more spread out on the abacus, from linear theory to Stokes $3^{rd}$ order. This may be due to the wide variety of periods and wave heights tested to fill the experimental space (described in Section 3.4). This figure shows the main differences between the analyzed datasets, being a first sample of the possible differences found in the analysis, when all the data were treated in the same way.

## 5.3 Experimental flow characteristics results

This section presents and analyzes the run-up measurements obtained on a flat, smooth and impermeable slope in the CIAO wave flume and in the numerical model IH-2VOF simulating the IISTA-UGR wave-current flume, for two slopes: 1:5 and 1:10. In addition, the observations of the wave break type and its progression as a function of the combination of $h/L$ and $H_I/L$ values according to the classification of Moragues and Losada (2021) and the time series of the free surface in three sensors placed between the generating paddle and the toe of the slope are available.

Based on dimensional analysis, as seen in Chapter 2, if the slope is plane, impermeable, smooth and non-overtoppable and $Re$ is large enough to admit that the flow in the slope is fully turbulent, the functional is simplified as seen in Equation 5.3

between the observed dimensionless variables ($Ru$, $Rd$, $\eta_m$) and the dimensionless values of the variables governing the problem.

$$\frac{X}{H_I} = \left(\frac{Ru}{H_I}, \frac{Rd}{H_I}, \frac{\eta_m}{H_I}\right) = f_\alpha \left(\frac{H_I}{L}, \frac{h}{L}, 2sinh\left(\frac{2\pi h}{L}\right)\frac{k_N}{H_I}\right) \tag{5.3}$$

For each slope angle, the functional relationship depends specifically on the roughness of the bed surface. The walls and bottom of the CIAO wave flume are glass and the slope surface is smooth wood. The numerical model was programmed so that the slope and walls would not generate resistance. Under these conditions it can be admitted that, globally, the dissipation in the boundary layer is negligible compared to the dissipation due to the wave train breaking, at least for the breaker types: spilling, weak and strong plunging and strong bore. For surging breakers the hypothesis may not be valid. Thus, the functional relationship of the relative flow characteristics depend only on three quantities (Equation 5.4): (1) the characteristics of the incident waves at the toe of the slope, $h/L$ and $H_I/L$; and (2) the slope, $m$. The interplay of these three quantities is most accurately and usefully represented by graphic representations in a 2D system in terms of value pairs (taken two by two) while the other quantity remains constant (Chapter 4).

$$\frac{X}{H_I} = \left(\frac{Ru}{H_I}, \frac{Rd}{H_I}, \frac{\eta_m}{H_I}\right) = f_\alpha\left(\chi\right) \tag{5.4}$$

This result differs from the one proposed by Battjes (1974), who eliminated the relative water depth ($h/L$) and kept a relation of the slope angle with the wave steepness.

### 5.3.1 Experimental space and breaker types

Figure 5.5 show the experimental space of the physical and numerical experiments run on each of the two slopes angles: 1:5 and 1:10. The vertical axis is the natural logarithm of the relative depth and the horizontal axis is the natural logarithm of the incident wave steepness, both calculated at the toe of the slope. This graphical representation allows for quantifying and comparing the sample space covered by the tests and, where appropriate, explaining any discrepant results. The parallelogram indicates the flume generation limits of wave height and wave period. For completeness, the maximum wave steepness curve of a regular train propagating along a horizontal bottom according to the formulation of Miche (1944) is included.

It can be observed that, for the two slopes, the points are distributed along the interior of the parallelogram. However, it does not include tests at shallow depths, $log(h/L) < -3.2$, nor with very small wave steepness, $log(H_I/L)$ at intermediate depths $[-3.0 < log(h/L) > -1.0]$. Nor is the region near the Miche's breaking curve homogeneously occupied. This Figure proves that, as the slope gets steeper, the transition moves to lower values of relative water depth and the wave steepness, being more difficult to observe dissipative wave breakers.

Figure 5.5, in addition to the data code, identifies the type of breaking observed, according to the classification of Moragues et al. (2020b): S = surging, WB = weak bore, SB = strong bore; SPl = strong plunging, WPl = weak plunging and Sp =

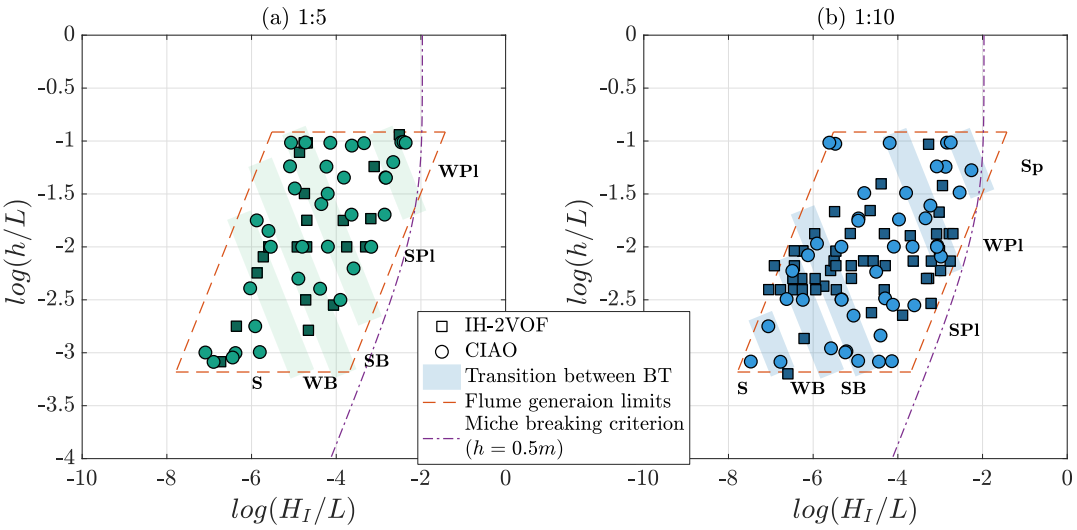


FIGURE 5.5: Experimental space $[log(H_I/L) - log(h/L)]$ classified by slopes (a) for a 1:5 slope and (b) for a 1:10 slope; from the numerical experiments performed at the IH-2VOF and the experimental tests done at the CIAO wave flume. The orange parallelogram indicates the wave flume generation limits.

spilling. A photographic series of the observed breakage types is included in Appendix B. The green/blue bands determine the transition zone between breaker types. It should be highlighted that the bands follow straight lines with constant values of the relative water depth ($h/L$) and incident wave steepness ($H_I/L$), and that the location of the breaker type transitions is specific of each slope, 1:10 and 1:5. Thus, with slope 1:5, in approximately one-quarter of the parallelogram surface (the lower left side, "South West") the wave trains "break" in surging, even with $log(H_I/L) \approx -4$. However, in the 1:10 slope, the surging breakers are located at the lower corner of the parallelogram and progress to WB and SB as the wave steepness increases, namely for $log(H_I/L) > -7.5$ and $log(h/L) < -2.5$. On the other hand, the spilling breakers could only be observed at slope 1:10.

In summary, to identify the breaker types on a slope, both the relative depth of the wave train and the wave steepness at the toe of the slope are needed. In addition, those depend on the slope steepness. Consequently, to characterize the water flow on the slope due to wave train breaking, it is necessary to consider both $h/L$ and $H_I/L$ at the toe of the slope.

### 5.3.2 Relative run-up versus the alternate similarity parameter

Figure 5.6 (a) and (b) represent the values of the observed run-up (dimensioned with the incident wave height, $Ru/H_I$) versus the log-transform of $h/L \cdot H_I/L$. Each point represents a test run with a height, $H$ and period $T$, and a sufficient number of waves (more than 100). $Ru$ is the mean of the observed values, after eliminating those corresponding to the start and stop of the test. With this design and this experimental technique, the values observed in each of the tests form a statistically independent sample.

For the two slopes, the relative run-up decreases with surging breakers as $log(H_I/L)$ and/or $log(h/L)$ decreases, namely for the 1:10 slope and $log(\chi) < -9.5$, and for the 1:5 slope and $log(\chi) < -8.3$. This differential behavior of the surging breakers will

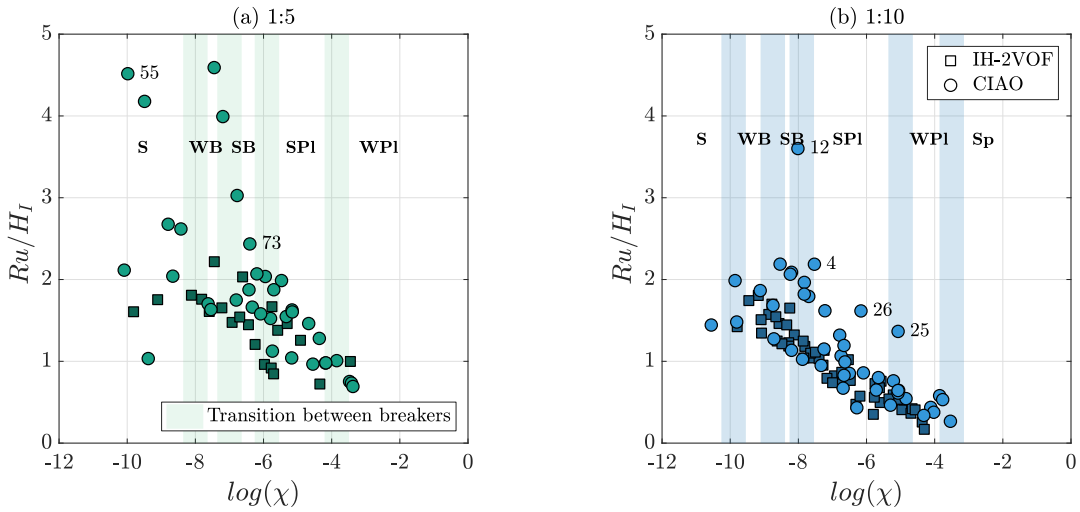


FIGURE 5.6: Non-dimensional run-up against $log(\chi)$, obtained from IH-2VOF and the CIAO wave flume for (a) 1:5 slope and (b) 1:10 slope. The vertical bands indicate the transition between breakers observed in the physical flume.

be discussed further on, in particular, whether it was induced (or conditioned) by the experimental conditions.

The highest values of relative run-up occur with breakers in WB and SB. The maximum values were observed with slope 1:5, $Ru/H_I \lesssim 4.5$; with slope 1:10, the maximum values are $Ru/H_I \lesssim 2.2$ (except one point with $Ru/H_I \approx 3.75$ wich produced overtopping). In some runs the water sheet overtopped the ramp crest in the CIAO wave flume; with slope 1:5, it occurred in runs [55, 73], so $Ru/H_I > 2.5$; with slope 1:10 the overtopping was observed in runs [4, 12, 25, 26] and $Ru/H_I > 1.5$. Around the maximum values, small changes of $log(\chi)$ cause very important reductions of the relative run-up. Moving away from this zone, in the transition from SB to SPl and from SPl to WPl breaker types, as $log(\chi)$ increases, the relative run-up values decrease overall with a lower rate of change than in the maximum zone.

When the break type is WPl or is in the transition from WPl to Sp, as $log(\chi)$ grows, the rate of change of $Ru/H_I$ is significantly smoothed. In the 1:10 slope, from $log(\chi) > -4.5$, the experimental values converge asymptotically to a constant value of $Ru/H_I \approx 0.20 - 0.30$, confirming that the $Ru$ contribution is essentially due to mean sea level. Likewise, in the 1:5 slope, $log(\chi) > -4.0$, convergence of the experimental data is observed. However, the smallest value $Ru/H_I \approx 0.75$ is still far from the expected asymptotic value $0.20 - 0.30$. To observe this value, it would have been necessary to generate wave trains breaking at spilling, $(H_I/L) > 0.135$ and at depths $h/L > 0.37$, with a global value of $log(\chi) > -3.0$.

### Relative run-up variation for each type of wave breaker

Regardless of the overall behavior of the relative run-up while varying $log(\chi)$, it is relevant to analyze its variability for each specific breaker type or constant value of $\chi$ . In the 1:10 slope, the transition from SB to SPl was observed in the $log(\chi) \approx -8$ band. In slope 1:5, this transition was observed in the $log(\chi) \approx -6$ band. In both cases the $Ru/H_I$ value grows while increasing $H_I/L$, and decreasing $h/L$.

Similarly, in the central zone of the SPl break domain, in slope 1:10 in the $log(\chi) \approx -7$ band and in slope 1:5 in the $log(\chi) \approx -4$ band, is observed that the $Ru/H_I$ value grows with decreasing $h/L$ and increasing $H_I/L$. For large depths, $log(h/L) \geq -1.5$ as $H_I/L$ grows, $Ru/H_I$ grows little or may even decrease slightly. In summary $Ru/H_I$ varies for each type of breaking and between different types of breakers.

Besides, in Figure 5.6, it can be seen a considerable difference between the data obtained from physical and numerical experiments. It can be assumed that all these differences come from the "incorrect" simulation of the numerical model of each type of breaker, without taking into account the differences between them, such as the different turbulent scales generated, the shapes of each break, the interaction with the descending water sheet or the generation of lateral or edge waves.

### 5.3.3 Interplay of the relative wave height, $H_I/h$, in the observed run-up

The variability for the same type of breaking was well known and, after Battjes (1974), it was described as a function of the surf similarity parameter, $\xi$ (or Iribarren's parameter, $Ir$) defined by the ratio between the slope gradient and the square root of the wave steepness ($H_I/L_0$), where $L_0$ is the wavelength at indefinite depths and $H_I$ the wave height of the incident train at the toe of the slope. Numerous laboratory and field experimental data indeed confirm the dependence of $Ru/H_I$ on $H_I$ for small values of the surf similarity parameter, with breakers in spilling and eventually in WPl (Ahrens, 1981). With breakers in SPl, SB, WB and S, the dependence deteriorates significantly (scatter becomes greater). Essentially the breaker zone changes from fully dissipative to intermediate and fully reflective (Guza et al., 1985). The reflected energy flux is comparable to the energy dissipation and the relative depth at the toe of the slope cannot be ignored.

Hughes (2004) is one of the few publications that does not rely on the conjecture of Battjes (1974) to analyze the run-up in an impermeable slope. According to his approach, for a given slope, the run-up dimensioned with the depth at the toe of the slope, $Ru/h$, depends on the relative wave height $\gamma = H_I/h$, and the relative water depth, $h/L$, calculated at the toe of the slope, but not on the incident wave steppness $H_I/L$. In the context of this work, the relative wave height at the toe of the slope is determined by the quotient of the wave steppness and the relative depth. There is, therefore, a relationship between the values of $\chi$ and $\gamma$ (Equation 5.5).

$$\chi = \gamma \left(\frac{h}{L}\right)^2 \tag{5.5}$$

It has been shown that each type of wave breaker at the slope occurs at a constant value of $\chi$. Therefore, if $H_I/L$ is increased, $h/L$ must decrease and $\gamma$ must increase. Therefore, to observe in the laboratory all possible values of $Ru/H_I$ with each type of wave breaking, it is necessary to increase $H_I/h$. If the depth of the test is constant, increasing $\gamma$ increases the height $H$, but without changing the type of breaking. Because of the larger dimensions of $H$, the breaker may be perceived as more "violent" but retains the characteristics that determine its type of breaking.

Unfortunately, wave generation in a laboratory wave flume is limited to a maximum value of this parameter, both for regular and irregular waves $H_{m0,I}/h$ and therefore at the toe of the slope. It is noteworthy that Ahrens et al. (1993) and Hughes

(2004) already questioned (*"we are not really certain"*) the behavior of the empirical $Ru/H_I$ formulas obtained in the laboratory for application in design conditions.

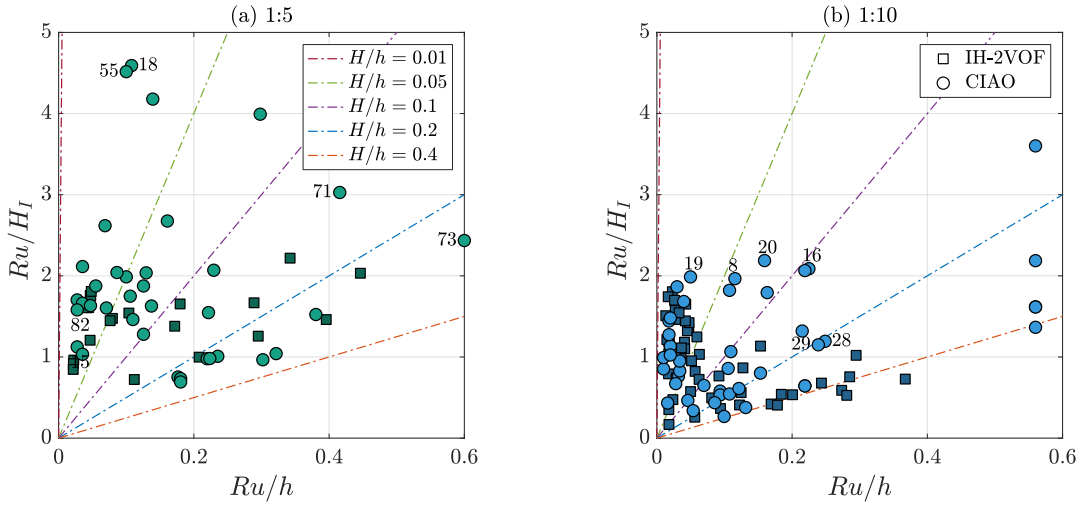


FIGURE 5.7: Non-dimensional run-up ($Ru/H_I$) versus the relative run-up ($Ru/h$), obtained from IH-2VOF and the CIAO wave flume for (a) 1:5 slope and (b) 1:10 slope. The dotted lines represent the isolines of $H/h$.

Figure 5.7 plots $Ru/h$ versus $Ru/H_I$ obtained in the numerical model and the CIAO wave flume for a 1:5 slope (a) and a 1:10 slope (b). The generation and propagation depth until the toe of the slope was kept constant in the physical and numerical tests. $Ru/h$ is the observed run-up divided by a constant value, directly proportional to the dimensional value of the run-up. For each experimental point, the value of $\gamma$ is obtained directly by dividing the value of the abscissa by the value of the point's ordinate. Thus, the dotted lines represent the geometric locus of the constant $\gamma$ value, and equal to 0.01, 0.05, 0.1, 0.2 and 0.4 rotating clockwise, respectively.

The maximum $Ru$ values observed on the 1:5 slope are points 71 and 73, $Ru/H_I \approx 3$ and 2.5, and $\gamma \approx 0.14$ and 0.25, respectively. The first point lies at the transition between WB and SB; the second breaks as SB. On the other hand, the maximum values of the measured relative run-up are points 18 and 55, with $\gamma \approx 0.024$ and 0.022, and breaks as WB and S, respectively. The antithesis are points 15 and 82 which break as SPl, $Ru/H_I \approx 0.6$ and 1.05, and $\gamma \approx 0.024$ and 0.017. The largest wave does not have to produce the largest relative run-up value or its largest dimensional value. The breaker type is a necessary and convenient indicator-predictor for analyzing both the dimensional and relative run-up value.

In the case of the 1:10 slope a majority of points located in the $log(H_I/L) < -6$ region of the sample space were tested with small values of $\gamma$, in the interval $0.005 < \gamma < 0.05$. Many of these tests had high $Ru/H_I$ values and small $Ru/h$ values. The largest $Ru/H_I$ values $\approx 2$ (without taking the points with overtopping into account), were observed with breaks at the WB-SB transition and $0.05 < \gamma < 0.10$, points 19, 8, 20, 16. The highest $Ru$ values were observed with breaks at SPl, $\gamma \approx 0.2$, points 28 and 29.

On the other hand, by means of the dotted lines in Figure 5.7 (a) and (b), it is possible to observe the same value of $Ru/H_I$, with different types of breaker by varying the value of $\gamma$ or $\chi$. Similarly, to observe the same dimensional $Ru$ value.

For example, in Figure 5.7 (a), for the series of points around $Ru/H_I \approx 1.6$ value, the wave breaking changes from WB to SPl, $[-7.8 < log(\chi) < -5.5]$ and $[0.01 < \gamma < 0.30]$. Similarly, for $Ru/h = 0.22$, ($Ru = 0.11$), $[1 < Ru/H_I < 2.1]$, breaks in SPl and SPl-SB, $[-3.8 < log(\chi) < -5.0]$ and $[0.1 < \gamma < 0.25]$. In both cases, the relative depth changes as well (see Figure 5.5). In addition, the ranges of the values depend on the slope angle.

## 5.4 Review of the development of empirical formulas

According to Battjes (1974), in the 80's and 90's of the last century, many researchers conducted extensive series of laboratory tests to develop run-up formulas with regular and irregular waves on smooth impermeable and permeable slopes as function of Iribarren number, Mase (1989), Van Der Meer and Stam (1992), Broekhoven (2011) or Kreyenschulte et al. (2020), among others.

It is usual to design and run these experiments by choosing pairs of values of $H_I$ and $T$ with one of the following three criteria. First, for a given slope and water depth, a test series is run with a constant value of wave period and several runs with different wave heights, chosen to cover the most probable values of the Iribarren number (Van Der Meer, 1988); under these conditions, $h/L$ is kept constant. A second criterion is to execute tests and their respective runs with a constant value of $Ir$; the increases of $H_I$ in each run must be accompanied by an increase of the wave period and, consequently, by a reduction of the relative depth, $h/L$. Finally, a third criterion, possibly the most classical, is to run runs with different pairs of $T$ and $H$ values that cover specific $Ir$ values and different types of breaking.

The design and execution of the experiments in the CIAO wave flume and numerical tests, depart from the usual criteria: (1) a parallelogram is developed from the experimental space, the sides of which are determined according to the dimensions of the wave flume and the capacity of the system to generate the frequencies associated with wind waves, (2) the experimental points are selected and grouped considering the bands with the same type of breaking (constant $\chi$) and with the same relative wave height (constant $\gamma$) and (3) the run-up and run-down are measured in the slope, and the free surface is recorded in at least three points between the generation paddle and the toe of the slope to estimate the reflected energy flux and the bulk dissipation on the slope.

The experimental space, Figure 5.8, is the geometric location of the experimental points defined by their coordinates: wave steepness and relative water depth. The sides of the parallelogram determine the boundaries of the wind wave generation system in the flume, for a given geometry and slope characteristics. The three usual experimental input selection criteria ($H_I$ ,$T$) are represented in the experimental space by a line grouping the experimental points satisfying a relationship between relative depth and wave steepness:

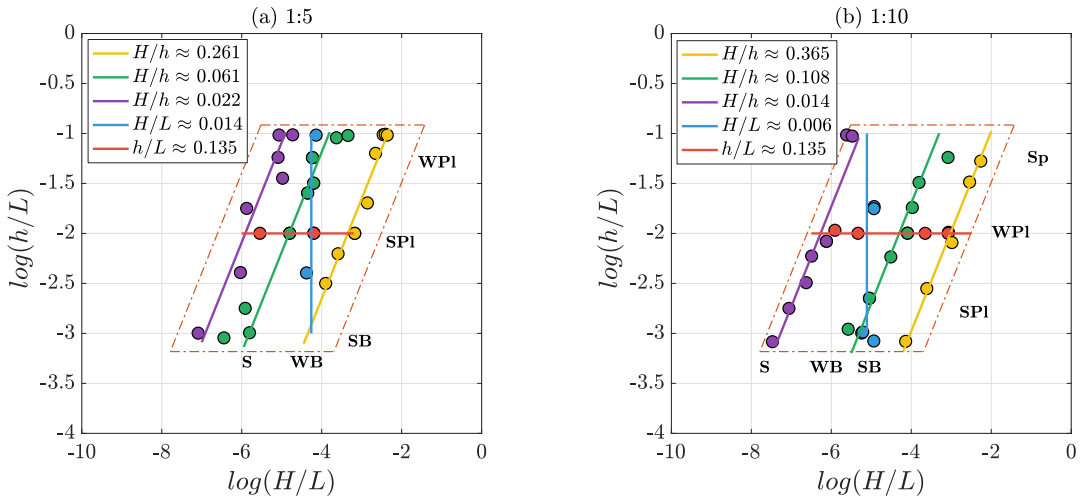


FIGURE 5.8: Lines fitted to the points of the experimental space with constant values of $H/h$, $H_I/L$ and $h/L$ for the CIAO data.

$$Y = a \cdot X + b \tag{5.6}$$

$$Y = log\left(\frac{h}{L}\right)$$

$$X = log\left(\frac{H}{L}\right)$$

Usually, the first criterion, (constant $h/L$), is represented by a horizontal line parallel to the abscissa axis. The second criterion, (constant $H_I/L$ or $Ir$), is represented by a vertical line parallel to the ordinate axis. In the third criterion, the experimental line is a diagonal to the parallelogram that links points at shallow water, small values of $h/L$ and $H_I/L$ (surging breakers) with higher values of $h/L$ and $H_I/L$ (spilling breaks). The orientation of the diagonal changes when connecting points in shallow water and large wave steepness (SB, WB and eventually surging) with points in intermediate or deep water and low wave steepness (SPl, WPl and eventually spilling).

In summary, for each geometry and slope angle $m$ of the slope, the experimental space helps to identify the values of the main parameters, ($h/L$, $H_I/L$) and to choose, depending on the generation system, the values of the runs in each test series considering the type of breaking, $\chi$, and the relative wave height, $\gamma$.

### 5.4.1 CIAO experimental data, 1:5 and 1:10 and fitting curves according to different groupings

The density of experimental points obtained from the CIAO wave flume experiments and their reasonably homogeneous distribution in the exxperimental space (Figure 5.5) for comparative purposes, allows the experimental data to be grouped with any of the usual criteria used to develop and propose empirical formulas. Figure 5.8 depicts, (a) 1:5 and (b) 1:10, respectively, different linear groupings of experimental points, namely, constant $h/L$, constant $\xi$ or $H_I/L$, constant break type (*chi*),

constant relative height ($\gamma$), and a generic diagonal of points with different *chi* and $\gamma$. Figure 5.9 represents the fitting curves, (a), (c) 1:5, and (b), (d) 1:10, respectively, of the experimental values of $Ru/H_I$ as a function of the log-transform of $\chi$ for each of the groupings, (a) and (b) constant $\gamma$; (c) and (d) constant $h/L$ and constant $\xi$.

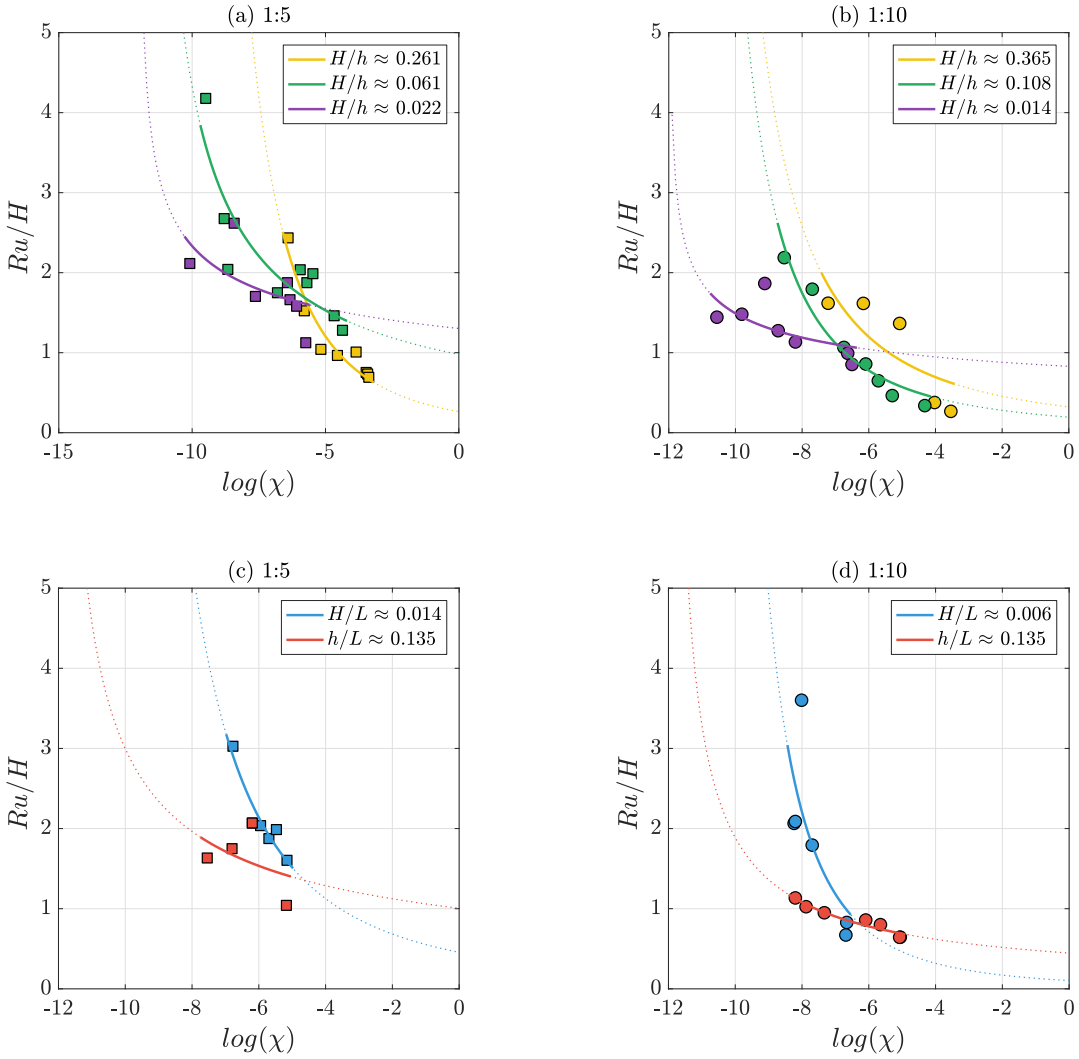


FIGURE 5.9: Non-dimensional run-up ($Ru/H_I$) against $log(\chi)$, obtained from the CIAO wave flume for (a) 1:5 slope and (b) 1:10 slope. The lines represent constant values of $H/h$, $H_I/L$ and $h/L$.

In summary, it is observed that, (1) depending on the grouping of experimental data, the fitting curves result in different formulas; (2) the maximum values of $Ru/H_I$ depend on the types of breakers tested (values of constant $\chi$) and on the relative wave height conditioned by the generation limits, in this case in a horizontal background, (values of constant $\gamma$); (3) the maximum value of the relative run-up occurs with breakers in the WB and SB transition, and in general, do not coincide with the maximum values of dimensional $Ru$ ($Ru/h$, with $h = 0.50m$).

On the other hand, both the experiments with surging breakers (long waves) and with WB and SB breakers, with high values of wave steepness, are severely conditioned (limited) by the generation system, confirming the doubt raised by Ahrens et al. (1993) and revisited by Hughes (2004). The difference between the values predicted by the fitting curves (empirical formulas) and the observed values can be very

TABLE 5.5: Fit parameters for the power function fitted to the relative run-up, against $log(\chi)$ in Figures 5.9, being the numbers of the table the order of the values in the figure legend.

| $\mathbf{y = a \cdot x^b}$ | | | | | |
|---|---|---|---|---|---|
| **1 : 5** | | | | | |
| | 1 | 2 | 3 | 4 | 5 |
| **a** | 241.1 | 7.698 | 2.922 | 116.4 | 4.573 |
| **b** | -2.825 | -0.830 | -0.325 | -2.231 | -2.231 |
| **1 : 10** | | | | | |
| | 1 | 2 | 3 | 4 | 5 |
| **a** | 35.62 | 27.88 | 1.871 | 105.2 | 3.294 |
| **b** | -1.894 | -1.999 | -0.327 | -2.789 | -0.804 |

significant.

### 5.4.2 Experimental formulas for random wave run-up on impermeable smooth slopes, Mase (1989)

Mase and Iwagaki (1984) and Mase (1989) conducted experiments in a physical wave flume on run-up oscillations over four (here we only analyze two) impermeable smooth slopes 1:5 and 1:10 under irregular waves attack. The output of each test is a sample of individual run-up heights measured vertically from the still water level. Based on these experimental data, Mase (1989) proposed a formula that relates the relative run-up statistical descriptor, $Ru^*$, to the Iribarren number or surf similarity parameter, $\xi$, as Equation 5.7.

$$\frac{Ru}{H_0} = a_M \xi^{b_M} \tag{5.7}$$

The exponent $b_M$ and the constant $a_M$ depend on: (1) the statistical descriptor and (2) on the slope angle. $H_0$ is the significant wave height in deep water and the surf similarity parameter, $\xi$, is calculated from the wave steepness at undefined depths, $H_0/L_0$. The characteristics of the experiment are described in Mase and Iwagaki (1984) , where $H_0$ is explicitly stated to be the wave height of the incident train.

Figure 5.10 shows, (a) the experimental space of the tests performed on a 1:5 slope as a function of the wave steepness and the relative depth of the incident train calculated at the toe of the slope, (c) the relative run-up calculated with the statistical descriptor $\overline{Ru}$ as a function of $log(\chi)$ and (e) the pairs of $Ru/H_I$ and $Ru/h$ values, with isolines of $\gamma = H/h$. In addition, the transition bands between the different breaker types adapted from the CIAO wave flume (regular swell) experiments are approximately plotted. In Figure 5.10 (b), (d), and (f) the same parameters are plotted for the 1:10 slope.

It can be seen that Mase's tests were performed with intermediate depths $[0.1003 \leq h/L \leq 0.4066]$, with low values of wave steepness $[0.0067 \leq H_{m0,I}/L \leq 0.0550]$ and relative wave height in the interval $[0.0672 \leq H_{m0,I}/L \leq 0.2466]$. According to the transition bands between breakers, the 1:10 slope only produces tests with WB and SB breakers, while the 1:5 slope included some runs with WB and SB breakers.

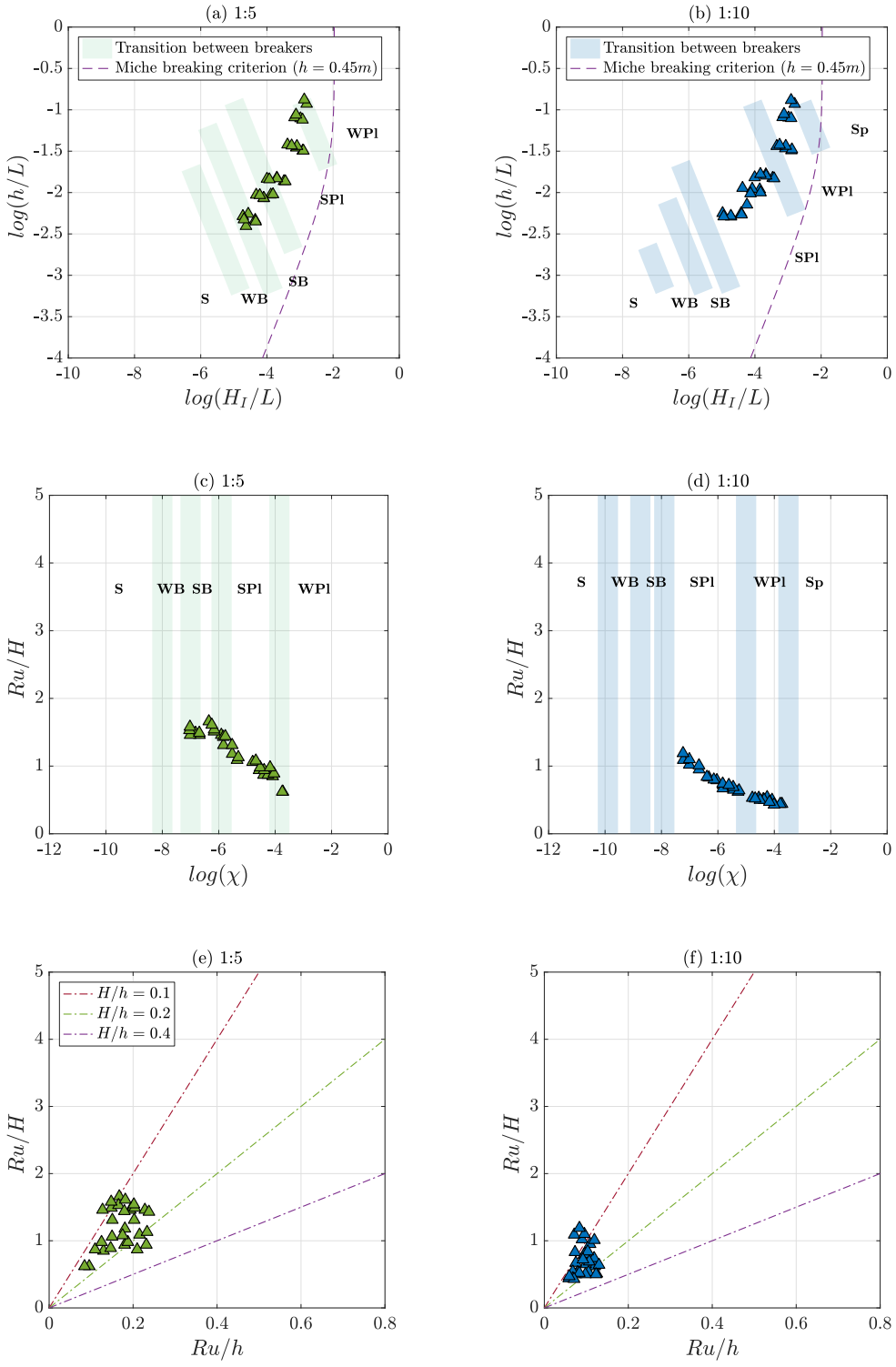


FIGURE 5.10: (a) and (b) Experimental space; (c) and (d) non-dimensional run-up versus $log(\chi)$ and (e) and (f) non-dimensioanl run-up versus the relative run-up for Mase's data for impermeable smooth slopes. The dashed lines represent the breaking criterion by Miche (1944) and the bands represent the transition between breakers observed at the CIAO wave flume for the same slope angle.

Although there may be some doubts about the relationship between the significant wave height, $H_s$, used in the tests of Mase and Iwagaki (1984) and the mean wave height of a regular train (Rayleigh's distribution $H_{I,regular} \approx 0.6H_s$) it is convenient to compare those results with those obtained in the CIAO wave flume. It is observed that, for the 1:5 slope the Mase line joining the experimental points lies between the green and yellow lines in Figure 7 a and b. The $Ru/H_I$ values reasonably coincide in the interval $log(\chi) > -7$. However, Mase's experimentation "lost" the $Ru/H_I$ values $> 2$ by running tests with low values of $\gamma < 0.25$, and not testing the S, WB and SB breaker types. The same conclusion is obtained when comparing the results for the 1:10 slope. These coincide in values and distribution with those obtained in the CIAO wave flume in the interval $[-8 < log(\chi) < -3.8]$, and $[\gamma < 0.11]$. Likewise, Mase's experimentation "lost" the values of $Ru/H_I > 1.2$ when experimenting with low values of the relative wave height.

In summary, it is observed that for the two slopes, (1) the experimental space tested by Mase and Iwagaki (1984) is a linear diagonal that does not include all breaker types, (2) does not include shallow water conditions, and (3) the relative wave heights are small to have guarantees that the tests represent design conditions.

### 5.4.3 Experimental formulas for regular wave run-up on impermeable smooth slopes, Broekhoven (2011)

Broekhoven (2011) conducted a series of experimental tests to study the influence of structure permeability on run-up. His Appendix B gives the wave data and measurements of every performed test: (B1) smooth impermeable and (B2) rough impermeable slopes (1:1.5 and 1.2). The experimental output is the mean run-up ($\overline{Ru}$) of the record. In addition, the last column of the table of experimental results provides the type of breaking observed, S = surging, C = collapsing and P = plunging.

Figure 5.11 plots: (a) and (b) the experimental space of the tests with a 1:2 and 1:1.5 slope, respectively, as a function of the wave steepness and relative depth of the incident train calculated at the toe of the slope, (c) and (d) the relative run up calculated with the statistical descriptor $\overline{Ru}$ as a function of $log(\chi)$, and (e) and (f) the pairs of $Ru/H_I$ vs $Ru/h$ values, with the isolines of $\gamma = H/h$.

Notice that not all the data included in Broekhoven table B.1 are included in Figure 5.11. Broekhoven (2011) excluded those data points because, cannot be analyzed correctly due to the generation of cnoidal waves, and the analysis is based in linear wave theory. Agreeing with that opinion, strictly speaking, indeed none of the experiments fullfil linear theory. However the calculated output, at least for regular wave trains, is consistent with overall output of the experiments. In cases of repeated runs the point is represented by the average value. The averaged runs are (the numbers are those in table B.1): 1, 2, 3, 6, 9, 9, 13, 14, 15, 35, 36, 37, 40. The points with only one run are 7, 34, 38, 41, 43 and 44.

It is noted that the tests with 1:2 slope angle were performed at intermediate depths $[0.0672 \leq h/L \leq 0.4066]$, with small wave steepness, $[0.0082 < H_I/L < 0.0608]$, and relative wave height in the interval $[0.11 < H_I/h < 0.29]$. In the case of 1:1.5 slope angle, the experimental intervals were, $[0.09h/L0.25]$, $[0.0150 < H_I/L < 0.0450]$ and $[0.12 < H_I/h < 0.29]$.

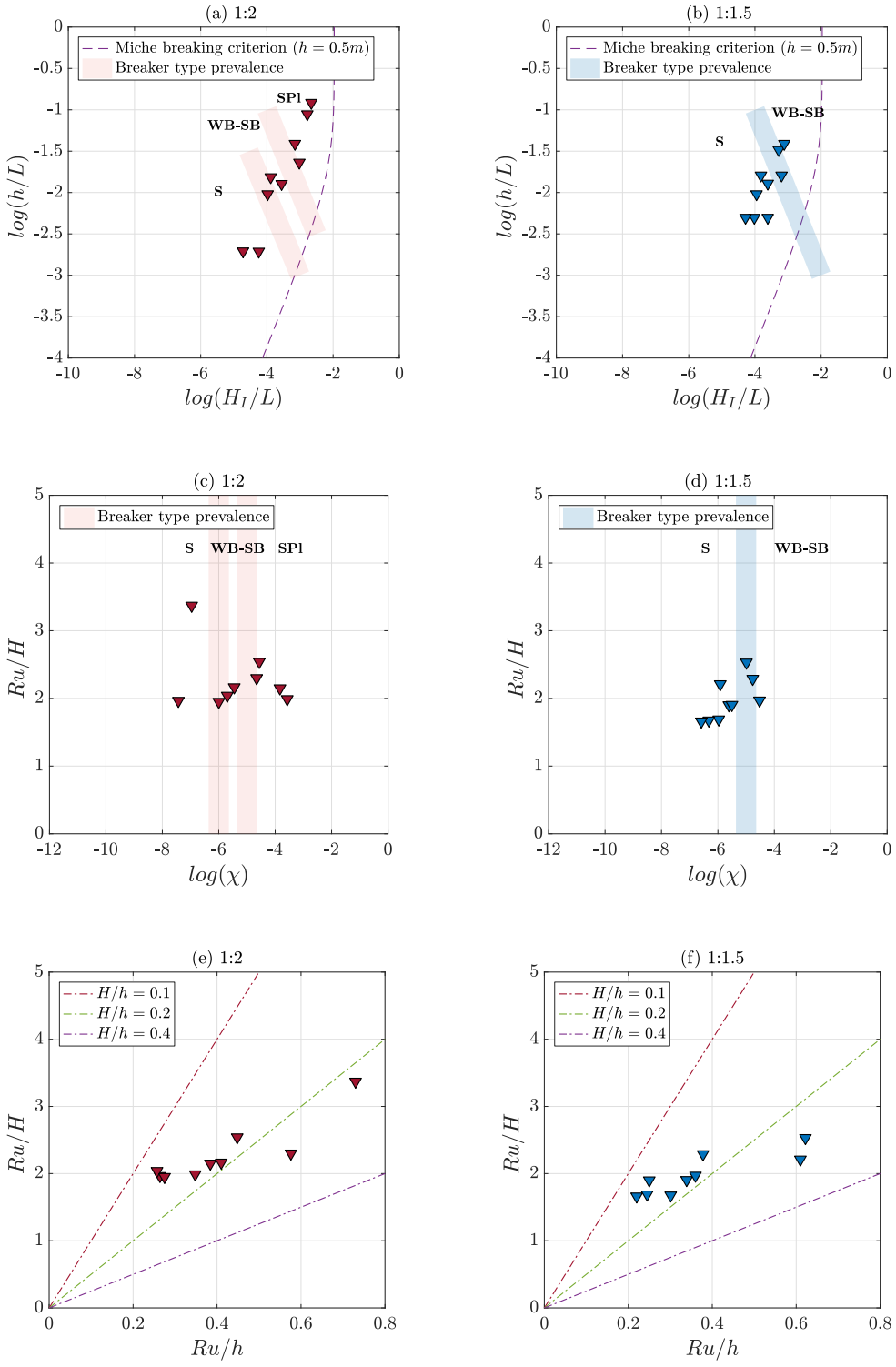


FIGURE 5.11: (a) and (d) Experimental space; (d) and (e) non-dimensional run-up versus $log(\chi)$ and (c) and (e) non-dimensioanl run-up versus the relative run-up for Broekhoven's data for smooth impermeable smooth slopes. The dashed lines represent the breaking criterion by Miche (1944) and the bands represent the expected transition between breakers.

Included in the Figures are the transition bands of the breaker types, constant, drawn from his Appendix B data. When the data provided is collapsing, it is identified in the figure as WB-SB; and when it is plunging, it is identified by SPl. In the 1:2 slope, S, WB-SB and SPl breaks were observed and in the 1:1.5 slope only S and WB-SB were observed.

The line joining the experimental input data values, $Y = aX + b$ (Equation 5.6), is relatively close to the breaking limit curve at the toe of the slope. However, one may wonder whether the experimental space includes a sufficient number of points to ensure that the experimental results represent the most extreme $Ru/H_I$ and $Ru/h$ conditions for either slope angle. After analyzing the data obtained in CIAO wave flume in Figure 5.6, it appears that it would have been possible to observe higher values of relative run-up if runs with $H_I/L > 0.09$ wave steepness were included in the range of relative depths $[0.12 < h/L < 0.22]$ that produce WB-SB and eventually SPl breakers. To fill this area of the experimental space, it is necessary to increase the value of $\gamma$ to values closer to the limits of the generating system. In addition, in order to obtain more data with higher $Ru/H_I$ values, it would have been desirable to fill in the same range of relative depths the region with lower wave steepness than those of the experimental line.

In summary, the lack of data in the region between $log(H_{s,I}/L) > -4$ and the breaking limit curve at the toe of the slope fuels doubts about the representativeness of the formula obtained with the experimental results of Broekhoven (2011) for design conditions.

## 5.5 Breaker types and wave energy transformation

### 5.5.1 Relative run-down versus the alternate similarity parameter

Figure 5.12 shows run-down data for two slopes of 1:5 and 1:10 obtained from the numerical model and physical CIAO wave flume. The experimental space is shown in Figure 5.5. $Rd$ is the average value on the slope obtained from the series of run-down data provided by the numerical model and recorded in the slope of the physical slope. Again, the run-down is aligned according to $log(\chi)$. The minimum value of $Rd$ (positive values) seems to be indicative of the transit from Sp to WPl and SPl. The SB, WB and S breakers produce lower values of run-down, as it happened (symetrical) with the run-up.

The higher variability appears for both slopes for the SB - SPl, in the interval $[-8 \leq log(\chi) \leq -4]$ for the 1:5 slope and $[-9 \leq log(\chi) \leq -6]$ for the 1:10 slope. As explained in the previous sections, these variability is related with the relative wave height $\gamma = H/h$, and the position of the points in the experimental space.

### 5.5.2 Relation between the total water excursion and the wave energy transformation

Figure 5.13 shows the non-dimensional total water excursion on the slope, $(Ru + |Rd|)/H_I$ obtained from the numerical model and the physical tests as a function of $log(\chi)$. Maximum values are obtained in the interval $log(\chi) < -8$, while minimum values occur at $log(\chi) > -4$. These maximum values depend on the slope and the

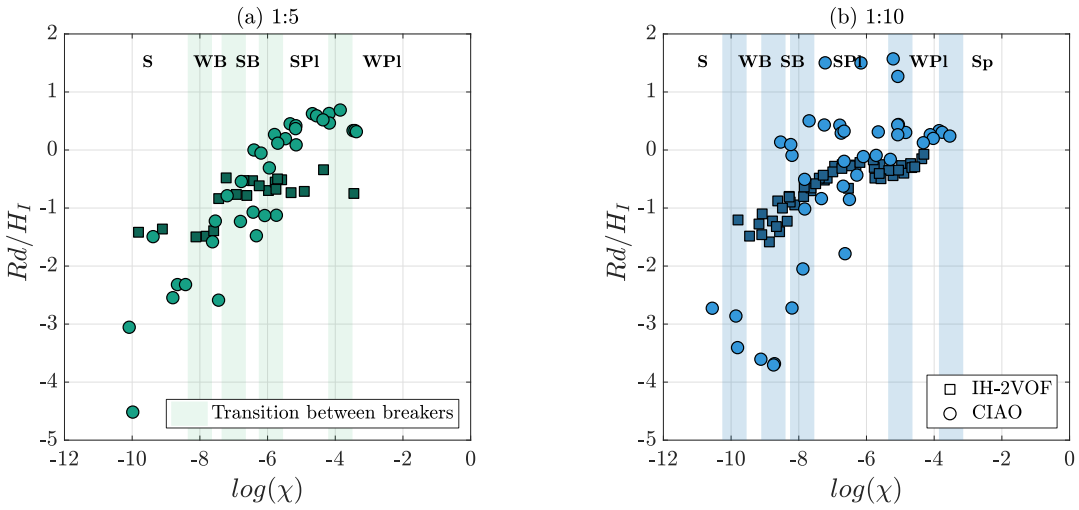


FIGURE 5.12: Average dimensionless run-down values obtained from the numerical IH-2VOF model and the CIAO wave flume, represented against the log-transformation product of $h/L$ and $H_I/L$. (a) for a 1:5 slope and (b) for a slope 1:10 slope. The vertical lines in (b) determine the domains of the different types of breaking according Chapter 3.

experiment (numerical or physical). For the 1:10 slope, the maximum appears in the interval $[4 < (Ru + |Rd|)/H_I < 8]$, while for the 1:5 slope, the maximum is within $[5 < (Ru + |Rd|)/H_I < 10]$.

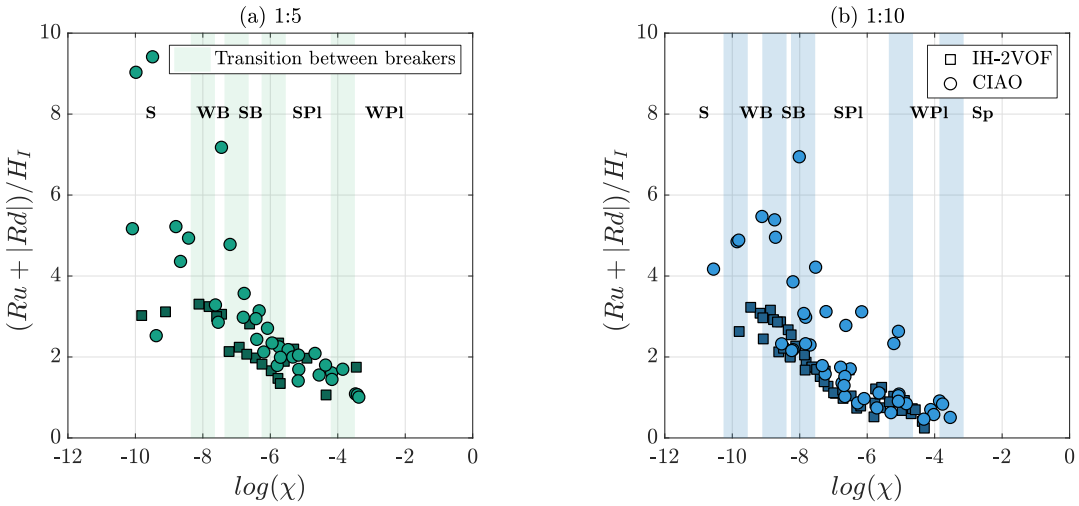


FIGURE 5.13: Non-dimensional total water excursion against $log(\chi)$, obtained from IH-2VOF and the CIAO wave flume for (a) 1:5 slope and (b) 1:10 slope. The vertical bands indicate the transition between breakers observed in the physical flume.

For both slopes, the differences between experiments become more evident as the regime becomes more reflective. For WPl and Sp breakers, the non-dimensional value of the excursion tends to $(Ru + |Rd|)/H_I \approx 1$ for the 1:5 slope and to $(Ru + |Rd|)/H_I \approx 0.5$ for the 1:10 slope. The variability found in the run-up and run-down results appears too in the total excursion, however, the maximum interval of total excursion is found in the surging breakers and not in the WB-SB.

As it happened for the run-up and the run-down, two trends are visible for both

the 1:5 and 1:10 slope, one produced by the rightmost data within the experimental space and the other by the leftmost data. The leftmost data produce the higher values of run-up and the minimum values of run-down.

Figure 5.14 represent the total water excursion in the slope versus the natural logarithm of the bulk dissipation coefficient, $B_S$ (Equation 5.8). For both slopes and the CIAO data, a linear trend of points with higher run-up or overtopping height is visible. That is, there is a linear relationship between the maximum water excursion and the total dissipation coefficient.

$$(D^*)_{CV} = B_S \frac{\rho}{g} C^5 \tag{5.8}$$

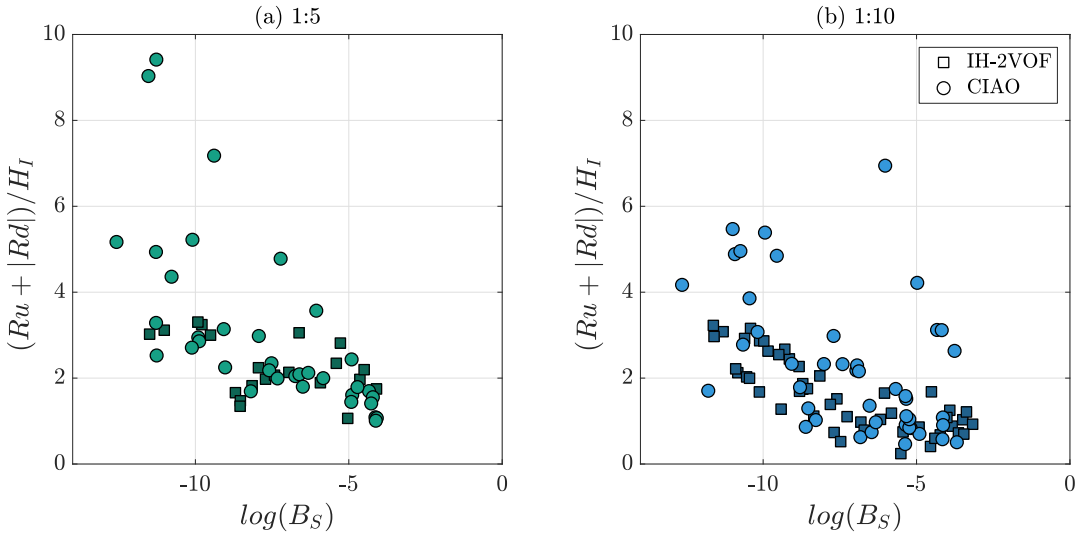


FIGURE 5.14: Non-dimensional total water excursion plotted against the bulk dissipation coefficient ($B_S$), obtained from IH-2VOF and the CIAO wave flume for (a) 1:5 slope and (b) 1:10 slope.

On the other hand, the remaining points, both physical and numerical, produce higher water excursion for the lower the dissipation coefficient, $log(B_s) \approx -13$ and $(Ru + |Rd|)/H_I \approx 5$. Focusing on the 1:5 slope, the water excursion decreases until it reaches its minimum value, $(Ru + |Rd|)/H_I \approx 1$, at approximately $log(B_S) \approx -4$. Likewise, in the 1:10 slope, the water excursion decreases as $B_S$ increases until it reaches a value of $(Ru + |Rd|)/H_I \approx 0.5$ at $log(B_S) \approx -3.5$.

Therefore, it is proved that not only the run-up is an indicator of the hydrodynamic regime on the interaction between the incident wave and the structure, but also the total water excursion is capable of describing whether the reflection or dissipation governs the problem.

### 5.5.3 Mean water level and type of breaking

Figures 5.15 (a) and (b) show the mean water level ($\overline{\eta}$) and Figure 5.15 (c) and (d), the non-dimensional mean water level ($\overline{\eta}/H_I$) obtained with the numerical model for two slopes: 1:5 and 1:10, as a function of $log(\chi)$. In addition, the vertical lines in (c) and (d) (constant value of $log(\chi)$) indicate the transit between the type of wave breakers observed in the numerical test and verified in the flume for a 1:10 slope,

and expected in the 1:5 slope. Vertical dotted lines in (c) and (d) determine the limit between the dissipative and reflective domain processes.

The mean water level is always positive, practically zero in the reflective domain and growing as $log(\chi)$ increases. It should be noted that this dependence is not monotonic. The mean water level value changes abruptly where the transits of the type of wave breaker occur.

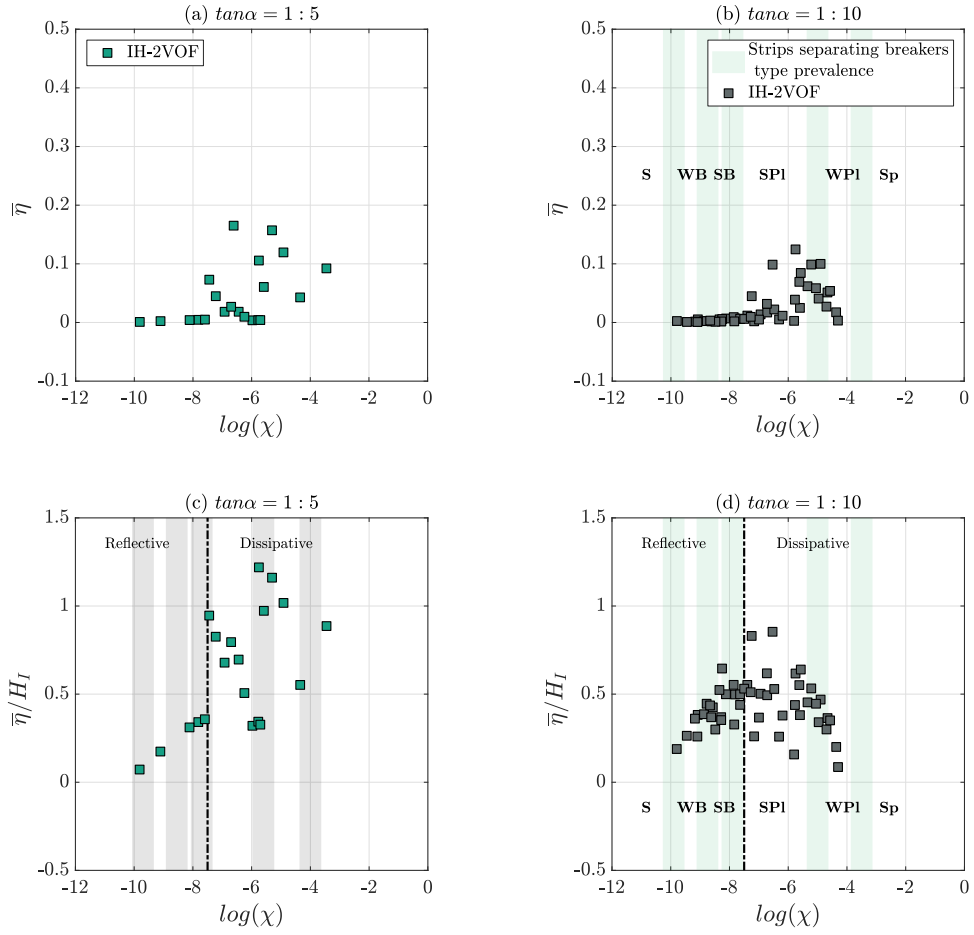


FIGURE 5.15: Mean water level and dimensionless mean water level for the numerical data plotted against $log(\chi)$. Numerical data are from IH-2VOF. Green lines in (d) determine the domains of the different types of breaking according to Chapter 3 (valid only for a 1:10 slope). Grey lines in (c) are the expected transition between breakers in a 1:5 slope. Vertical doted lines in (c) and (d) determine the limit between the dissipative and reflective domain processes.

### 5.5.4 Sigmoid function

Although we have seen in the previous sections that different run-up or run-down results can be obtained for the same type of breaking (constant $\chi$ value), or that the same $Ru/H$ value is obtained for different $\chi$ values, for engineering applications, it is very convenient to have formulas to quantify the flow characteristics of an impermeable and non-overtoppable slope. A spline function or a hyperbolic tangent function can be used to fit the experimental data. However, the sigmoid function (Churchill and Usagi, 1972) has been successfully used to describe various physical transport phenomena in fluid mechanics, heat transfer, and chemical engineering

(Sivanesapillai et al., 2014; Vílchez et al., 2016b). Since the flow characteristics of a slope are strongly dependent on wave energy transformation (bulk wave energy dissipation and reflection), it seems appropriate to apply the sigmoid function (Equation 5.9) to fit the experimental data.

$$Z(\chi) = (Z_1 - Z_0)\frac{1}{\left[1 + \left(\frac{\chi}{a_\chi}\right)^{\gamma_\chi}\right]}; \quad \chi > 0 \tag{5.9}$$

where $Z(\chi) = (Ru/H_I, Rd/H_I, \eta_m/H_I)$ is the physical entity, and $Z_0$ and $Z_1$ are the chosen limit values of $Z(\chi)$ for fitting the curves for small (reflective domain) and large values (dissipative domain) of the independent dimensionless variable $\chi$. The function describes a smooth transition between the limit values with a blending coefficient, $\gamma_\chi$, and a parameter of the process inherent to the sigmoid shape, $a_\chi$. Note that $\gamma_\chi$ determines the velocity of change of the flow characteristics as the independent variable changes. For $\chi = a_\chi$, the sigmoid has an inflection point, identifying the change of the dominant process in the wave energy transformation: reflective or dissipative.

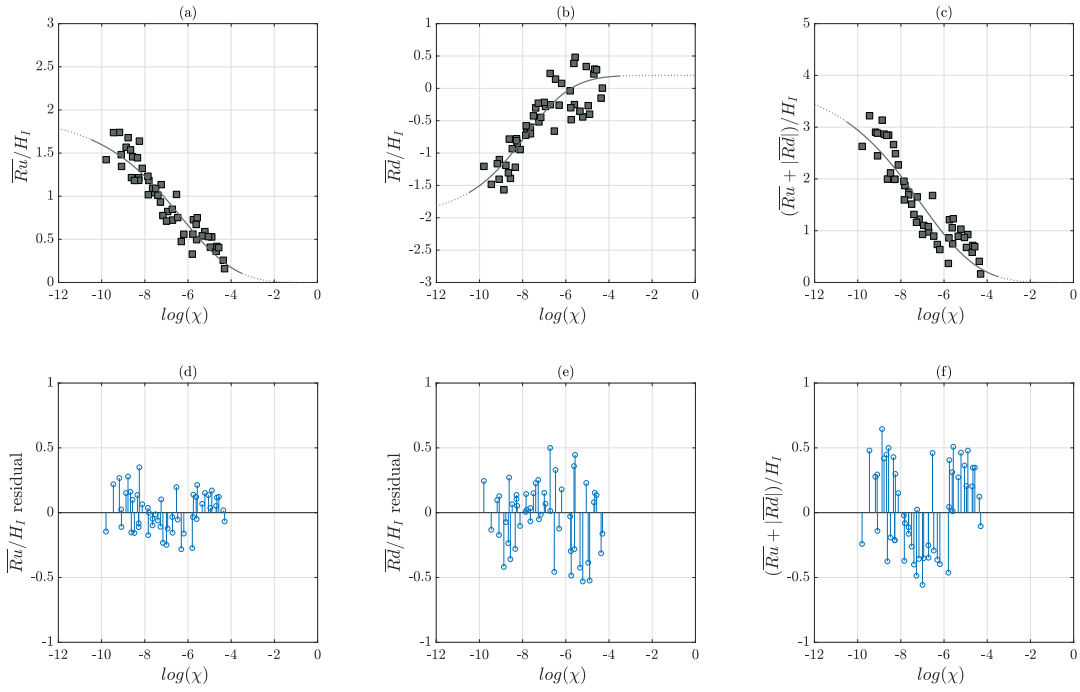


FIGURE 5.16: Sigmoid functions fitted to the dimensionless (a) run-up values, (b) run-down values and (c) total water excursion dependence on $log(\chi)$. (d), (e) and (f) represent the corresponding residuals errors of those fits. Data for slope 1:10

Figures 5.16(a), (b) and (c) represent the fit of a sigmoid curve to the experimental values of run-up, run-down and total water excursion for the 1:10 impermeable slope against $log(\chi)$ as well as their residual values. The experimental data alignment is satisfactory, and the distribution of the residual values indicates that the deviation of the $Ru/H_I$, $Rd/H_I$, $(Ru + |Rd|)/H_I$ values is reasonably small. It is possible that fitting the sigmoid functions depending on the position of the data inside the experimental space, as done in Figures 5.5 and 5.6, would give even smaller residual values.

Figure 5.17 shows the fit of a sigmoid curve to the experimental run-up, run-down and total water excursion values for the 1:10 impermeable slope against $Ir$ as well as the residual values. The distribution of the residual values indicates that the deviation of the $Ru/H_I$, $Rd/H_I$, $(Ru+|Rd|)/H_I$ values is larger with $Ir$ than with $log(\chi)$.

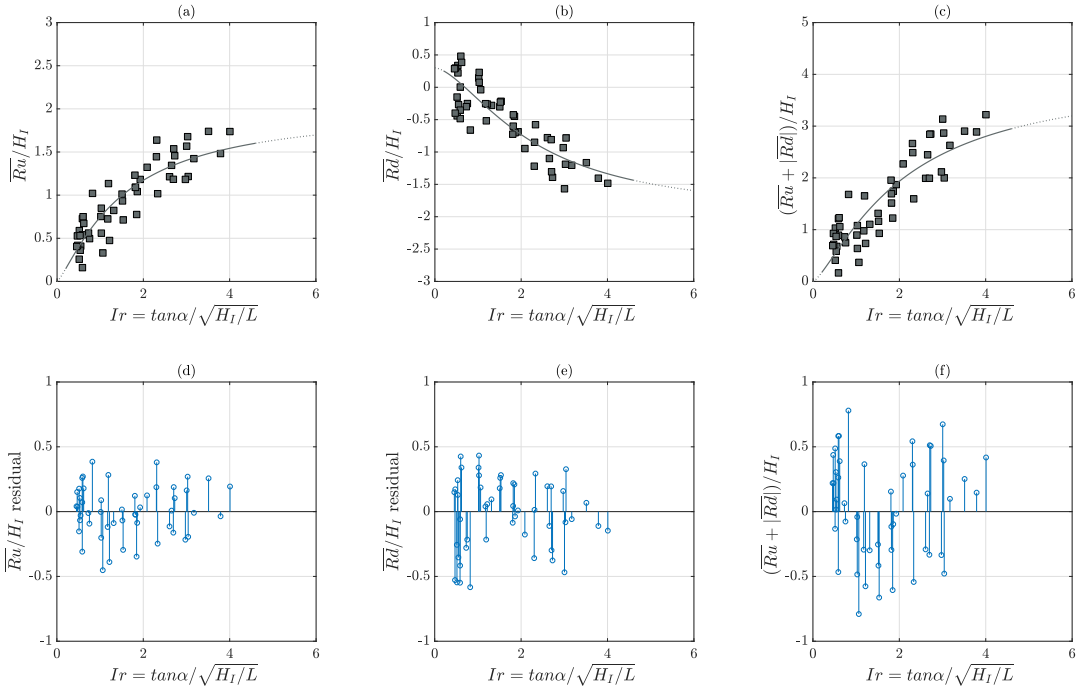


FIGURE 5.17: Sigmoid functions fitted to the dimensionless (a) run-up values, (b) run-down values and (c) total water excursion dependence on the Iribarren number ($Ir$). (d), (e) and (f) represent the corresponding residuals errors of those fits. Data for slope 1:10.

Table 5.6 shows the parameters of the sigmoid functions fitted to the impermeable experimental results $(Ru/H_I, Rd/H_I)$ and slope angle against $log(\chi)$. These parameters show that the sigmoid shape, $a_\chi$, is specific for each slope angle tested, including the chosen values of $Z_0$, $Z_1$.

Figure 5.18(a) shows the bulk dissipation versus $log(\chi)$ and Figure 5.18(b) the total water excursion on the slope, $(Ru+|Rd|)/H_I$ versus $log(\chi)$, for the two slopes analyzed with the numerical model. Since the transmitted energy flow is zero, the complementary curve of the dissipation, $1-D^*$, quantifies the relationship between the total water excursion and $K_R^2$.

It is important to note that these relationships can be explicitly obtained by solving the system of equations of the two sigmoids. In summary, knowing the relative $(Ru+|Rd|)$ and the values of the incident train ($H_I$, $T$ at the slope toe with depth $h$), the reflected energy flow and the bulk dissipation caused by the interaction of the train with the slope are predetermined. The inverse, knowing the distribution of $K_R^2$ or $D^*$ with $\chi = (h/L)(H_I/L)$ determines the total water excursion. However, to separate the run-up from the run-down, it is necessary to have records for one of them. This result converges with and supports the proposal of Almar et al. (2019) to use run-up asymmetry as a predictor of reflection on dissipative, intermediate and reflective beaches, in addition to recognizing the importance of wave reflection in beach morphodynamics (Baquerizo et al., 1998).

TABLE 5.6: Fit parameters for the sigmoid function fitted to the relative run-up, run-down and total water excursion values against $log(\chi)$ and $Ir$ in Figures 5.16 and 5.17.

| | **log($\chi$)** | | |
|---|---|---|---|
| | $Ru/H_I$ | $Rd/H_I$ | $(Ru+\|Rd\|)/H_I$ |
| $\Upsilon_0$ | 0 | 0.2 | 0 |
| $\Upsilon_1$ | 2 | -2 | 4 |
| $a_x$ | -7.13 | -8.25 | -7.90 |
| $\gamma_x$ | -4.07 | -6.39 | -4.33 |
| | **Ir** | | |
| | $Ru/H_I$ | $Rd/H_I$ | $(Ru+\|Rd\|)/H_I$ |
| $\Upsilon_0$ | 0 | 0.2 | 0 |
| $\Upsilon_1$ | 2 | -2 | 4 |
| $a_x$ | 1.51 | 2.41 | 2.10 |
| $\gamma_x$ | 1.25 | 1.86 | 1.32 |

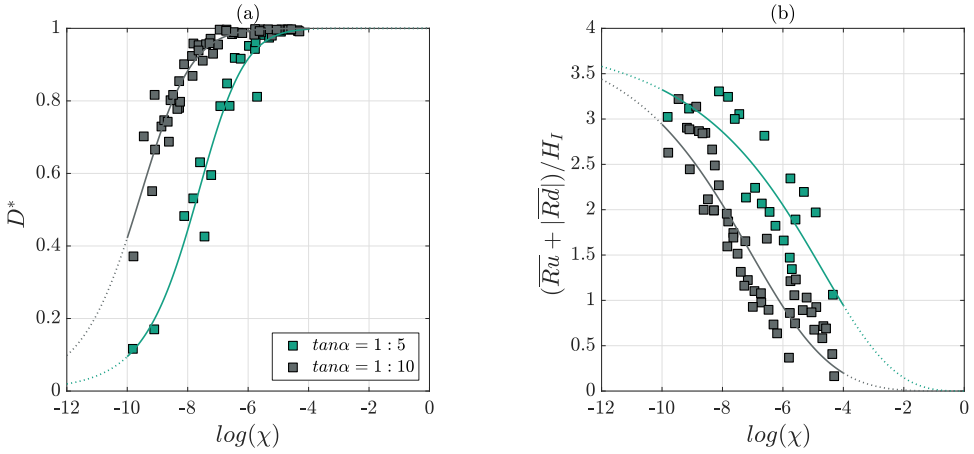


FIGURE 5.18: Sigmoid functions fitted to the dimensionless (a) the dissipation coefficient and (b) to the total water excursion for slopes 1:5 and 1:10, versus the logarithmic transformation of $\chi$.

TABLE 5.7: Fit parameters for the sigmoid function fitted to the bulk dissipation coefficient and total water excursion values against $log(\chi)$ in Figure 5.18.

| | **D** | | **$(Ru+\|Rd\|)/H_I$** | |
|---|---|---|---|---|
| | 1:5 | 1:10 | 1:5 | 1:10 |
| $\Upsilon_0$ | 1 | 1 | 0 | 0 |
| $\Upsilon_1$ | 0 | 0 | 4 | 4 |
| $a_x$ | -7.81 | -9.07 | -5.90 | -7.90 |
| $\gamma_x$ | -9.09 | -10.45 | -3.01 | -4.33 |

## 5.6 Conclusions

The objectives of this chapter are threefold: (a) to quantify the flow characteristics on plane-impermeable non-overtoppable slopes with different inclinations under regular and irregular waves, (b) to correlate with the type of wave breaking types and (c) to relate the total water excursion in the slope with the bulk dissipation coefficient $(D^*)$ or its complementary value, the reflection coefficient $(K_R^2)$. To accomplish these objectives three sources of experimental data are considered:

(a) physical tests done on a smooth impermeable slope at the CIAO wave flume, (b) numerical experiments on undefined impermeable rigid slopes with the numerical model (IH-2VOF) and (c) published physical experiments on non-overtoppable plane impermeable slopes in 2D wave flumes by different authors. From this study the following conclusions can be drawn:

1. Based on dimensional analysis, an alternate slope similarity parameter $\chi$, is proposed for the analysis of flow characteristics on impermeable slopes under regular and irregular waves. Plotting $[Ru/H_I, Rd/H_I]$ against $\chi$, gives a good display of the experimental data, and help to define the wave energy transformation domains on the slope. The largest deviation of the experimental data use to occur at the transitions between the following types of wave breaker: weak bore - strong bore - strong plunging. These transitions depend on the slope angle.

2. The same breaker type can produce different run-up values depending on the relative water height of the incident wave $\gamma = H/h$. The generation of regular and irregular wave trains in a horizontal bottom channel limits the $H/h$ values and is a severe constraint for the development of formulas for slope flow characteristics. Thus, Ahrens et al. (1993) concerns, *"that laboratory-based wave run-up formulas do not perform for what may be the design run-up condition, even for regular wave trains"*, are verified.

3. A sigmoid function of the variable $(h/L)(H_I/L)$ fits reasonable well with the experimental results $[Ru/H_I, Rd/H_I]$. A poor fit is obtained when the Iribarren number is taken as the independent variable. These conclusions are confirmed by the representation of the residual error between the experimental data and the fitted curve. The total water excursion on the slope, $(Ru + |Rd|)/H_I$, can be predicted by knowing the bulk dissipation (or with its complementary value, $K_R^2$), and vice versa.

4. The blending parameter of the sigmoid function is the value of the parameter $\chi = h/L \cdot H_I/L$ where the inflection point is located. This parameter can be used to separate the reflective predominance and the dissipative predominance domains (Figure 5.15). It is shown that most of the revised flume experimental data do not encompass the plausible experimental space but are obtained under a constant relationship of $(h/L)$ and $(H_I/L)$ or constant Iribarren number.

# 6 Flow characteristics on armored impermeable slopes

**Comment**

This section presents some of the results published on:

**Moragues, M.V.**, Clavero, M., Díaz-Carrasco, P. and Losada, M.A. (2020) "Bulk dissipation and flow characteristics in cube armored breakwaters". In: *Proceedings of the 36th International Conference on Coastal Engineering (vICCE20)*.
DOI: https://doi.org/10.9753/icce.v36v.structures.40

*"Our knowledge is a little island in a great ocean of nonknowledge."*

Isaac Bashevis Singer

*Based on dimensional analysis, the alternate slope similarity parameter has been used to analyze the flow characteristics on an armored non-overtopabble impermeable slope. As seen in Chapter 5, this parameter is capable of defining the run-up and run-down for a given slope angle. In this Chapter, this parameter is combined with the relative diameter of the armor pieces to analyze the two main sources of dissipation for this type of structure: the breaking waves and the turbulence generated in the pores between the pieces. Searching for constant values of $\chi$ allows us to focus on a fixed breaker type and to analyze the influence of the armor and viceversa. Additionally, a sigmoid function has been fitted to the run-up data in ranges of $D_a/H$. In this Chapter the goals to be achieved are (a) to be able of predicting the run-up as a function of $\chi$ and $D_a/H$ and (b) to analyze the bulk dissipation coefficient $(D^*)$ or its complementary value, the reflection coefficient $(K_R^2)$, in this type of breakwater.*

## 6.1 Introduction

This chapter continues the research begun in the previous Chapter, where the parameters affecting run-up and run-down in a smooth impermeable slope were analyzed. It has been shown how the slope angle ($\alpha$), the relative water depth ($h/L$) and the wave steepness ($H_I/L$) are the main variables affecting the run-up and run-down.

However, if the rubble mound breakwater is formed by a rough permeable armor and an impermeable core, the permeability of the material would affect the maximum level the water reaches. This means that the flow characteristics, in addition to being affected by the dissipation caused by wave breaking and by the boundary layer of the impermeable material, will be influenced by the roughness of the permeable material that forms the main armor.

The turbulence created in the pores between the armor units increases the energy dissipation. These pores depend on the material size and its colocation, but it can be concluded that the bigger the space between pieces, the bigger the dissipation and therefore, less the run-up.

One of the first experiments for measuring run-up on armored permeable slopes were done by Hudson (1959) and Hunt (1959) who added a reduction factor to include the effect of the roughness into the prediction of run-up. Other publications such as The Shore Protection Manual (1984) or Ahrens (1981) also recommended the use of reduction factors to account for the influence of both the hydraulic conductivity and the roughness of the structure.

However, several studies have shown that the behavior of waves on permeable slopes is very different from those on impermeable slopes (Losada and Giménez-Curto, 1981; Allsop et al., 1985; Van Der Meer, 1992), implying that the calculation of flow characteristics in permeable structures must be performed in a different way.

Firstly, the parameters of the permeable breakwater must be identified, as shown in Figure 6.1. The influence of the main armor can be described by the nominal diameter of the armor pieces ($D_{n50,a}$), their density ($\rho_s$) and the thickness of the armor ($e$). Notice that the thickness of the main armor layer, $e$, can be determined based on the nominal size of unit, $D_{n50,a}$, and on the shape factor of unit, $K_p$ and the number of layers, $n_c$, as shown in Equation 6.1 (Gómez-Martín and Medina, 2014).

$$e = n_c K_p D_{n50,a} \tag{6.1}$$

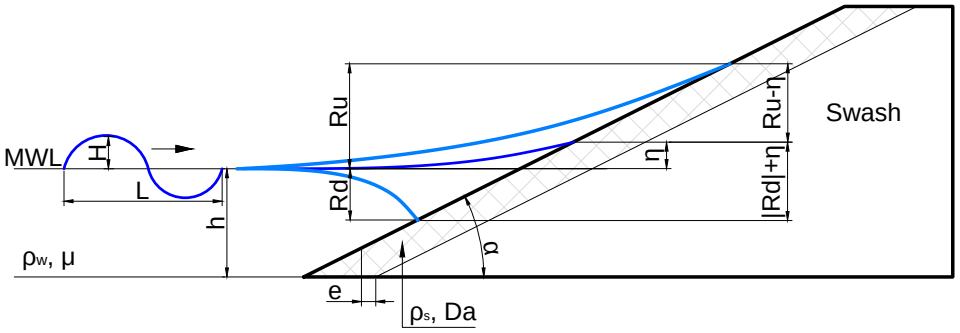


FIGURE 6.1: Scheme of the geometrical parameters affecting run-up and run-down in an armored non-overtoppable breakwater.

Next, an analysis of how these variables affect the flow run-up and run-down must be done. For this purpose, as in the previous Chapter, dimensional analysis has been used (Chapter 2). The following sections present the influence of the friction coefficient of the porous medium, the methodology and datasets used, the results obtained for run-up, and the conclusions that can be drawn from them.

## 6.2 Dissipation in the porous medium

The resistance forces generated during the propagation of the fluid through the porous medium are the cause of the dissipation generated in the main armor. The Forchheimer equation (Equation 6.2) can represent these forces adequately:

$$F_{NL} = au + b|u|u + c_A \frac{\partial u}{\partial t} \tag{6.2}$$

where u is the seepage velocity through the voids and $a$, $b$, and $c_A$ are local coefficients. Dalrymple et al. (1991), Van Gent (1995), Burcharth and Andersen (1995) and Requejo et al. (2002), among others, analyzed in detail the coefficients $a$, $b$ and $c_A$. The expression includes a linear term accounting for the laminar flow; a non-linear term, representing the turbulent flow; and an inertial term considering the added mass effect (Polubarinova-Kochina, 1962).

The governing equations for the interaction of a gravity wave train with a single homogeneous porous structure can be solved analytically when the resistance forces are linearized, introducing a friction coefficient, $f_c$. Pérez-Romero et al. (2009) proposed a characteristic friction diagram considering the energy balance between numerical and experimental tests to analyze the wave interaction with porous structures. Vílchez et al. (2016a) following the same methodology, obtained a characteristics friction diagram for different breakwater types.

Through dimensional analysis they proved that the friction coefficient depends on:

$$f_c = f\left(\frac{B}{L}, D_a k, \frac{D_a}{H}\right) \tag{6.3}$$

where $B$ is the relative width of the core of the structure, $D_a$ is the stone diameter, $L$ is the wavelength, $k$ is the wave number and $H$ is the wave height. As in this case the core is impermeable, the non-dimensional parameters in which the $f_c$ depends on are $D_a k$ and $D_a/H$. Figure 6.2 presents the characteristic friction diagram based on Vílchez et al. (2016a), the best fitting curve and the upper and lower 95% confidence bounds are also given.

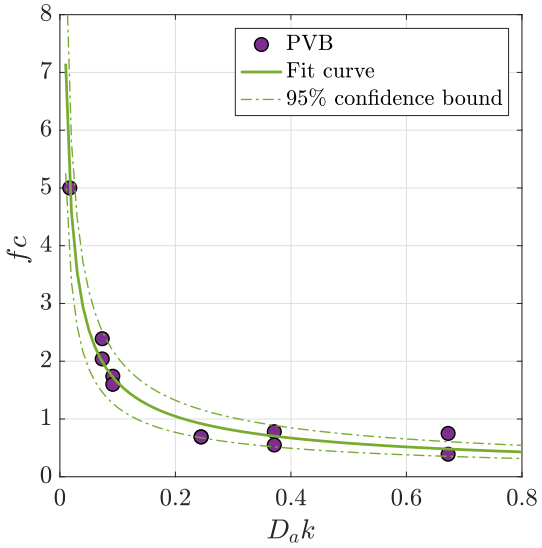


FIGURE 6.2: Characteristic friction diagram based on Vílchez et al. (2016a), with the best fit and the 95% confidence bounds for a porous vertical breakwater.

However, with this representation the influence of $D_a/H$ in the friction coefficient cannot be seen. Therefore, a new way of representing these values has been proposed to take into account the influence of both dimensionless parameters. Figure 6.3 presents a new friction diagram with $log(D_a/H)$ plotted against $log(D_a/L)$. As tests were done keeping $L$ constant while increasing $H$, there are groups for both variables. The Figure shows how the value of $f_c$ decreases as $D_a/H$ and $D_a/L$ increases, being $f_c$ almost 0 for the maximum values ($D_a/H \approx 5.75$ and $D_a/L \approx 0.10$); and its maximum value, $f_c = 5$, is reached for the minimum values ($D_a/H \approx 0.259$ and $D_a/L \approx 0.002$).

It can be concluded that the friction coefficient depends on both, $D_a/H$ and $D_a/L$. As resulted from dimensional analysis, the water depth and the wave height are non-dimensionalized with the wave length, from now on, the influence of the relative diameter has been analyzed through $D_a/H$ instead of $D_a k$.

## 6.3 Methodology and data from other authors

### 6.3.1 Data from other authors

This study is based on the following experimental data for run-up obtained from other published papers: Van Der Meer (1988) and Van Der Meer and Stam (1992),

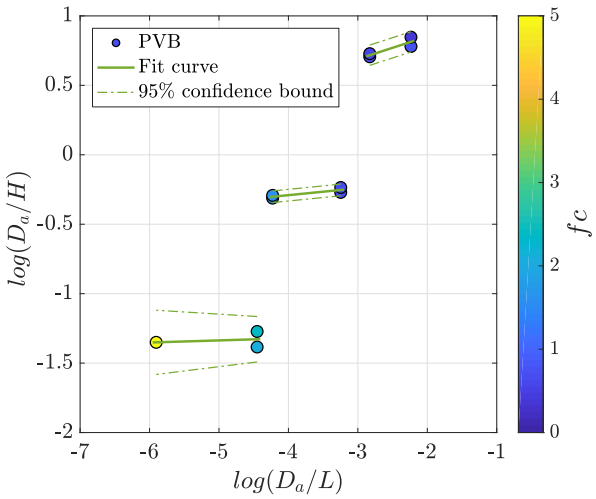


FIGURE 6.3: New friction diagram, with the best fit and the 95% confidence bounds for a porous vertical breakwater.

Broekhoven (2011) and Kreyenschulte et al. (2020).

### Van Der Meer (1988) and Van Der Meer and Stam (1992)

Van Der Meer (1988) and Van Der Meer and Stam (1992) conducted a series of tests on permeable and impermeable structures. Test were done at the wave flume of the Delft University of Technology with dimensions of 50 $m$ long, 1.2 $m$ deep and 1.0 $m$ wide. Irregular waves were generated following a Pierson-Moskowitz spectrum. They used a 2 wave gauge array to compensate the reflection from the paddle generator. Their test series consisted on series with the same wave period an increasing the wave height. Then the wave period was increased and the process repeated. Water depth at the toe of the structure was kept constant at $0.8m$. Tests conditions are summarized in the Table 6.1. The provided value for the run-up measurements is the 2% exceedance run-up.

TABLE 6.1: Summarized test conditions of the tests carried out by Van Der Meer (1988) and Van Der Meer and Stam (1992). Variables are described in the Nomenclature.

| Parameter | Armored impermeable |
|---|---|
| Number of tests | 101 |
| $\boldsymbol{tan(\alpha)}$ | 1:2, 1:3, 1:4 |
| $\boldsymbol{H_{m0}}(m)$ | 0.045 - 0.198 |
| $\boldsymbol{T_p}(s)$ | 1.37 - 3.85 |
| $\boldsymbol{H_{m0}/L}$ | 0.006 - 0.062 |
| $\boldsymbol{Ir}$ | 1.05 - 8.32 |
| $\boldsymbol{h}(m)$ | 0.8 |
| $\boldsymbol{Ru_{2\%}}(m)$ | 0.109 - 0.287 |
| $\boldsymbol{D_{n50,a}}(m)$ | 0.036 |
| $\boldsymbol{e}(m)$ | 0.08 |
| $\boldsymbol{\rho_a}(Kg/m^3)$ | 2620 |

**Broekhoven (2011)**

Broekhoven (2011) conducted a series of experimental tests to study the influence of the structure permeability on the run-up (Section 5.2.3). In this Chapter, the data corresponding to an armored impermeable slope slope is used (Table 6.2). The experimental output is the mean run-up of the record.

TABLE 6.2: Summarized test conditions of the tests carried out by Broekhoven (2011).

| Parameter | Armored impermeable |
|---|---|
| Number of tests | 166 |
| $\boldsymbol{tan(\alpha)}$ | 1:1.5, 1:2 |
| $\boldsymbol{H}(m)$ | 0.054 - 0.149 |
| $\boldsymbol{T}(s)$ | 0.85 - 3.59 |
| $\boldsymbol{H/L}$ | 0.008 - 0.097 |
| $\boldsymbol{Ir}$ | 1.69 - 11.84 |
| $\boldsymbol{h}(m)$ | 0.5 |
| $\overline{\boldsymbol{Ru}}(m)$ | 0.053 - 0.402 |
| $\boldsymbol{D_{n50,a}}(m)$ | 0.067 , 0.09 |
| $\boldsymbol{e}(m)$ | 2*Da |
| $\boldsymbol{\rho_a}(kg/m^3)$ | 2610 |
| $\boldsymbol{n_a}$ | 0.41. 0.40 |

**Kreyenschulte et al. (2020)**

Kreyenschulte et al. (2020) conducted a series of full scale experimental tests at the GWK of the Coastal Research Center (FZK), which has a length of 304 $m$, 7 $m$ depth and 5 $m$ width. The flume has a piston-type paddle. They tested four different configurations of mortar-grouted riprap with a 1:3 fixed slope and a constant water depth of $h = 4m$. The difference between configurations was the thickness of the armor and its porosity, changed by applying more volume of mortar. They produced irregular waves following a Jonswap spectrum with a minimum of 1000 waves per test. With the method of Mansard and Funke (1980), they separated the incident and reflected wave height. Run-up was measured with a 2D LIDAR scanner, providing the run-up 2%. Tests conditions are summarized in Table 6.3.

### 6.3.2 Hydrodynamic flow regimes of the analyzed data

As done in Section 5.2.4, before analyzing all the data together, an analysis of the hydrodynamic regimes has been made to see how each test has been done and if, in spite of studying them together in this work, there are hydrodynamic differences between them. Figure 6.4 represent de aforementioned described data in the Le Méhauté abacus (Le Méhauté, 1976). Linear wave theory (Airy, 1845) can be applied in the bottom right area of the abacus, where the waves are small enough, and its wavelength is small compared to the water depth. This means that the Stoke's expansion (Stokes, 1847) does not need a second order term. If the amplitude of the wave increases until it reaches values of $H/(gT^2) = 0.001$, linear theory cannot be applied anymore and the Stokes theory needs its second order term. If the wave

TABLE 6.3: Summarized test conditions of the tests carried out by Kreyenschulte et al. (2020). $n_a$ is the estimated porosity (after grouting).

| Parameter | Partially Grouted | Fully Grouted |
|---|---|---|
| Number of tests | 16, 16 | 16, 16 |
| $\boldsymbol{tan(\alpha)}$ | 1:3 | 1:3 |
| $\boldsymbol{H_{m0}}(m)$ | 0.375 - 0.853 | 0.390 - 0.941 |
| $\boldsymbol{T_p}(s)$ | 3.01 - 12.18 | 3.43 - 12.18 |
| $\boldsymbol{H_{m0}/L}$ | 0.003 - 0.027 | 0.003 - 0.039 |
| $\boldsymbol{Ir}$ | 1.56 - 3.56 | 1.42 - 3.45 |
| $\boldsymbol{h}(m)$ | 4 | 4 |
| $\boldsymbol{Ru_{2\%}}(m)$ | 0.80 - 2.21 | 0.99 - 2.32 |
| $\boldsymbol{D_{n50,a}}(m)$ | 0.21 | 0.21 |
| $\boldsymbol{e}(m)$ | 0.4, 0.6 | 0.4 , 0.6 |
| $\boldsymbol{n_a}$ | 0.32, 0.25 | 0.16, 0 |

amplitude continues increasing, higher order terms should be added to the Stokes theory to obtain more accurate results.

This is what happens to Broekhoven's, Van der Meer's and Kreyenschulte's data. It can be seen how it holds in the same regimes as for a smooth slope, mostly in Stokes's 2$nd$ and 3$^{rd}$ order. This means that the higher order Stokes wave can be separated into two or more coupled sine waves. This mechanism is followed by more complicated representations resulting from the superposition of basic sine waves to obtain more complex representations that better fit the phenomena occurring in nature.

On the other hand, Van der Meer's and Kreyenschulte's data have the same hydraulic regime between them. This means that although both datasets are produced at different scales, a direct comparison can be made between them.

### 6.3.3 Dimensional analysis

Based on Chapter 2, if the slope of the structure is non-overtoppable, impermeable and has a permeable armor, the functional to analyze its behavior is as shown in Equation 6.4.

$$\frac{X}{H_I} = \left(\frac{Ru}{H_I}, \frac{Rd}{H_I}, \frac{\eta_m}{H_I}\right) = f_\alpha \left(\frac{H_I}{L}, \frac{h}{L}, \frac{D_{a,n50}}{H_I}, Re_p\right) \tag{6.4}$$

Being $Re_p$ the pore size based Reynolds number, which depends on the thickness and the porosity of the main armor (Equation 6.5).

$$Re_p = \frac{\pi e}{n_e T} \frac{H_I}{\nu_w \left(sinh \frac{2\pi h}{L}\right)} \tag{6.5}$$

In Figure 6.5 all sets of data for the aforementioned authors are presented in the experimental space $[log(H/L) - log(h/L)]$. The data is classified by slopes: Figure 6.5(a) represents the data for a 1:1.5 slope, (b) for a 1:2 slope, (c) for a 1:3 slope and (d) for a 1:4 slope. For each author, the legend specifies the type of data represented.

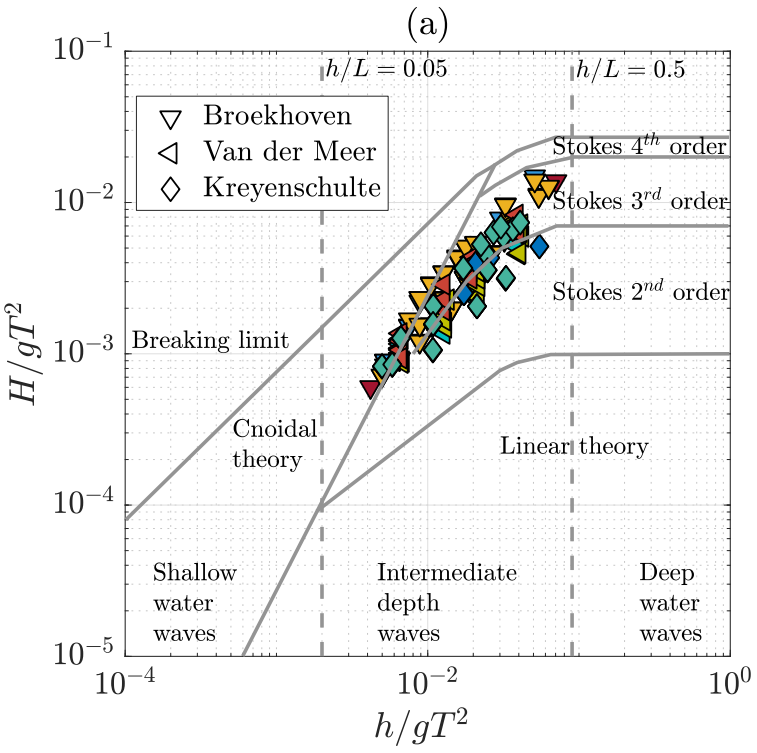


FIGURE 6.4: Analyzed data from the other authors represented together with the limits of validity for various wave theories (Le Méhauté, 1976). Symbols represent the data from each author and colors each slope angle and configuration.

However, the data for each author has a particular behavior. Broekhoven's data follows a linear relation between $log(h/L)$ and $log(H/L)$, as it did in the case of a smooth slope. Van der Meer's data is organized in groups of points with constant values of $h/L$ while varying the wave steepness. However, the changes in wave steepness values, for each relative water depth, are not pronounced enough for a trend change to be seen in the run-up data. Kreyenschulte et al. (2020)'s data, without having Van der Meer's trend of constant $h/L$ while increasing $H/L$, are in the same ranges of $[log(H/L)$ vs $log(h/L)]$. It should be noted that the four configurations were made in pairs, so the data from configurations 1 and 2 and those from configurations 3 and 4 should overlap as they have the same wave data.

## 6.4 Results

### 6.4.1 Run-up

In Figure 6.6, the non-dimensional run-up is plotted versus $log(\chi)$ as a function of the slope. In Figure 6.6(a) the data from Broekhoven for a 1:1.5 slope is shown as a function of the nominal diameter of the material (config. 1: $D_{n50,a} = 0.067m$ and config. 2: $D_{n50,a} = 0.09m$). The data appears to have a lot of dispersion around $log(\chi) \approx -6$ with $Ru/H = [0.75 - 1.55]$. Although difficult to predict, it is to be expected that, between $log(\chi) \approx -5$ and $log(\chi) \approx -7$, the transitions between strong plunging, strong bore and weak bore will occur, causing a lot of scatter in the data. Before analyzing the effect of the armor diameter, Broekhoven's results are in accordance with the results obtained for a smooth impermeable slope where for

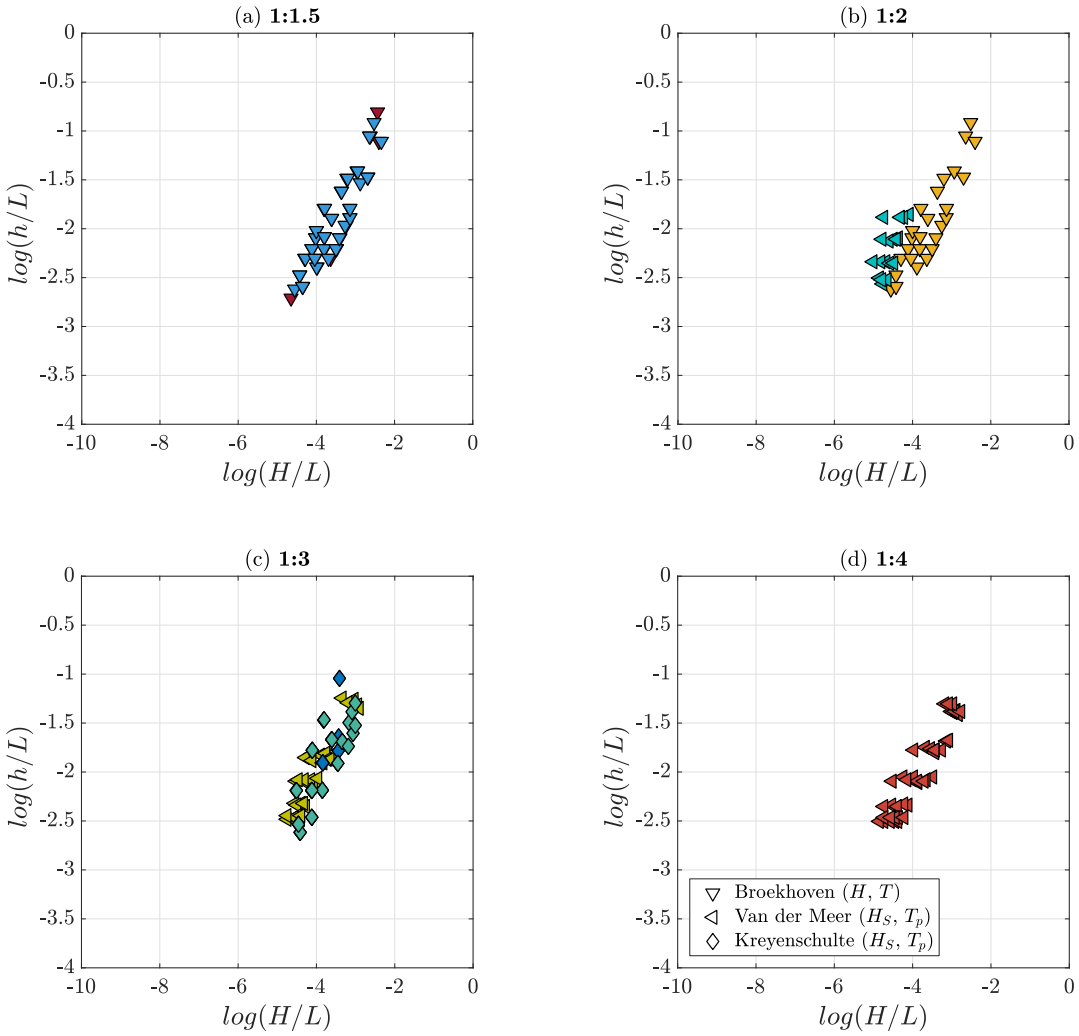


FIGURE 6.5: Experimental space $[log(H_I/L) - log(h/L)]$ classified by slopes (a) for a 1:1.5 slope, (b) for a 1:2 slope, (c) for a 1:3 slope and (d) for a 1:4 slope. Symbols represent the data for each author and colors are different for each slope angle and configurations.

the same $\chi$ value a range of $Ru/H$ values can be obtained. It would be necessary to check if the data shown are the maximum data that can be obtained, but looking at the position of the points in the experimental space, it would be expected that the data located further to the left (from $log(H/L) \approx [-7$ to $-4]$ and $log(h/L) \approx [-2.75$ to $-0.25]$ would produce higher dimensionless run-up values.

In Figure 6.6(b), the data from Broekhoven and Van der Meer for a 1:2 slope is presented. Even though both sets of data cover the same values of the alternate similarity parameter, $[-7.5 < log(\chi) < -5.8]$, the difference between the authors' $Ru/H$ values is almost double, being greater the values from Van der Meer. Van der Meer's points are closer to each other in the experimental space, producing similar values of run-up. Broekhoven's data appear to have the same behavior as for the 1:1.5 case, being more spread out in Figure 6.5(b), their data produce more variable results. Similar to the previous case, it is to be expected that, around these values, the changes between SP, SB and WB will occur. This Figure proves that the dissipation in the permeable armor should be analyze separately from the breaking waves, but both dissipation fonts must be taken into account.

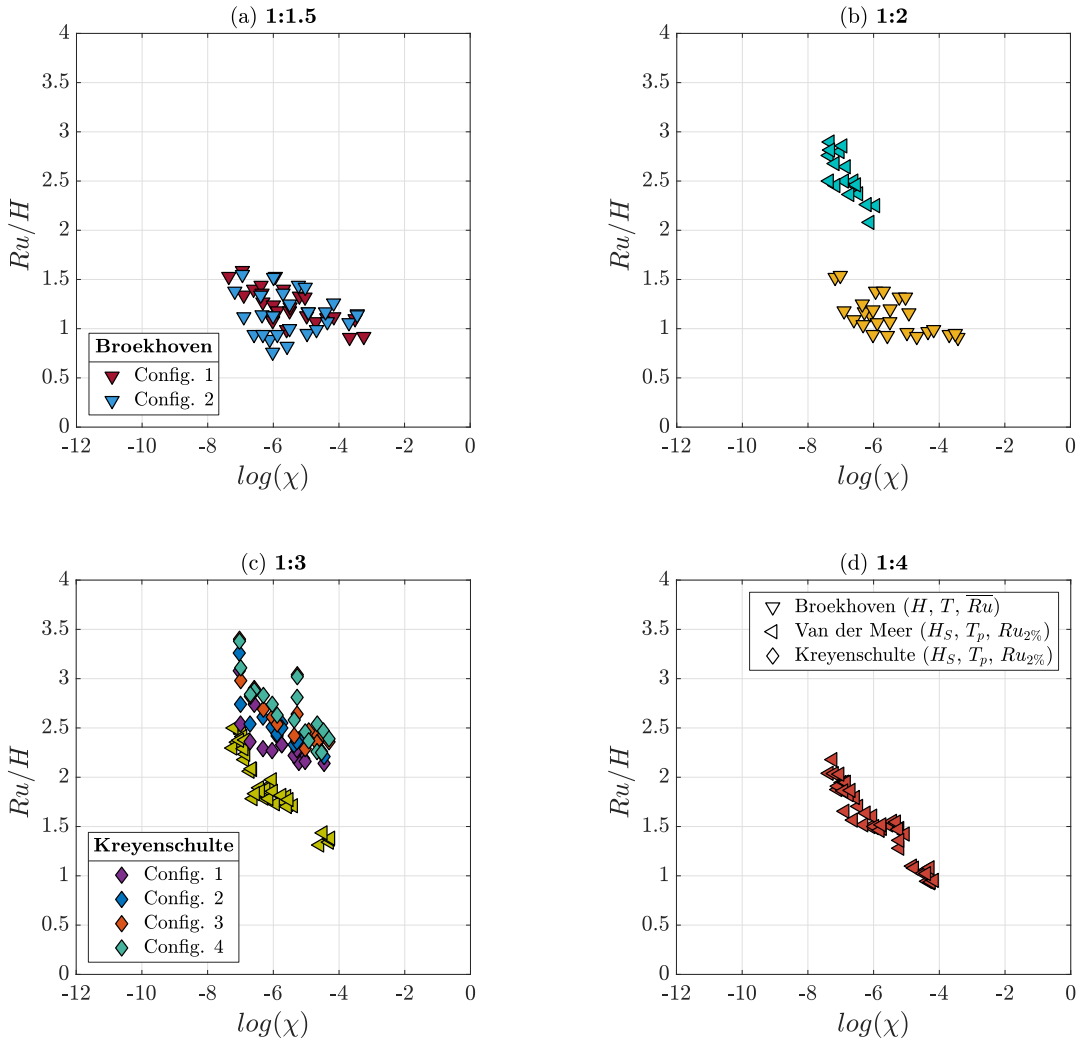


FIGURE 6.6: Non-dimensional run-up versus $log(\chi)$ classified by slopes (a) for a 1:1.5 slope, (b) for a 1:2 slope, (c) for a 1:3 slope and (d) for a 1:4 slope. Symbols represent the data for each author and colors are different for each slope angle and configurations.

Similar behavior appears in Figure 6.6(c) with the data from Van der Meer and Kreyenschulte for a 1:3 slope. The data from Kreyenschulte et al. (2020) is divided into four configurations with different porosity and armor thickness (config. 1: $e = 0.6$ and $n = 0.32$; config. 2: $e = 0.4$ and $n = 0.25$; config. 3: $e = 0.6$ and $n = 0.16$; and config. 4: $e = 0.4$ and $n = 0$). In this case the data from Kreyenschulte is greater than the data from Van der Meer, in both cases the maximum run-up ($Ru/H \approx 2.5$ for Van der Meer's data and $Ru/H \approx 3.4$ for Kreyenschulte's data) appears at a value of $log(\chi) = -7$. Also, both datasets appear to have the same behavior as a function of $\chi$: they appear grouped in 3 clusters, $[-7.5 < log(\chi) < -6.75]$, $[-6.75 < log(\chi) < -5.5]$ and $[-5.5 < log(\chi) < -4 - 0]$, probably caused by strong bore, strong plunging and weak plunging type breakers, respectively, and the jumps are due to their transitions. However, in neither cases does the variability seen in Broekhoven's data appear. As seen for the case of the smooth and impermeable slope, this is due to the narrow range of $h/L$ and $H/L$ values with which these authors have worked. Tests closer to the generation limits of each wave channel would be able to identify higher values of run-up.

Focusing on Kreyenschulte et al. (2020)'s data, configuration 4 produces the higher run-up values, while configuration 1 produces the lower values, meaning that the lower the porosity and the thickness of the armor layer, the higher values the water reaches, as it has been concluded in other studies (Van Der Meer, 1988; Ahrens and Titus, 1985; Van Der Meer and Stam, 1992; Broekhoven, 2011; Capel, 2015; Giridhar and Reddy, 2015; Kreyenschulte et al., 2020), among others.

In Figure 6.6(d) only Van der Meer's data for the 1:4 slope are shown. As the slope is gentler, the run-up values are lower than in the 1:3 slope, yet the behavior is the same, with little data scatter produced by the few values of $H/L$ tested. As for the 1:3 case, the data appears in three different groups: $[-7.5 < log(\chi) < -6.0]$, $[-6.0 < log(\chi) < -5.0]$ and $[-5.0 < log(\chi) < -4 - 0]$, also probably caused by the SB, SP and WP breakers and their transitions.

Figure 6.7 shows the experimental space for the 1:3 slope data from Van Der Meer (1988) and Kreyenschulte et al. (2020). Figure 6.7(a) presents all the points from the experimental space, while in (b) only the five lines with the fitted points are shown: fit 1 with $\chi = 0.0140$, fit 2 with $\chi = 0.0025$, fit 3 with $\chi = 0.0013$ and fits 4 and 5 covering the maximum values of $\chi$ with different combinations of $h/L$ and $H/L$.

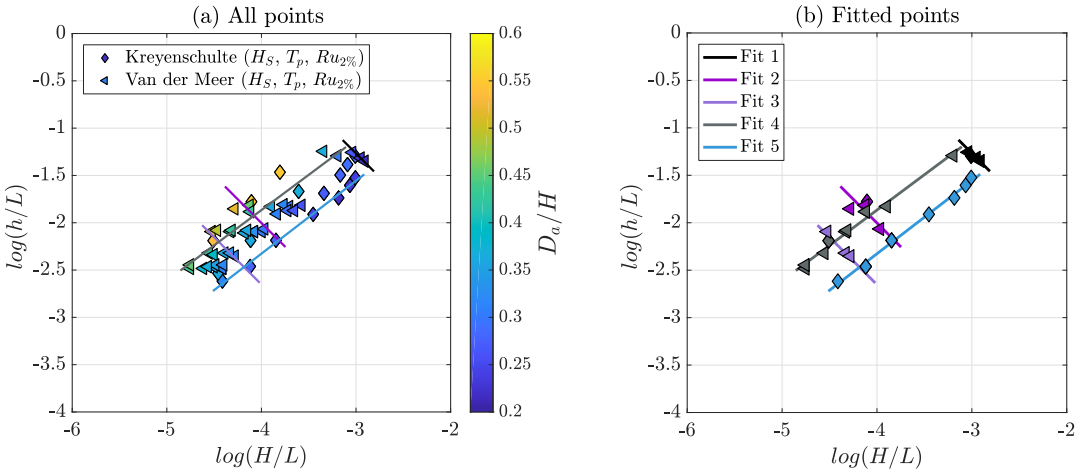


FIGURE 6.7: Experimental space $[log(H_I/L) - log(h/L)]$ for the 1:3 slopes of Van Der Meer (1988) and Kreyenschulte et al. (2020) (a) with all the data points and (b) for the fitted lines with constant values of $\chi$ and increasing values of $\chi$.

In general, comparing the four figures, it can be concluded that the steeper the slope, the higher the run-up values, and that the breaker types must be taken into account since their transitions show jumps in the dimensionless run-up values. To analyze this influence, from the datasets points with constant $\chi$ values (same type of breaking) and with linear $\chi$ changes (to observe the highest number of transitions) have been chosen.

The fitting points in Figure 6.7 are represented in Figure 6.9, showing the non-dimensional run-up versus $log(\chi)$. In this case Van der Meer's and Kreyenschulte's data are more differentiated from each other, being Kreyenschulte's non-dimensional run-up around 0.8 higher than Van der Meer's. Both authors have the same ranges of relative diameter of the armor, so these differences might be caused by the different scales both author work with: while Kreyenschulte et al. (2020) works with full-scale hydraulic models, Van der Meer's were done in small scale (not scaled to any specific structure), so scale effects can be expected.

Figure 6.8 presents the Reynolds number inside the porous armor for each dataset (Equation 6.5). Van der Meer's data has values between $[1.42x10^4 \leq Re_p \leq 3.50x10^4]$, while Kreyenschulte's results are between $[1.52x10^5 \leq Re_p \leq 3.39x10^6]$ (as the Reynolds value depends on the porosity, which remains in the denominator of the formula, in Kreyenschulte's configuration 4, the value of $Re_p$ is infinite since it divides by 0). Some authors concluded that the run-up was underestimated in normal small scale models (De Rouck et al., 2001; Burcharth and Lykke Andersen, 2009) so it is possible that the lower values of run-up from Van der Meer's data set are due to these scale effects.

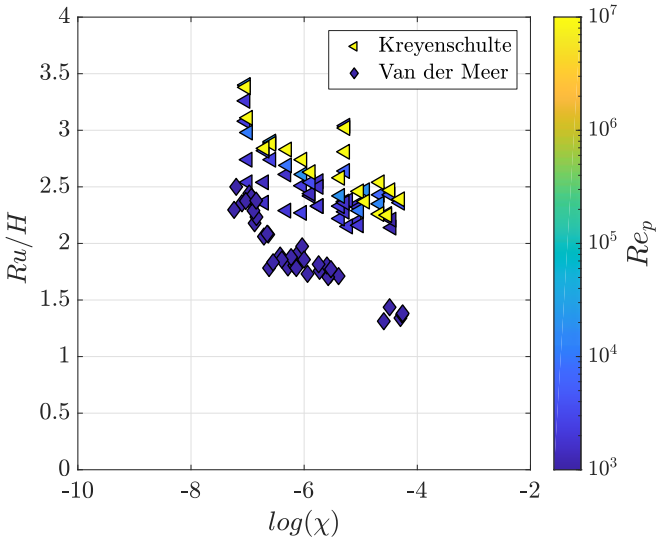


FIGURE 6.8: Non-dimensional run-up versus $log(\chi)$ from Van Der Meer (1988) and Kreyenschulte et al. (2020) depending on the Reynolds number inside the porous armor.

Figure 6.9(a) shows the three fits done for constant values of $\chi$ (the three vertical lines). Although each author's data go for different values, the trends are the same for both: (1) the lower the value of $log(\chi)$, the higher the value of $Ru$; and (2) for the same value of $\chi$, higher values of $D_a/H$ produce lower run-up.

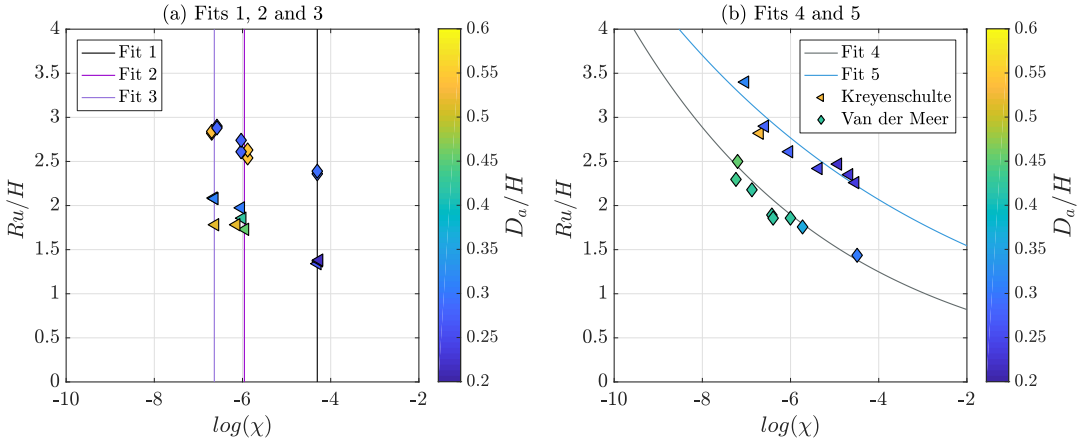


FIGURE 6.9: Non-dimensional run-up versus $log(\chi)$ for the 1:3 slopes, for the five lines fitted in Figure 6.7.

Figure 6.9(b) shows the two fits done for variable values of $\chi$. The fits tried to be perpendicular to the fits with constant $\chi$, to be able to cover the largest number

of breaker types. Straight lines in the experimental space produce exponential fits when drawing the run-up produced by each trial. The grey line, adjusted to leftmost points in Figure 6.7, produces lower values of $Ru/H$, as happened for the smooth impermeable case, while the rightmost points produces the "maximum" available run-up for those tests. As before, it is to be expected that tests closer to the generation limits, with the highest possible value of wave height, $H$, and wave period, $T$, will produce the maximum run-up (and run-down) values.

TABLE 6.4: Fit parameters from the exponential function ($f = a \cdot e^{bx}$): blue and grey lines in Figure 6.8.

| | $a$ | $b$ |
|---|---|---|
| Fit 4 | 0.539 | -0.209 |
| Fit 5 | 1.154 | -0.145 |

### 6.4.2 Sigmoid function

In Chapter 5, to analyze de influence of the breaker types in the dissipation coefficient, $D^*$ was plotted against the $\chi$ parameter, and the data was fitted to a sigmoid function and related to the total water excursion. Besides, for the 1:10 slope, it was possible to identify the transition between the breakers. In this case, the available data has steeper slopes, so the transition between breakers is difficult to know with out experimental tests, however, in Figure 6.6, it was possible to estimate where they would occur.

Another way to examine where they could occur is through the sigmoid function. In this case, Broekhoven (2011) and Kreyenschulte et al. (2020) provided data of the reflection coefficient, so it is possible to calculate the dissipation by means of Equation 2.5, where the transmission coefficient is 0 due to impermeability of the core and non overtopping conditions.

In Figure 6.10, the bulk dissipation coefficient, $D^*$, is plotted versus the alternate similarity parameter, $\chi$, as a function of the relative diameter of the armor, $D_a/H$. The data is plotted separated by slope angles. Sigmoid functions have been fitted in ranges of $D_a/H$. The dotted lines appear where there is no data and are estimates of how the function varies in that area.

In Figure 6.10(a), the data from Broekhoven (2011) for a 1:1.5 slope is presented. In this case, the values of $D_a/H$ are divided into three ranges: $[0.2 \leq D_a/H < 0.6]$, $[0.6 \leq D_a/H < 1.0]$ and $[1.0 \leq D_a/H < 1.4]$. It can be seen that for lower values of $D_a/H$ (the blue fitted function), for the same value of $\chi$, there is lower dissipation than for higher values of $D_a/H$ (the yellow function). For the blue line, the estimation is to reach the no-dissipation conditions around $log(\chi) \approx -11$, while for the yellow line, it reaches it around $log(\chi) \approx -12.5$.

In the case of the 1:2 slope, Figure 6.10(b), only two ranges of $D_a/H$ were identified: $[0.2 \leq D_a/H < 0.6]$ and $[0.6 \leq D_a/H < 1.0]$, and the differences among them are more evident. It should also be noted that the dissipation is generally higher, so that for data with less than $D^* < 0.5$, the estimations are more variable. What is demonstrated is that for the same value of $\chi$, $log(\chi) = -6$, there is more than a 0.1 difference in the dissipation, a considerable difference for technical engineering.

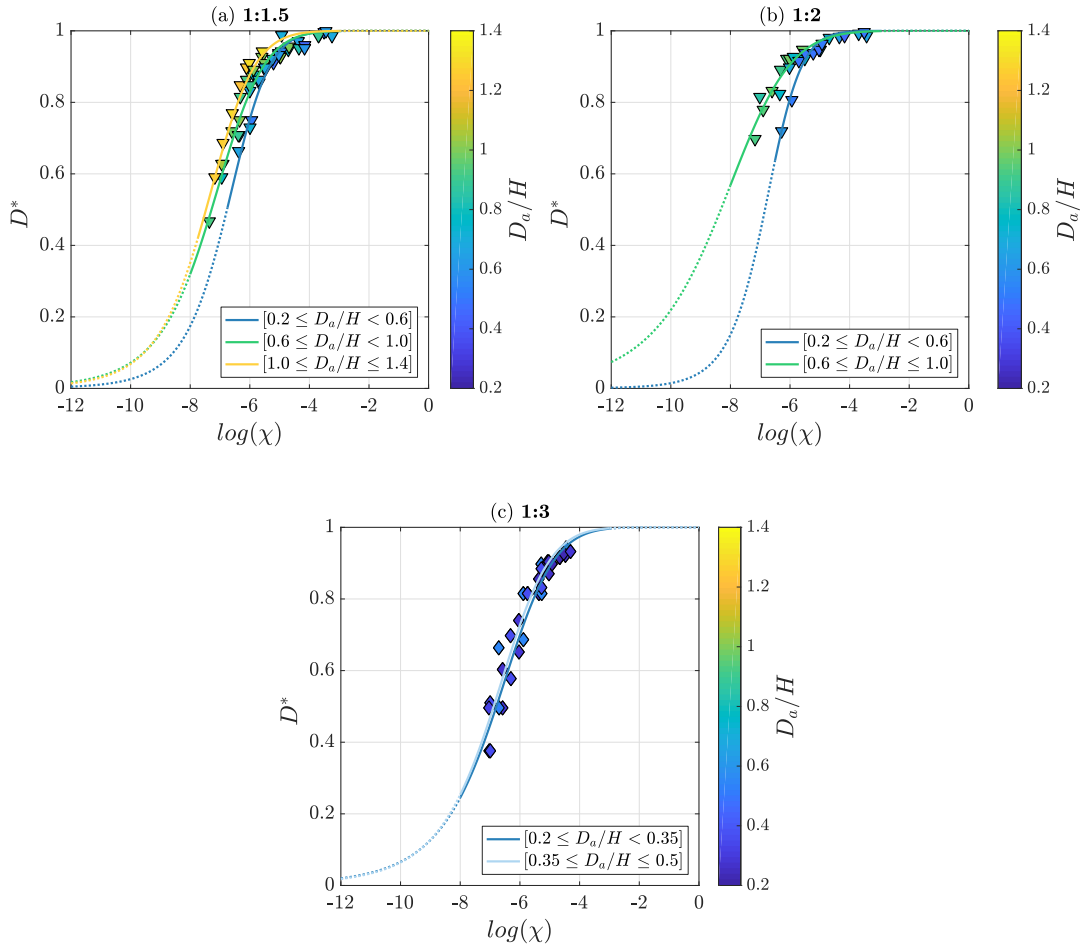


FIGURE 6.10: Bulk dissipation coefficient versus the logarithmic transformation of $\chi$, as a function of $D_a/H$. Sigmoid functions have been fitted to the points in ranges of $D_a/H$. (a) shows the data for a 1:1.5 slope, (b) for a 1:2 slope and (c) for a 1:3 slope.

Figure 6.10(c) shows the data for a 1:3 slope from Kreyenschulte. In this case, the values of $D_a/H$ are lower than for Broekhoven: $[0.2 \leq D_a/H < 0.3]$ and $[0.3 \leq D_a/H < 0.5]$ and the differences are less appreciable and the sigmoid functions are almost parallel.

Table 6.5 shows the parameters of the sigmoid functions fitted to the armored impermeable experimental results of $D^*$ against $log(\chi)$, as a function of the relative diameter, $D_a/H$. It can be seen how the values of $a_x$ increases as the values of $D_a/H$ increases. For the case of the 1:3 slope, both values $a_x$ and $\gamma_x$ are quite similar, as the fitted functions are in Figure 6.10(c).

TABLE 6.5: Fit parameters for the sigmoid function fitted to the bulk dissipation against $log(\chi)$ as a function of $D_a/H$ (Y: yellow, G: green, B: blue, LB: light blue and DB: dark blue) in Figure 6.10.

| | 1:1.5 | | | 1:2 | | 1:3 | |
|---|---|---|---|---|---|---|---|
| | Y | G | B | G | B | LB | DB |
| $Y_0$ | 1 | 1 | | 1 | 1 | 1 | 1 |
| $Y_1$ | 0 | 0 | 0 | 0 | 0 | 0 | 0 |
| $a_x$ | -7.47 | -7.28 | -6.76 | -8.32 | -6.84 | -6.88 | -6.78 |
| $\gamma_x$ | -8.95 | -8.07 | -9.27 | -6.92 | -11.08 | -7.16 | -6.84 |

## 6.5 Conclusions

The objectives of this Chapter were twofold: (a) to estimate the flow characteristics on armored impermeable non-overtopabble slopes with different slope angles under regular and irregular waves, and (b) to estimate the bulk dissipation coefficient $(D^*)$ produced by the breaking waves and by the turbulence generated in the pores of the main armor. To accomplish these objectives, one source of experimental data has been used: published physical experiments on non-overtopabble armored impermeable slopes in 2D wave flumes by different authors (Van Der Meer, 1988; Broekhoven, 2011; Kreyenschulte et al., 2020). From this study the following conclusions can be drawn:

1. Based on dimensional analysis (Chapter 2), the alternate slope similarity parameter $(\chi)$, combined with the relative diameter of the armor $(D_a/H)$, are suggested for the analysis of flow characteristics on armored impermeable slopes under regular and irregular waves.

2. By plotting $Ru$ versus $\chi$ and using $D_a/H$ as the third variable, a good visualization of how the run-up is affected by dissipation caused by the breaking waves and in the armor, respectively, is obtained. This provides a tool to define the wave energy transformation domains on the slope. As for the smooth impermeable case (Chapter 5), the largest deviation of the experimental data are expected to occur at the transitions between weak bore, strong bore and strong plunging breaker types.

3. The sigmoid function fits reasonably well to the run-up data versus $(h/L)(H/L)$. It is possible to define ranges of the relative diameter to fit each range, highlighting the influence of this parameter on energy transformation. The blending parameter of the sigmoid function $(a_x)$ is the value of the parameter $\chi = h/L \cdot H_I/L$ where the inflection point is located. This parameter can be used to separate the reflective predominance and the dissipative predominance domains.

# 7 Flow characteristics on permeable slopes

**Comment**

This section presents some of the results published on:

**Moragues, M.V.**, Clavero, M., Díaz-Carrasco, P. and Losada, M.A. (2020) "Bulk dissipation and flow characteristics in cube armored breakwaters". In: *Proceedings of the 36th International Conference on Coastal Engineering (vICCE20)*.
DOI: https://doi.org/10.9753/icce.v36v.structures.40

*"Global warming has already triggered a sea level rise that could reach from 6 metres to 25 metres."*

James Hansen

*As done in the previous Chapters, based on dimensional analysis, the alternate similarity parameter has been combined with the dimensionless armor and core variables to analyze the flow characteristics over a permeable structure. Once analyzed the effect of the types of breakers and the main armor in the run-up, the influence of a permeable core can be studied. Using experimental data from the current-wave flume of the IISTA and from two previous published works from other authors, the flow characteristics have been analyzed depending on the slope angle. Besides, the bulk dissipation $(D^*)$ has been fitted to a sigmoid function depending on the relative armor diameter and a bulk dissipation coefficient $(B_S)$ has been estimated through the incident wave's celerity. Since the dissipation and the total water excursion in the slope have the same behavior (the sigmoid function correctly identifies it), a "run-up coefficient $(R_S)$" has been proposed, also calculated by the incident wave celerity.*

## 7.1 Introduction

Following Chapters 5 and 6, where the run-up and run-down were analyzed on a smooth impermeable slope and an armored impermeable slope, being the main variables that affect them the slope angle $(\alpha)$, the relative water depth $(h/L)$, the wave steepness $(H/L)$ and the relative diameter of the main armor $(D_a/H)$, the next step for the study is to analyze the influence of a porous core protected by an armor.

The influence of the core is mainly caused by the accumulation of water in the porous medium. The more permeable the material, the easier it is for water to enter and exit. The water level inside the material is also influenced by the period of the incident wave and of course, by the type of breaker, since as seen above, in plunging or spilling breaks, the water does not drop below the mean level at rest, causing more water to accumulate inside the core.

This means that the flow characteristics, in addition to being affected by the dissipation caused by wave breaking and by the porosity of the amor, will be influenced by the permeability and porosity of the core. So there are three main sources of dissipation that should be analyzed separately.

In addition to the variables described in Chapter 6, in the case of a permeable core, the variables involved in the process are also the nominal diameter of the core pieces $(D_{c,n50})$, their density $(\rho_c)$ and the relative width of the core of the structure $(B^*)$, as seen in Figure 7.1.

## 7.2 Experimental set-up and data from other authors

### 7.2.1 Wave-current flume

To achieve the objectives of this research, a series of experimental test were done in the he Andalusian Institute for Earth System Research (IISTA) wave flume. This flume has 23 $m$ long, 0.65 $m$ width and 0.9 $m$ height. The wave-maker is a piston-type paddle generator with an active wave reflection system in order to absorb the reflected waves on the breakwater. The flume has a dissipation ramp behind the paddle and at the end of it.

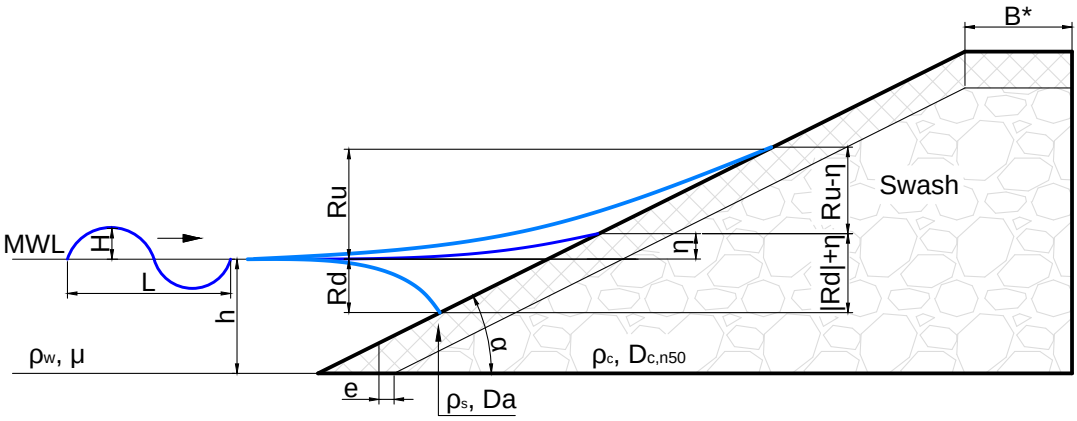


FIGURE 7.1: Scheme of the geometrical parameters affecting run-up and run-down in a permeable slope.

The tested model was a non-overtopped rubble mound breakwater with a crown wall (RMB-CW), as shown in Figure 7.2. The breakwater consisted on a core made of fine gravel ($D_{c,n50} = 12mm$, $\rho_s = 2.83t/m^3$ and $n_c = 0.391$) and a main armor layer made of either one or two layers of cubes of different sizes. The geometrical characteristics of each model tested are plotted in Table 7.1 with the following common configurations: freeboard $F_c = 0.25m$, porous medium height $F_{MT} = 0.55m$, impermeable caisson width $B = 0.5m$, foundation height $h_b = 0.1m$ and slope angle 1:1.5. Water depth was kept constant at $0.4m$.

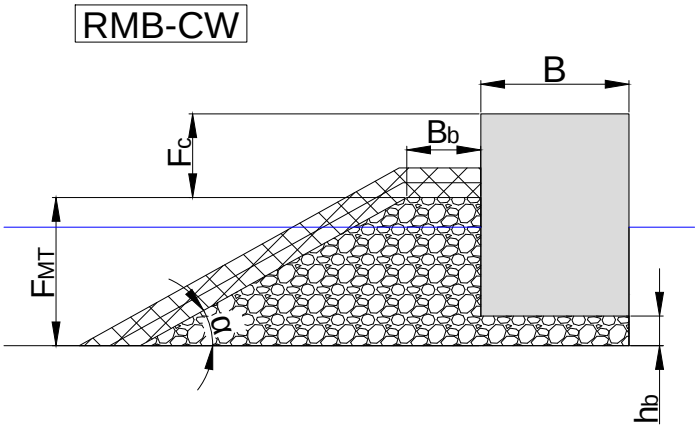


FIGURE 7.2: Scheme of the breakwater tested in the current-wave flume: a rubble-mound breakwater with crown wall consisting of a porous core and a main armor of cubes.

TABLE 7.1: Porous material of the armor layers properties: cube size, characteristic diameter and dry density.

| $Size(mm)$ | $D_a(mm)$ | $\rho_a(t/m^3)$ |
|---|---|---|
| 25 | 31.0 | 2.07 |
| 33 | 40.9 | 2.18 |
| 38 | 47.1 | 2.20 |
| 44 | 54.6 | 2.21 |
| 65 | 80.6 | 2.27 |

Irregular waves were generated following a Jonswap-type spectrum with a 3.3

peak enhancement factor ($\gamma$). The characteristics of the generated waves were two different wave heights for each wave period as shown on Table 7.2.

Seven resistance gauges were placed along the flume to measure the free surface elevations with a sampling frequency of 20 Hz (Figure 7.3). In these tests, the most important gauge is number 7, which is the one in charge of measuring the run-up and run-down at the slope of the structure.

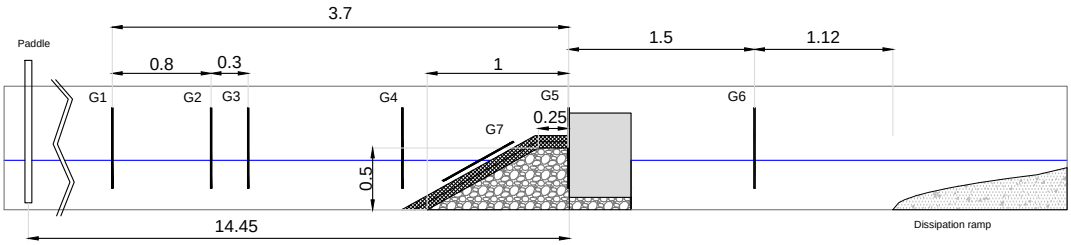


FIGURE 7.3: Diagram of the current-wave flume and wave gauges position for the 1:1.5 slope (measurements in meters).

The hydraulic performance of the breakwater was calculated from gauges G1-G3, applying Baquerizo (1995)'s method which separates the incident and the reflected wave trains. The root mean square of the total wave height at the toe of the structure was calculated from gauge G4 and the root mean square of the wave height on the crown wall was obtained from gauge G5. Using gauge G6 the root mean square of the transmitted wave was calculated and the ratio of the incident wave height and the transmitted wave height gave the transmission coefficient. The reflection coefficient and its phase ($K_R$ and $\phi$) were calculated from the separated incident and reflected waves. After the separation of the incident waves, the statistical parameters had been calculated.

TABLE 7.2: Summarized test conditions of the tests carried out at the wave-current flume. $H_I$ is the incident wave height, $T_z$ is the mean wave period, $Ir$ is the Iribarren number or surf similarity parameter, $h$ is the water depth at the toe of the structure, $\overline{Ru}$ is the mean run-up value and $\overline{Rd}$ is the mean run-down value.

| Parameter | A |
|---|---|
| $\boldsymbol{H_I}(m)$ | 0.0208 - 0.0576 |
| $\boldsymbol{T_z}(s)$ | 0.9407 - 4.3182 |
| $\boldsymbol{H_I/L}$ | 0.0029 - 0.0408 |
| $\boldsymbol{Ir}$ | 3.2997 - 12.4604 |
| $\boldsymbol{h}(m)$ | 0.4 |
| $\overline{\boldsymbol{Ru}}(m)$ | 0.0125 - 0.0656 |
| $\overline{\boldsymbol{Rd}}(m)$ | (-0.0500) - (-0.0128) |

### 7.2.2 Data from other authors

#### Van Der Meer (1988) and Van Der Meer and Stam (1992)

Van Der Meer (1988) and Van Der Meer and Stam (1992) conducted a series of tests on permeable and impermeable structures. The general conditions of the tests were explained in the Section 6.3.1. The particular characteristics of these tests are

summarized in the Table 7.3. The provided value for the run-up measurements is the 2% exceedance run-up.

TABLE 7.3: Summarized test conditions of the tests carried out by Van Der Meer (1988) and Van Der Meer and Stam (1992). $H_{m0}$ is the energy-based wave height, $T_p$ is the peak wave period, $H_{m0}/L$ is the wave steepnees, $Ir$ is the Iribarren number or surf similarity parameter, $h$ is the water depth at the toe of the structure and $Ru_{2\%}$ is the run-up exceeded by two per cent of the incoming waves.

| Parameter | Permeable |
|---|---|
| Number of tests | 54 |
| $\boldsymbol{tan(\alpha)}$ | 1:1.5, 1:2, 1:3 |
| $\boldsymbol{H_{m0}(m)}$ | 0.085 - 0.18 |
| $\boldsymbol{T_p(s)}$ | 1.39 - 3.51 |
| $\boldsymbol{H_{m0}/L}$ | 0.011 - 0.056 |
| $\boldsymbol{Ir}$ | 1.47 - 8.87 |
| $\boldsymbol{h(m)}$ | 0.8 |
| $\boldsymbol{Ru_{2\%}(m)}$ | 0.113 - 0.348 |
| $\boldsymbol{D_{n50,a}}$ | 0.036 |
| $\boldsymbol{e}$ | 0.08 |
| $\boldsymbol{\rho_a}$ | 2620 |
| $\boldsymbol{B^*}$ | 0.50 |
| $\boldsymbol{D_{n50,c}}$ | 0.011 |

**Broekhoven (2011)**

Broekhoven (2011) conducted a series of experimental tests to study the influence of the structure permeability on the run-up. The general conditions of the tests were explained in the Section 5.2.3, while the particular characteristics are shown in Table 7.4.

### 7.2.3 Hydrodynamic flow regimes of the analyzed data

As done in Sections 5.2.4 and 6.3.2, an analysis of the hydrodynamic regimes has been made to see how each test has been done and if, in spite of studying them together in this work, there are hydrodynamic differences between them. Figure 7.4 represent the aforementioned described data in the Le Méhauté abacus (Le Méhauté, 1976).

Figure 7.4 shows that the second-order Stokes theory range applied to most of the data from the IISTA physical tests and the analytical solution should contain at least the second power term proportional to $H^2$ that is characteristic of the non-linear behavior. Moreover, Broekhoven's data, as well as for the impermeable cases, most of its points are located between the Stokes $2^{nd}$ and $3^{rd}$ order.

Figure 7.5 represents the flow in the porous core for the physical tests, using the diagram proposed by Gu and Wang (1991) in terms of the Reynolds number inside the porous material $(Re_c)$ and the Keulegan-Carpenter number $(KC_c)$. All of the tests conducted with the porous core and main armor layer took place in the region where the three forces (laminar $f_L$, inertial $f_I$ and turbulent $f_T$ ) are equally important

TABLE 7.4: Summarized test conditions of the tests carried out by Broekhoven (2011). $H$ is the mean wave height, $T$ is the mean wave period, $H/L$ is the wave steepness, $Ir$ is the Iribarren number or surf similarity parameter, $h$ is the water depth at the toe of the structure and $\overline{Ru}$ is the mean run-up.

| Parameter | Permeable |
|---|---|
| Number of tests | 59 |
| $tan(\alpha)$ | 1:2 |
| $H(m)$ | 0.068 - 0.147 |
| $T(s)$ | 0.9 - 3.2 |
| $H/L$ | 0.01 - 0.091 |
| $Ir$ | 1.68 - 7.42 |
| $h(m)$ | 0.5 |
| $\overline{Ru}(m)$ | 0.051 - 0.19 |
| $D_{n50,a}$ | 0.067 |
| $e$ | 2*Da |
| $\rho_a$ | 2610 |
| $n_a$ | 0.41 |
| $B^*$ | 0.30 |
| $D_{n50,c}$ | 0.033 |
| $\rho_c$ | 2590 |
| $n_c$ | 0.36, 0.43 |

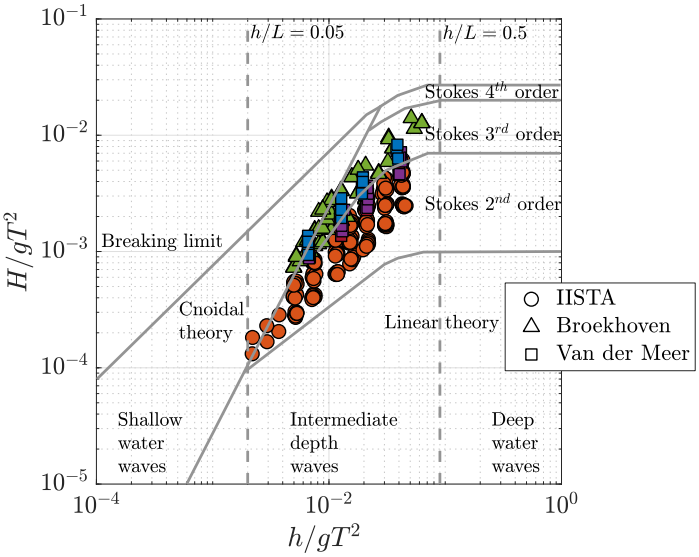


FIGURE 7.4: Data from the experimental tests done at the IISTA current-wave flume and from the other authors represented together with the limits of validity for various wave theories (Le Méhauté, 1976).

with values exceeding the threshold where the flow regime is fully turbulent ($Re_c > 300$).

### 7.2.4 Dimensional analysis

Based on Chapter 2, if the slope of the structure is non-overtoppable, with a main armor and has a permeable core, the functional to analyze its behavior is as shown in Equation 7.1.

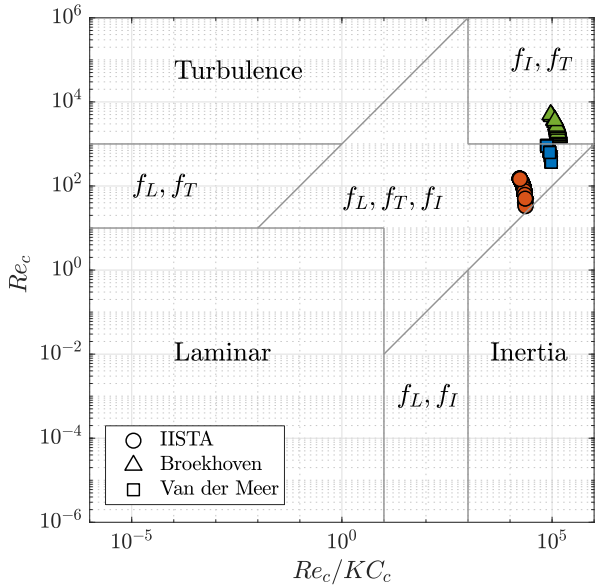


FIGURE 7.5: Importance of the resistance forces (diagram from Gu and Wang (1991)) in the studied tests.

$$\frac{X}{H_I} = \left(\frac{Ru}{H_I}, \frac{Rd}{H_I}, \frac{\eta_m}{H_I}\right) = f_\alpha \left(\frac{H_I}{L}, \frac{h}{L}, \frac{D_{a,n50}}{H_I}, Re_p, \frac{B}{L}, \frac{D_{c,n50}}{L}\right) \tag{7.1}$$

In Figure 7.6, the data sets from the aforementioned authors are presented in the experimental space $[log(H/L) - log(h/L)]$. The data is classified by slopes: Figure 7.6(a) represents the data for a 1:1.5 slope, (b) for a 1:2 slope and (c) for a 1:3 slope. Figure 7.6(a) shows the experimental space for the IISTA wave-current flume. As the experimental technique consisted of maintaining a constant period while increasing the wave height, the data appears in groups with constant values of $h/L$. The main difference with the data from other authors is that this tests have lower values of relative water depth and wave steepness ($log(h/L) < -3$ and $log(H_I/L) < -5$). This means that the area of the parallelepiped is bigger, and so, more breaker types would be expected.

The data for each author has a particular behavior, in general the same presented for the armored impermeable structures (Chapter 6). Broekhoven (2011)'s data follows a linear relation between $log(h/L)$ and $log(H/L)$, while Van Der Meer (1988)'s data is organized in groups of points with constant values of $h/L$ while varying the wave steepness. Despite the experimental technique was the same for Van der Meer's data and the IISTA tests, for each value of $h/L$, the combinations of $H/L$ is also wider (i.e. for a value of $log(h/L) = -1.5$, Van der Meer's data goes from $[-3.5 \leq log(H/L) \leq -3]$, while the IISTA data goes from $[-4.2 \leq log(H/L) \leq -3]$).

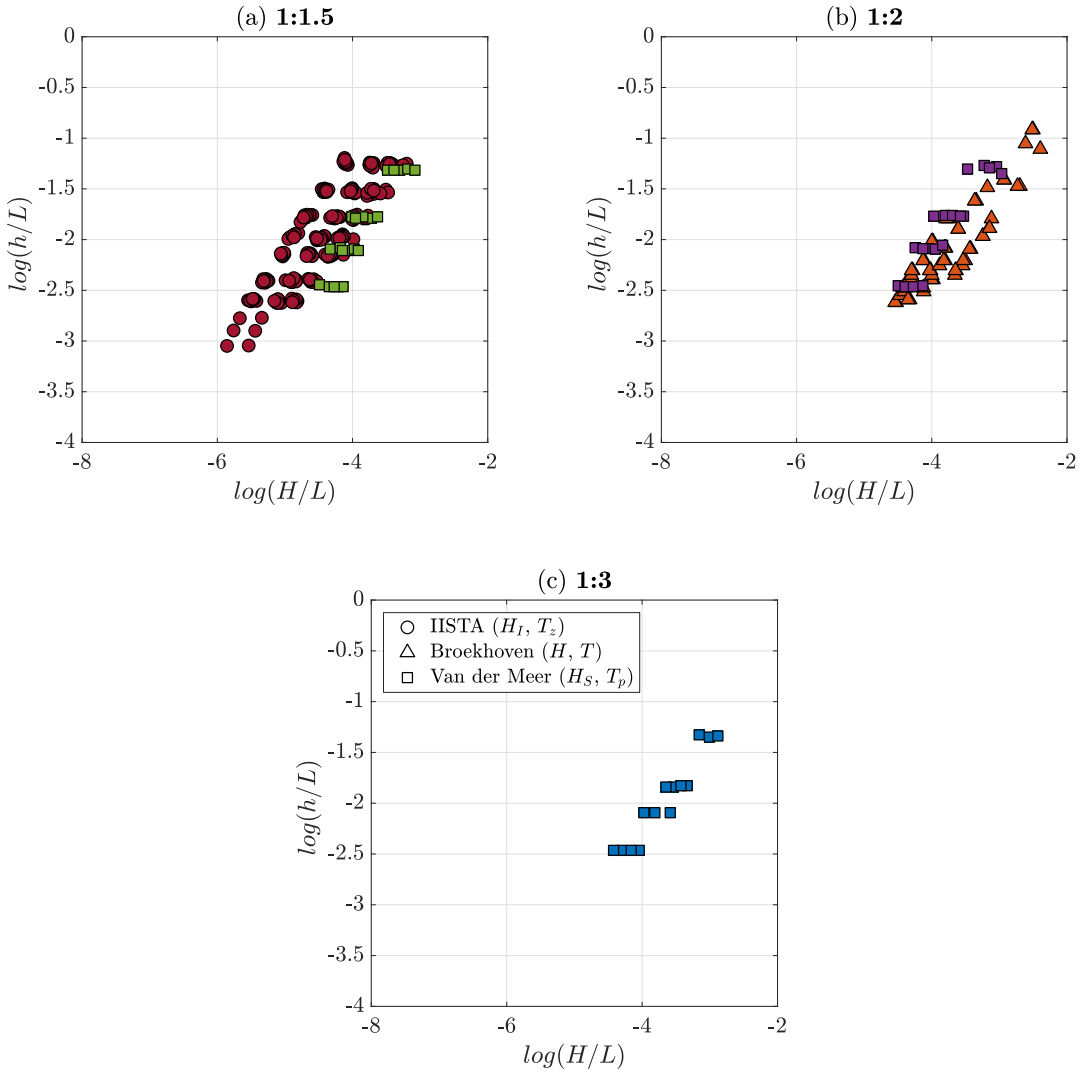


FIGURE 7.6: Experimental space $[log(H_I/L) - log(h/L)]$ classified by slopes (a) for a 1:1.5 slope, (b) for a 1:2 slope and (c) for a 1:3 slope. Symbols represent the data for each author and colors are different for each slope angle.

## 7.3 Results

### 7.3.1 Run-up

First of all, the non-dimensional run-up has been plotted against the logarithmic transformation of the alternate similarity parameter ($\chi$). In Figure 7.7, the data has been classified by slope angles: (a) 1:1.5, (b) 1:2 and (c) 1:3. It can be seen how the data does not follow any visual trend (except maybe the data from Van der Meer for a 1:2 slope). All points lie within a range of $\chi$ values of $[-7.5 < log(\chi) < -3.5]$. This means that breakers are expected to be between strong plunging, strong bore or weak bore. However, just the progression between breakers does not explain the scatter of the data.

Figure 7.7(a) shows the data from the wave-current flume of the IISTA. The data appears to be quite organized, without to much scatter, going from $[0.5 < Ru/H_I < 1.75]$ as the values of $\chi$ decrease. This result is consistent with the results obtained

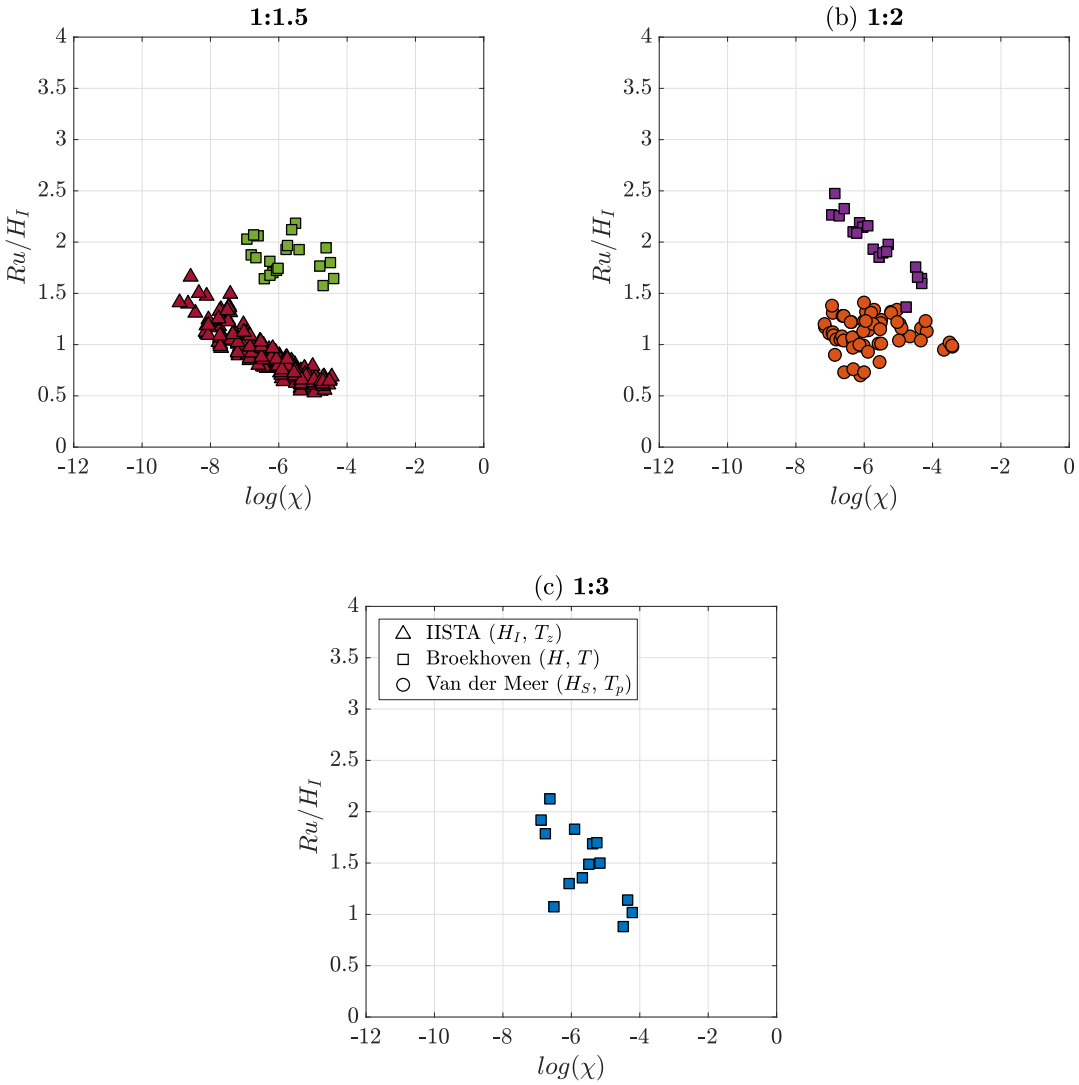


FIGURE 7.7: Non-dimensional run-up versus the logarithmic transformation of $\chi$, classified by slopes (a) for a 1:1.5 slope, (b) for a 1:2 slope and (c) for a 1:3 slope. Symbols represent the data for each author and colors are different for each slope angle.

in Chapter 5. However, due to the differences in the main armor of the breakwater, for the same value of $\chi$, there is more or less a variability of 0.5 in the run-up values. Also, Van der Meer's data is presented and although the $\chi$ range coincides with the IISTA data, the non-dimensional run-up values are almost double and have greater scatter. Whether this variability is produced by the main armor, the core or both, will be discussed later.

Figure 7.7(b) shows the data from Van Der Meer (1988) Broekhoven (2011) for a 1:2 slope. In this case, Van der Meer's data have a lineal trend, increasing $Ru/H$ while decreasing $log(\chi)$. However, Broekhoven's data, with the same range of $\chi$, is more disperse with variations between $[0.6 \leq Ru/H \leq 1.5]$ for the same $\chi$. In Chapter 5, this variation was caused bu the position of the points inside the experimental space, but this is not the case now, because Broekhoven's data in Figure 7.6(b) appear close enough together so as not to cause this scattering.

Figure 7.7(c) shows the data from Van Der Meer (1988) for the 1:3 slope. In this

case, the run-up values are lower than in the previous slopes, and although they grow as $\chi$ decreases, they also have enough variability that a function cannot be fitted.

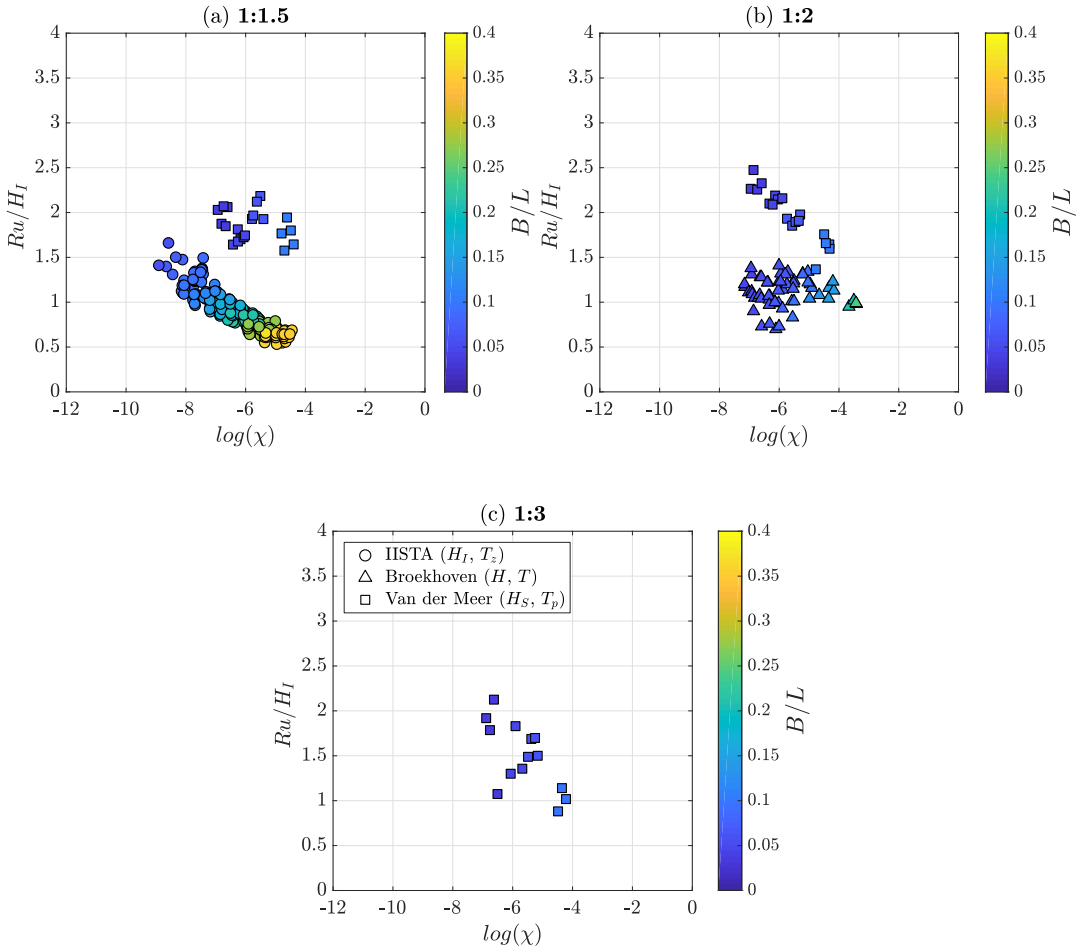


FIGURE 7.8: Non-dimensional run-up versus $log(\chi)$, classified by slopes (a) for a 1:1.5 slope, (b) for a 1:2 slope and (c) for a 1:3 slope. The colorbar represent the values of $B/L$. Symbols represent the data for each author and colors are different for each slope angle.

Figure 7.8 represents the same run-up values depending on the relative with of the breakwater $(B/L)$. Losada et al. (1995) and Pérez-Romero et al. (2009) concluded that for values of $B/L < 0.2$, the saturation regimen is never reached, meaning that the performance of the structure will be governed by the changes in the flow regime. This is the case for almost all the data points analyzed, except for some points of the IISTA tests. On the other hand, all the tests for each author have the same width, meaning the relative width only changes due to the wavelength. Taking all this into account, the influence of $B/L$ has been overlooked.

From now on in this section, the data have been analyzed depending on the slope angle. First of all the data for a 1:2 slope have been analyzed. Figure 7.9 shows the non-dimensional run-up data versus the logarithmic transformation of the alternate similarity parameter with the relative diameter of the armor in the colorbar. As seen in the previous chapter, the influence of the armor produces higher or lower values of run-up for the same value of $log(\chi)$. In this case, Broekhoven's values of $D_a/H \approx 1$ produce run-up between $[0.75 < Ru/H < 1]$ and $D_a/H \approx 0.5$ between

$[1.25 < Ru/H < 1.45]$. For Van der Meer's data the influence is less appreciable since its $D_a/H$ range is small ($[0.22 < D_a/H < 0.41]$).

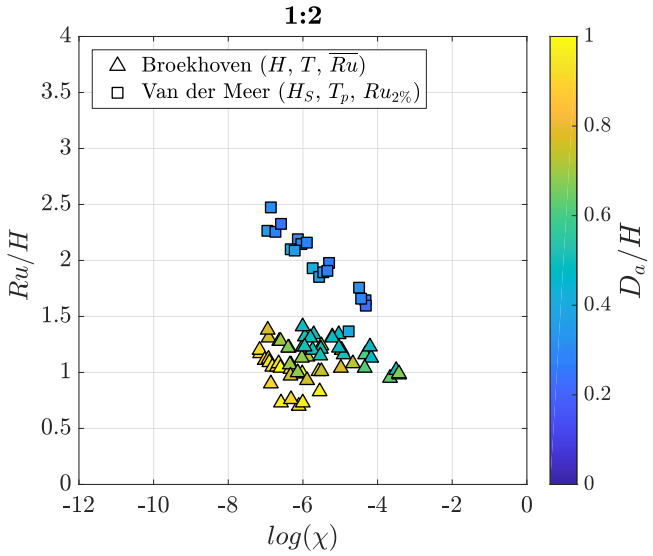


FIGURE 7.9: Non-dimensional run-up versus $log(\chi)$, for 1:2 slope data, depending of $D_a/H$.

In order to analyze the influence of the core of the structure on the run-up heights obtained without taking into account the effect of the armor and the types of breaking, it was decided to choose $D_a/H$ ranges and analyze the impact of the relative diameter, $D_c/L$. The chosen ranges were: $[0 \leq D_a/H < 0.25]$, $[0.25 \leq D_a/H < 0.40]$, $[0.40 \leq D_a/H < 0.55]$, $[0.55 \leq D_a/H < 0.70]$, $[0.70 \leq D_a/H < 0.85]$ and $[0.85 \leq D_a/H]$. In Figure 7.10, this ranges are shown in each subplot, while the data is colored depending on the values of $D_c/L$. In Figures 7.10(a), (b) and (c), the data from Van Der Meer (1988) has values of $D_c/L$ relatively low ($D_c/L \leq 0.039$). However, Broekhoven's data (Figures 7.10c, d, e and f) show how the higher the values of $D_a/H$ the lower the values of the run-up, and these in turn, show how the tendency is to produce lower run-up for values with higher values of $D_c/L$.

Focusing on Broekhoven's data, it is hereby proven that the relative diameters of both the armor and the core are able to correctly characterize the run-up as a function of $log(\chi)$. However, Broekhoven conducted tests with the same core diameter and different grading and this situation can be seen especially in Figures 7.10(e) and (f). The data points follow two parallel lines, one for each core grading.

### 7.3.2 Sigmoid function

As seen in the previous Chapters, the sigmoid function is able to characterize the wave energy transformation and the total water excursion on the slope while they are plotted against the logarithmic transformation of the alternate similarity parameter.

Figure 7.11 shows the bulk dissipation coefficient and the total water excursion plotted against $log(\chi)$ for the IISTA tests done in the wave-current flume with a 1:1.5 slope. The color bar indicates the values of the relative diameter of the armor ($D_a/H_I$). The sigmoid functions have been fitted in ranges of these values. This

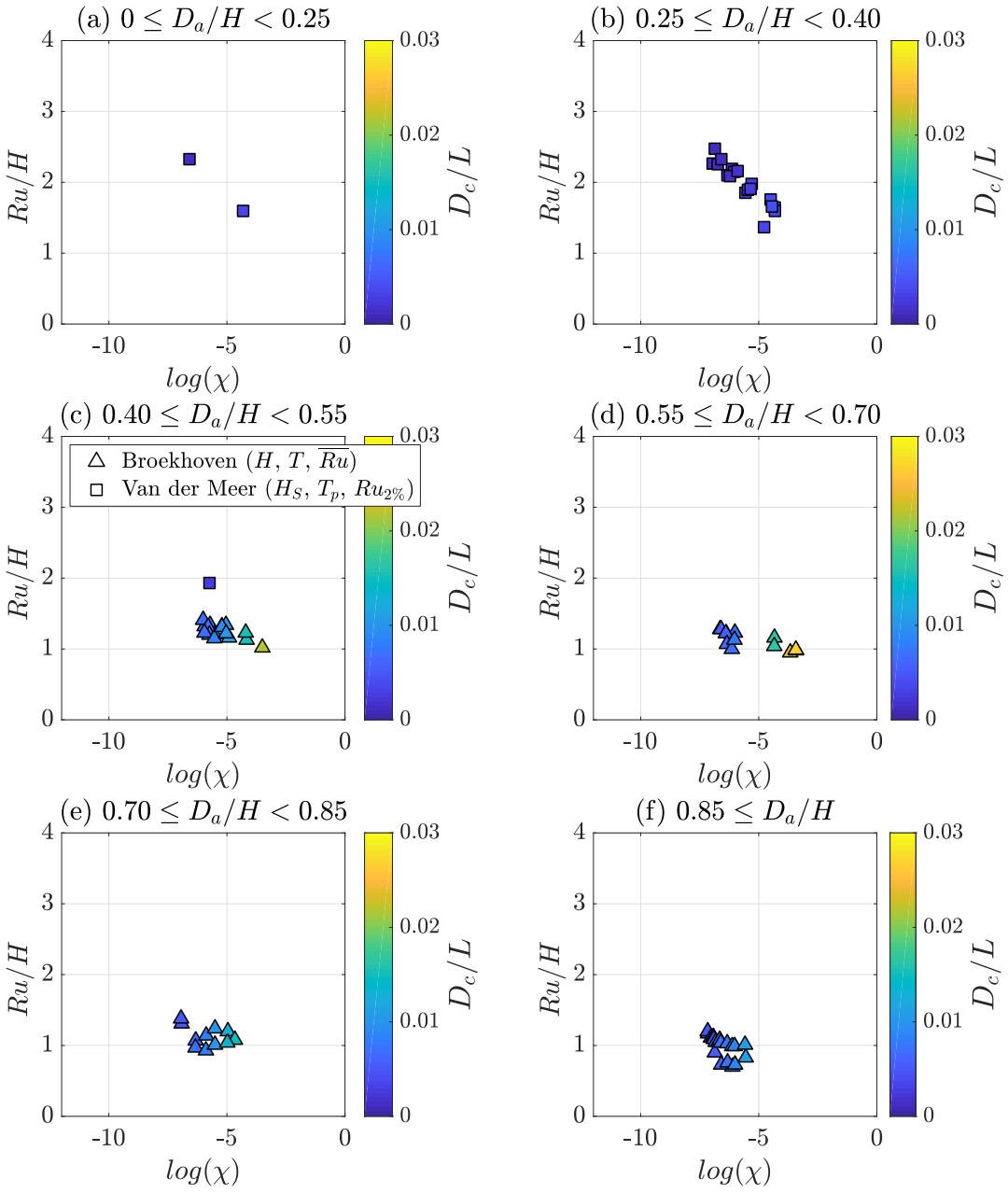


FIGURE 7.10: Non-dimensional run-up versus the logarithmic transformation of $\chi$, for a 1:2 slope, classified in ranges of $D_a/H$. The colorbar indicates the values of the relative core diameter $(D_c/L)$.

figure shows how the data is sorted by color, producing more dissipation (and less water excursion), the higher values of the relative diameter.

In Table 7.5 the parameters of the four sigmoid functions are shown. It can be seen how for both, the dissipation and the total water excursion, the inflection point, $a_x$, is lower as the value of $D_a/H_I$ increases. This means that the dissipation is lower for surging or bore breakers with lower values of $D_a/H_I$, and they produce higher values of the total water excursion.

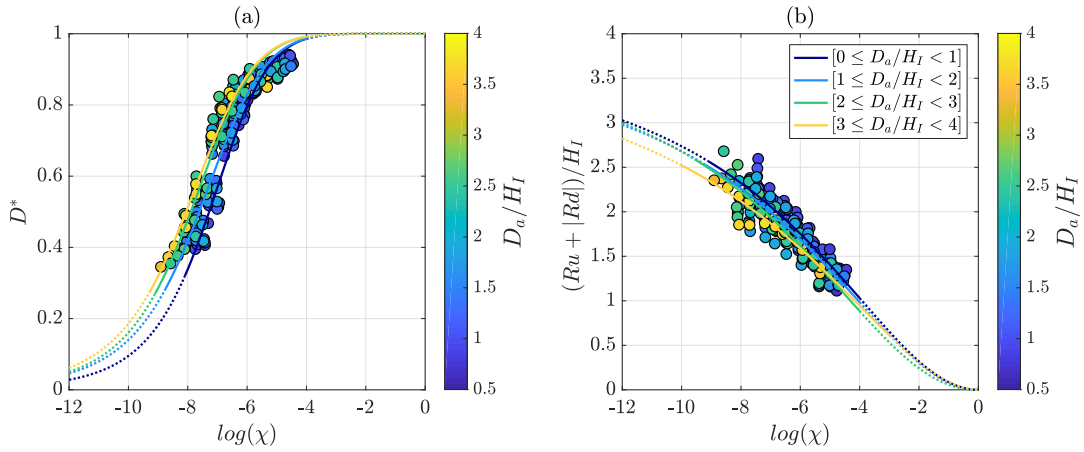


FIGURE 7.11: (a) Bulk dissipation coefficient $(D^*)$ and (b) total water excursion $(Ru + |Rd|)/H_I$ versus $log(\chi)$. Colors indicate the range of values of $D_a/H_I$.

TABLE 7.5: Fit parameters for the sigmoid function fitted to the bulk dissipation against $log(\chi)$ as a function of $D_a/H_I$ (Y: yellow, G: green, LB: light blue and DB: dark blue) in Figure 7.11.

| | $D^*$ | | | | $(Ru + \|Rd\|)/H_I$ | | | |
|---|---|---|---|---|---|---|---|---|
| | DB | LB | G | Y | DB | LB | G | Y |
| $Y_0$ | 1 | 1 | 1 | 1 | 0 | 0 | 0 | 0 |
| $Y_1$ | 0 | 0 | 0 | 0 | 4 | 4 | 4 | 4 |
| $a_x$ | -7.278 | -7.612 | -7.897 | -8.054 | -6.795 | -7.015 | -7.199 | -7.509 |
| $\gamma_x$ | -7.087 | -6.655 | -7.011 | -6.827 | -1.997 | -1.993 | -2.140 | -1.863 |

### 7.3.3 Energy dissipation

In Chapter 4, Section 4.5, the dissipation was estimated through a bulk dissipation coefficient, $B_S$ (Equation 7.2), depending on the characteristics of the incident wave train ($C$, $C_g$, $H_I$ and $T$) at the toe of the slope (Duncan, 1981; Martins et al., 2018).

$$d_* = B_s \frac{8l}{g^2} \frac{C^5}{H_I^2 C g} \tag{7.2}$$

In the same way, the bulk dissipation coefficient has been calculated for the tests done in the current-wave flume. To take into account the dissipation caused in the main armor, the data has been plotted with color depending of $D_a/H_I$. Figure 7.12 shows $B_S$ against $log(\chi)$ while the colorbar shows the values of $D_a/H_I$. Four ranges have been chosen for the fitting lines: $[D_a/H \leq 1.0]$, $[1.0 \leq D_a/H < 2.0]$, $[2.0 \leq D_a/H < 3.0]$ and $[D_a/H \geq 3.0]$. The influence of the core has not been taken into account since it has the same geometrical characteristics for every tests.

Having proved in Chapter 5 that the sigmoid function is able to relate the bulk dissipation $(D^*)$ to the total water excursion $(Ru + |Rd|)/H_I)$, it can be assumed that a "run-up and run-down coefficient" can be obtained, capable of estimating the total water excursion as a function of the characteristics of the incident train at the toe of the slope (Equation 7.3).

Figure 7.13 shows the run-up and run-down coefficient versus $log(\chi)$ depending on the armor characteristics. As seen with the sigmoid functions in Figure 7.11, the points with lower $B_S$ are the ones producing higher $R_S$.

$$\frac{Ru + |Rd|}{H_I} = R_S \frac{\rho}{g} C^5 \tag{7.3}$$

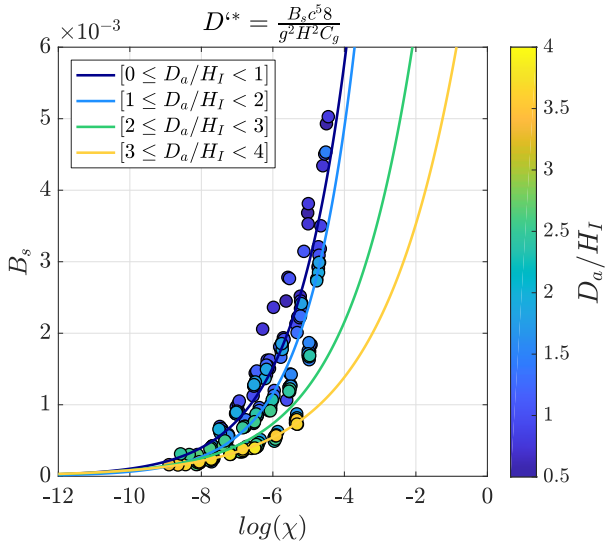


FIGURE 7.12: Bulk dissipation coefficient $(B_S)$ versus $log(\chi)$. Colors indicate the range of values of $D_a/H_I$.

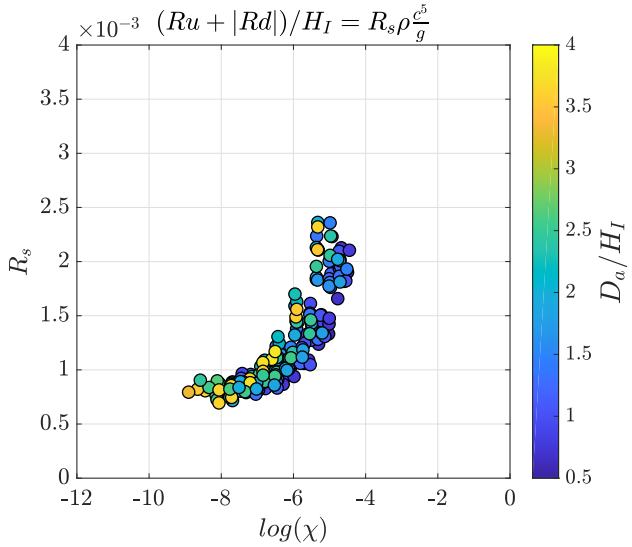


FIGURE 7.13: Run-up and run-down coefficient $(R_S)$ versus $log(\chi)$. Colors indicate the range of values of $D_a/H_I$.

## 7.4 Conclusions

The objectives of this Chapter were threefold (a) to estimate the flow characteristics on armored permeable non-overtopabble slopes with different slope angles under regular and irregular waves, (b) to estimate the bulk dissipation coefficient

$(D^*)$ produced by the breaking waves, the turbulence generated in the pores of the main armor and the permeable core, and (c) to derive a non-dimensional bulk energy dissipation coefficient on the slope, which depends on the breaker type and, therefore, on the value of $\chi$ at the toe of the slope. To accomplish these objectives, two sources of experimental data are considered: physical experimental tests done in the wave-current flume on the IISTA, and published physical experiments on non-overtopabble armored permeable slopes in 2D wave flumes by different authors (Van Der Meer, 1988; Broekhoven, 2011). From this study the following conclusions can be drawn:

1. Based on dimensional analysis (Chapter 2) the alternate slope similarity parameter $(\chi)$, combined with the relative diameter of the armor $(D_a/H)$, and the relative diameter of the core $(D_c/L)$ are suggested for the analysis of flow characteristics on armored permeable slopes under regular and irregular waves.

2. By plotting $Ru$ versus $\chi$ and using $D_c/L$ as the third variable in ranges of $D_a/H$, a good visualization of how the run-up is affected by dissipation caused by breaking waves, in the armor and in the core, respectively, is obtained. This provides a tool to define the wave energy transformation domains on the slope.

3. The sigmoid function fits reasonably well to the run-up data versus $(h/L)(H/L)$, defining ranges of the relative diameter to fit each range of $D_a/H_I$, highlighting the influence of this parameter on energy transformation. The blending parameter of the sigmoid function $(a_x)$ can be used to separate the reflective predominance and the dissipative predominance domains.

4. Two non-dimensional coefficient $(B_S, R_S)$ have been obtained to quantify the bulk dissipation and the total water excursion depending on the characteristics of the incident wave train, $\chi$ and the armor properties.

# 8 Conclusions and future research lines

*"People ask: Why should I care about the ocean? Because the ocean is the cornerstone of earths life support system, it shapes climate and weather. It holds most of life on earth. 97% of earths water is there. Its the blue heart of the planet-we should take care of our heart. Its what makes life possible for us. We still have a really good chance to make things better than they are. They wont get better unless we take the action and inspire others to do the same thing. No one is without power. Everybody has the capacity to do something."*

Sylvia Earle

## 8.1 Conclusions

The main objective of this thesis is to find a methodology for the integrated analysis of the processes occurring in the wave-structure interaction in a sloped breakwater. These specific processes are the energy transformation, specifically the dissipation, and the flow characteristics, run-up and run-down. The main conclusions are organized according to the different specific objectives defined in section 1.2:

1. *To apply dimensional analysis in a global way to obtain all the variables on which the hydraulic performance of the breakwater depends, on impermeable and permeable structures.*

   Dimensional analysis offers a simple methodology to describe physical processes establishing the dependence of physical quantities by using their dimensions. The advantages of dimensional analysis are: (1) the dimension reduction, and (2) scalability of the developed model.

   Four steps are necessary for the dimensional analysis once the dependent quantities are defined: (1) choose a complete set of $n$ independent variables, (2) list a complete dimensionally independent subset of k quantities, (3) define the dimensionless forms of the $n - k$ remaining independent variables, and (4) application of the Buckinghams $\Pi$ theorem to state the dimensionless dependent quantities as a function of the $(n - k)$ dimensionless independent quantities.

   The dimensionless variables on which the wave-structure interaction depends have been found for 3 different types of slopes: smooth impermeable, armored impermeable and permeable. It has been demonstrated that the incident wave variables, measured at the toe of the slope, are fundamental when analyzing the process and neither the relative depth nor the wave steepness can be ignored. In addition, the slope angle, being dimensionless, is left out of the analysis, so the results are only valid for each specific angle.

   Equations 2.22, 2.28 and 2.33 provide the dimensionless variables on which the wave-structure interaction depends on a (1) smooth and impermeable, (2) armored impermeable and (3) permeable slope respectively.

2. *To analyze the breaking processes on a smooth and impermeable slope to avoid dissipation in porous media and use the dimensionless variables identified in the dimensional analysis to identify and classify them.*

   Through new physical experiments conducted on a smooth impermeable slope, six breaker types have been identified and described: surging, weak bore, strong bore, strong plunging, weak plunging and spilling. Dimensional analysis was used to show that the dominant breaker types and their progression/transition depend on three quantities: (1) the characteristics of the incident waves at the toe of the slope, $h/L$ and $H_I/L$; and (2) the slope, $m$. This research showed that the breaker types on a given slope can be well approximated by the log-transform of the alternate similarity parameter $\chi = (h/L)(H_I/L)$.

   The interplay of the relative water depth, the wave steepness and the slope angle, is most accurately and usefully represented by graphic representations in a 2D system in terms of value pairs (taken two by two), while the other

quantity remains constant. Accordingly, it is either possible to combine values of $m$ and $H_I/L$ while $h/L$ remains constant, to combine values of $m$ and $h/L$ while $H_I/L$ remains constant, or to combine values of $h/L$, and $H_I/L$ while $m$ remains constant.

The use of the experimental space could help to develop the experimental design. It made it possible to forecast the types of breaker, as well as the variability of the flow characteristics, wave energy transformation and structure stability.

3. *To study the prevalence and progression of each breaker type and link them to the most common used experimental techniques and derive a bulk dissipation coefficient that depends on the types of breaking and is able to characterize them.*

   The progression of breaker types observed inside the experimental space. As the wave steepness and relative water depth increases, there is a continuous gradation in the type of breaking from surging to spilling. Furthermore, when wave steepness decreases and relative water depth increases but $\chi$ remains constant, the breaker type does not change. In other words, there is no progression of breaker type.

   It is concluded that the transition between breaker types does not occur in a fixed value of $\chi$ but rather they occur progressively between certain values of the alternate similarity parameter. Taking this into account, having studied at which points the transitions occur, it has been possible to conclude that the experimental techniques most commonly used in laboratories do not cover all types of breakers, which means that not all possible results are obtained and often the same tests are repeated, obtaining the same results. A good organization prior to testing can reduce the testing time and thus the economic costs of the tests.

4. *To study the flow characteristics (run-up, run-down and total excursion) on a smooth impermeable slope, estimating the local dissipation caused only by the breaking waves.*

   Based on dimensional analysis, an alternate slope similarity parameter $\chi$, is proposed for the analysis of flow characteristics on impermeable slopes under regular and irregular waves. Plotting $[Ru/H_I, Rd/H_I]$ against $\chi$, gives a good display of the experimental data, and helps to define the wave energy transformation domains on the slope. The largest deviation of the experimental data uses to occur at the transitions between the following types of wave breaker: weak bore - strong bore - strong plunging. These transitions depend on the slope angle.

   However, the same breaker type can produce different run-up values depending on the relative water height of the incident wave $\gamma = H/h$. The generation of regular and irregular wave trains in a horizontal bottom channel limits the $H/h$ values and is a severe constraint for the development of formulas for slope flow characteristics.

   It has also been proven that the higher dimensionless run-up ($Ru/H$) does not have to be produced by the higher height of the water sheet or dimensional run-up ($Ru$). It is therefore important to analyze the relationship between $Ru/H$ and $Ru/h$.

The mean water level is a clear indicator of the breaker types since each type of break stores water in the slope in a different way. In a dissipative regime, the water is accumulated in the slope causing the mean water level to be above the value of the water at rest. In a perfect reflective regime, the run-down and run-up values are almost symmetrical, producing a mean water level at the same level as at rest

The total water excursion on the slope, $(Ru + |Rd|)/H_I$, eliminates the effect of the mean water level by adding the values of the water ascent and descent. In the same way as the run-up and run-down, it has been proven that the total excursion identifies the wave energy transformation regimes. Moreover, can be predicted by knowing the bulk dissipation (or with its complementary value, $K_R^2$), and/or the bulk dissipation coefficient ($B_S$).

Besides, a sigmoid function of the variable $(h/L)(H_I/L)$ fits reasonable well with the experimental results $[Ru/H_I,\ Rd/H_I]$. A poor fit is obtained when the Iribarren number is taken as the independent variable. The blending parameter of the sigmoid function is the value of the parameter $\chi = h/L \cdot H_I/L$ where the inflection point is located. This parameter can be used to separate the reflective predominance and the dissipative predominance domains.

5. *To analyze the flow characteristics on armored impermeable slope and permeable slopes depending on the non-dimensional variables obtained from the dimensional analysis, and to find the parameters on which the dissipation depends for each type of structure.*

Based on dimensional analysis, the alternate slope similarity parameter $\chi$, combined with the relative diameter of the armor $(D_a/H)$, are suggested for the analysis of flow characteristics on armored impermeable slopes under regular and irregular waves. By plotting $Ru$ versus $\chi$ and using $D_a/H$ as the third variable, a good visualization of how the run-up is affected by dissipation caused by the breaking waves and in the armor, respectively, is obtained. Moreover, the sigmoid function fits reasonable well to the run-up data versus $(h/L)(H/L)$. It is possible to define ranges of the relative diameter to fit each range, highlighting the influence of this parameter on energy transformation.

In the case of an armored permeable slope under regular and irregular waves, based on dimensional analysis, the alternate slope similarity parameter $(\chi)$, combined with the relative diameter of the armor $(D_a/H)$, and the relative diameter of the core $(D_c/L)$ are suggested for the analysis of flow characteristics. The sigmoid function fits reasonable well to the run-up data vs $(h/L)(H/L)$, defining ranges of the relative diameter to fit each range, highlighting the influence of this parameter on energy transformation. Two non-dimensional coefficients $(B_S, R_S)$ have been obtained to quantify the bulk dissipation and the total water excursion depending on the characteristics of the incident wave train, $\chi$ and the armor properties.

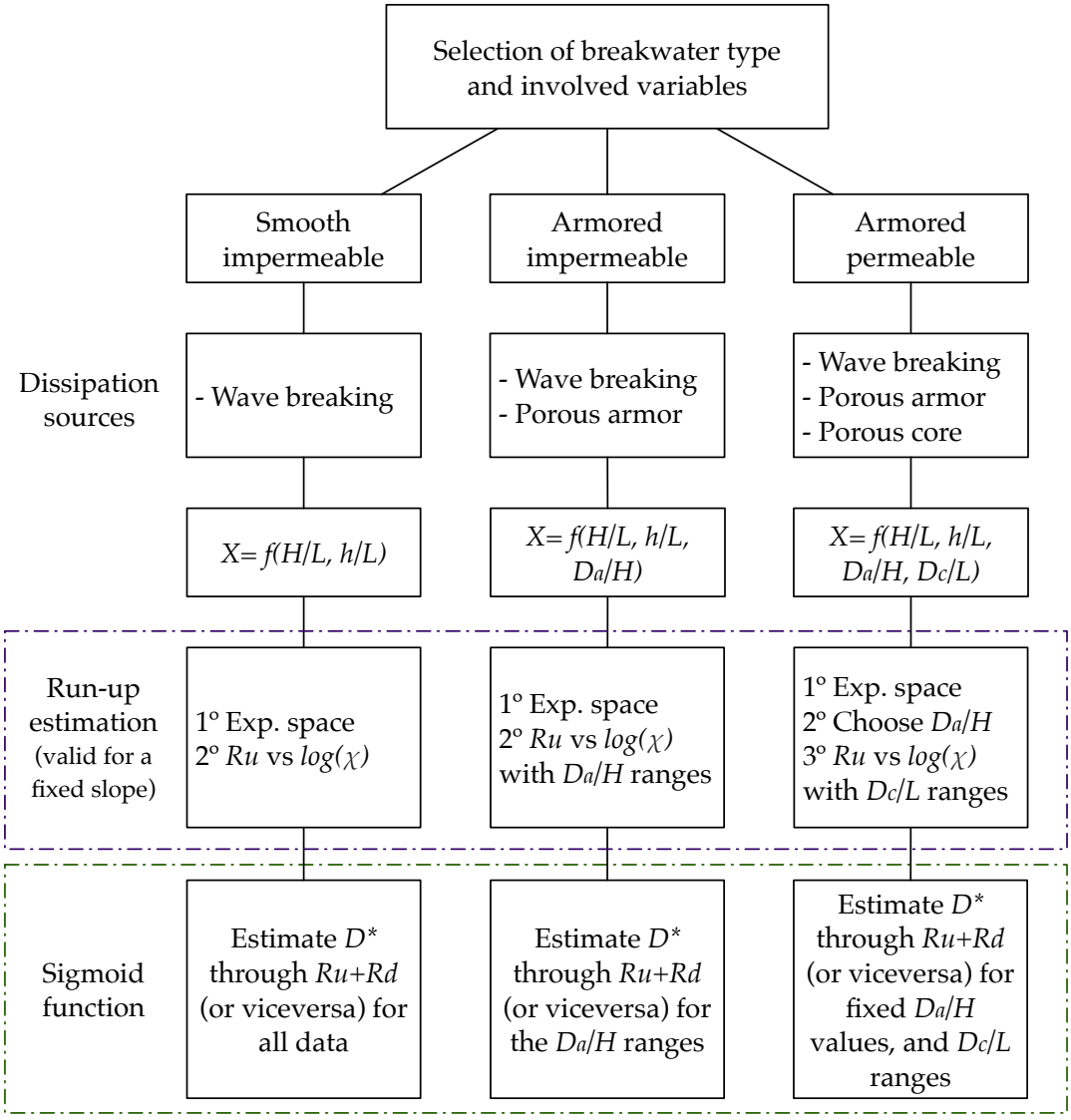


FIGURE 8.1: Sequence methodology for estimating run-up, run-down and energy transformation in different types of structures.

## 8.2 Future research lines

Based on the aforementioned conclusions, it is proposed to advance in the following lines of research:

1. The first proposed line is to analyze the six types of breakers on smooth impermeable slopes with different angles with respect to the bottom (1:2, 1:3, 1:20...) to see how the breakers move within the experimental space $log([H_I/L) - log(h/L)]$ and to see in which $\chi$ ranges the transitions occur.
2. To analyze through dimensional analysis the failure modes: loss of stability of the armor pieces and overtopping. These failure modes have in common that they are cumulative in time, so that time $t_0, t_1$ must be considered in the dimensional analysis. An adaptation of the current model of evolution fo damage (Castillo et al., 2012) could be proposed. This approach must be carried out with care and the final result should be a renewal of the formulas used today based on studies from years ago (Van Der Meer, 1988; Van Gent, 1995; EurOtop, 2018).
3. To add to the dimensional analysis other physical parameters of breakwaters such as the influence of a berm, crown wall or other geometries. These parameters are known to affect the flow characteristics but not analyzed through dimensional analysis. In this way the dimensionless variables that affect flow characteristics, stability or energy transformation will be more organized and easier to study.
4. To propose a working methodology and its specifications for the design of a breakwater section type following 1.1-18 (2018) requirements, including the optimization of total costs. Implement global methodologies for design, verification, and optimization of mound breakwaters, in the light of different damage levels and repair strategies taking into account the total costs of the infrastructure.

# Appendices

# A Overview of the experimental technique in the CIAO wave flume

The choice of slope, water depth, and target wave characteristics, height, $H$, and period, $T$, of the regular train generally depend on the dimensions of the wave flume and wavemaker. The vertical water surface displacement is recorded with an array of 4 gauges located along the channel. This set of data is used to separate the incident and the reflected wave trains. The experimental input thus consists of the actual values of the non-dimensional variables at the toe of a slope, namely, the relative water depth, $h/L$ , and incident wave steepness, $H_I/L$.

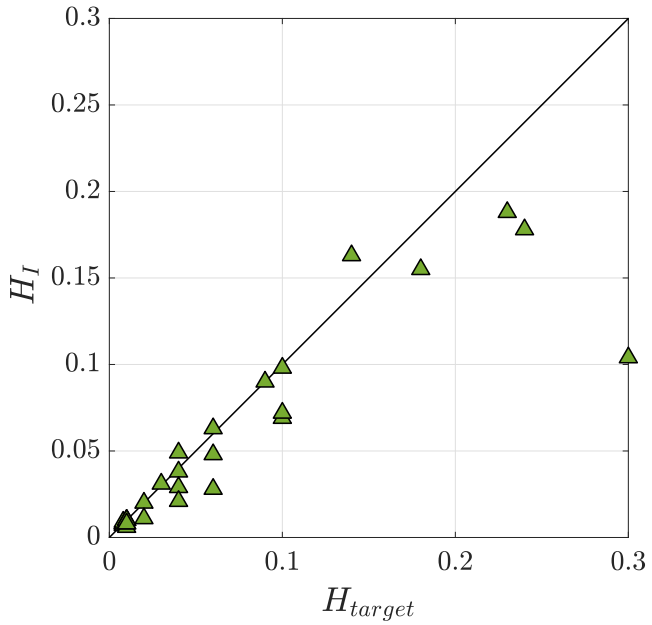


FIGURE A.1: Comparison between the target and measured values of the wave height in the CIAO wave flume.

The experiment is carried out by runs. The input of a run is the calculated pair of values, $h/L$ , $H_I/L$, and the output is the observation of one of the six wave breaker types. Each run is independent, and for an impermeable slope under a regular wave train, $h/L$, $H_I/L$, the observed breaker type is unique and repeatable. A run starts with the target signal to the wavemaker and the wave generation. Thus, there should be slight differences in the calculated values at the toe of the slope and the observed breaker type (Figure A.1).

A sequence of runs is defined by a varying $h/L$ and $H_I/L$. Each sequence provides a specific progression of wave breaker types. In this research, these include the following: (a) a constant $h/L$ and a varying $H_I/L$; (b) a constant $H_I/L$ and a varying $h/L$ ; (c) a linear or non-linear functional relationship between $h/L$ and $H_I/L$. Once a sequence is defined, then the expected progression of breaker types is predictable (Chapters 3 and 4).

## A.1 Wave propagation down the flume

Froudes law of similitude, applied as gravitational acceleration, is the dominant physical parameter. In some of the runs carried out in the wave flume, the effects of viscosity and surface tension can be significant. At a short distance from the wavemaker, the evanescent modes decay completely, and the generated wave train propagates down the flume between the vertical side walls with the direction parallel to the longitudinal axes of the channel. There are two characteristics of the fluid, surface tension and viscosity, and two of the flume geometry, width and surface roughness of the bottom and side walls, which can affect the wave train propagation and its expected characteristics at the toe of the slope. Viscosity is accounted for by the Reynolds number, and the surface tension by the Weber number.

### A.1.1 Surface tension and wave propagation down the flume

The surface tension, $\tau_s$, on the free surface yields a difference between atmospheric pressure and the water surface below. This effect is considered in the dynamic free surface boundary condition $(z = 0)$ of the boundary value problem of water waves through the dispersion relationship, $f(T, h, \tau_s) = 0$. The effect of the surface tension is to increase the wave length and the wave celerity for all the wave frequencies. Furthermore, the potential wave energy includes a term that evaluates the work done in extending a surface element against the surface tension, and the kinetic wave energy includes a term that evaluates the corresponding transport. The contribution of the surface tension to the total average wave energy per unit surface and to the wave celerity is given by the dimensionless quantity, $\epsilon_\tau = (\tau_s k^2)/(\rho_w g)$. According to Le Méhauté (1976), the capillary effects are negligible for wave propagation if still-water depths $h > 0.02m$ and wave periods $T > 0.35s$. For the tests run in the wave flume, the range of wave periods $[0.9 < T(s) < 4.0]$, water depth $h = 0.50m$ and $L > 1m$ , signifies that the value of $\epsilon_\tau$ is $O(10^{-6})$, and Weber number is $O(10^{-4})$. Indeed, surface tension is relevant for capillary waves, $T < 0.2s$, deep water wave number $k_0 > 2\pi$.

For deep and intermediate water depths, Barthelemy et al. (2018) proposed a breaking criterion based on the local incident energy flux velocity and introduced a breaking onset threshold parameter, later applied by Derakhti et al. (2020). Their research neglected surface tension effects, but they assessed the validity of this assumption at the crest point of a 2D wave with a wavelength of order $1m$. They concluded that for water waves in the laboraroty with shorter wavelengths, there is the potential for the proposed breaking onset threshold to be modified by the effects of surface tension. Therefore, for freshwater, the conclusion by Stagonas et al. (2011), that when waves shorter than $4m$ and smaller than $0.11m$ break under the weakened influence of surface tension, they dissipate up to 65% more wave energy is possibly optimistic, and the intervals of wave height and wave length should be significatively decreased. Thus, it can be assumed that wave generation and propagation down the CIAO wave flume are not affected by surface tension.

### A.1.2 Viscosity and wave decay down the flume

The bed and the lateral walls of the flume are built with glass, which is often used in labs because of its very low Nikuradse roughness value. It provides an reasonable slip boundary condition at the bottom and at the wall, namely $[\tau_{xz}(z = -h), \tau_{xy}(y \pm b)] \approx 0$. These shear stresses are almost negligible in the core of the irrotational flow. However, their gradients $\partial\tau_{xz}/\partial z$, $\partial\tau_{xy}/\partial y$, which are very close to the bed and to the walls, respectively cause of the development of the wave boundary layer. For a viscous fluid the equations governing the water waves are NS equations. Considering their linearized and dimensionless form, the two dimensionless quantities affecting the pressure gradient term and the viscous shear stress gradient are the Froude number, $F_r^2 = C^2\sqrt{k/g}$, and the Reynolds number, $R_e = \omega/(\nu k^2)$ respectively. The laminar WBL at the bed and at the walls occupied a very small region. The vertical length scale close to the bed is defined by the dimensionless number, $\omega/(\nu\delta^2)$, which becomes $O(1)$ if $\delta \sim \sqrt{\nu/\omega}$. For laminar WBL, $\delta \sim 1mm$.

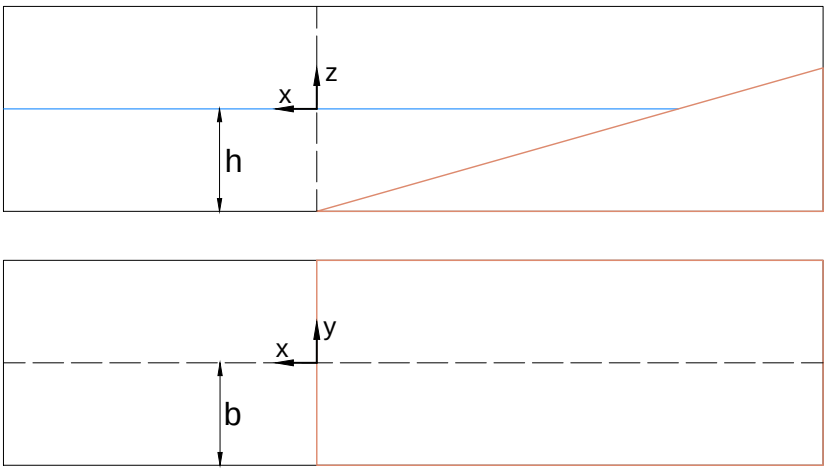


FIGURE A.2: Scheme of the CIAO wave flume (plan and elevation) with the position of the origins of the $x$, $y$ and $z$ directions.

For turbulent WBL, the vertical length at the bed and the horizontal length at the walls are larger than for laminar WBL. However, in any case for glass contours they occupy a very small part of the depth at the bottom and a small part of the width at the wall. A conventional form for the shear stress at the bed in an oscillatory flow propagating on constant depth is,

$$\tau_{xz} = \frac{1}{8}\rho_w f_b(u_b|u_b|) \quad \text{at } z = -h. \tag{A.1}$$

$$\tau_{xy} = \frac{1}{8}\rho_w f_w(U|U|) \quad \text{at } y \pm b. \tag{A.2}$$

where, $f_{(b,w)}$ are the friction factors; $u_b$ a representative velocity at the bottom; and $U$ the depth-averaged horizontal velocity at the lateral walls. At the bottom the potential velocity is $u_b = \zeta_b\omega$, and $R_e = u_b\zeta_b/\nu$. The friction factors depend on a Reynolds number, $R_e = Uh/\nu$ and a relative roughness, $\zeta_b/k_e$ (Kamphuis, 1975)

where $k_e$ is the equivalent sand grain size of the bed. The generated waves propagating down the flume, $10^5 < Re < 10^7$ and $\zeta_b/k_e > 2800$ are in the transition and smooth turbulent regime, $5x10^{-3} \lesssim f_{(b,w)} \lesssim 10^{-2}$.

For the turbulent wave boundary layer (Dean and Dalrymple, 1991), the mean rate of energy dissipation per unit time and unit width is $\varepsilon_{D,b} = 1/T \int_t^{t+T} \tau_{xz} u_b dt$. Similarly, the mean rate of energy dissipation per unit time and per unit water depth at the side walls is $\varepsilon_{D,w} = 1/T \int_t^{t+T} \tau_{xy} U dt$. Solving the energy conservation equation (Equation A.3) and using as an initial condition the flux of energy at the wavemaker, the total mean rate of energy dissipation per unit time and wetted perimeter, (bed plus side walls, $2b + 2h$) are obtained.

$$\frac{d}{dx}\left(2b \cdot EC_g\right) + 2b \cdot \varepsilon_{D,b} + 2h \cdot \varepsilon_{D,w} = 0 \tag{A.3}$$

The wave decay, $H(x)/H_p$, along the flume depends on the wave steepness at the wavemaker, the relative water depth, the relative distance $x/L$ to the paddle, the friction coefficient and the width $2b$ of the channel. Furthermore, $x$ is the distance to the wavemaker, and $H_p$ is the wave generated by the paddle. Figure A.3 shows that for $x/L < 10$, the wave decay for all the runs is $O(10^{-4})$. Although the mean rate of energy dissipation at the vertical walls is different than at the bed, the magnitude of decay and the symmetry support the assumption that the wave crest propagates down the flume perpendicular to the central axes of the channel.

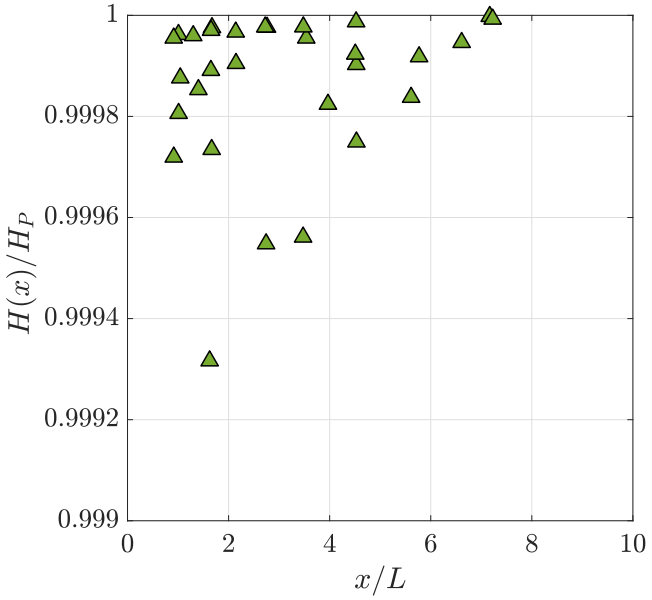


FIGURE A.3: Wave height decay along the flume, $H(x)/H_p$, plotted against the relative distance to the wavemaker $x/L$. $H_p$ is the wave generated by the paddle, recorded close to the wavemaker, but far enough away so as not to be affected by the evanescent modes.

### A.1.3 Standing transversal oscillations

The boundary value problem of the wave propagating down the flume can be completely solved with the appropriated boundary condition (BC) at the surface

and the no-flow boundary conditions at the bottom and vertical walls (Losada et al., 1994). The inclusion of the Fourier terms $cos(m\lambda y)$ for the velocity potential insures no flow through the channel walls, provided that $\lambda = \pi/b$. The wave field downstream consists of the wavemaker-generated incident plane wave propagating down the flume and the reflected plane waves, which are independent of the $y$ coordinate $(m = 0)$ plus the progressive and evanescent standing waves travelling in the direction from the $x$ direction. The progressive standing wave modes, $m\lambda < k_n$ consist of two intersecting wave trains travelling at an angle $\theta$ to the x-axis (Equation A.4).

$$\theta = \frac{1}{k_n} \cos^{-1} \sqrt{k_n^2 - (m\lambda)^2} \tag{A.4}$$

For the experimental runs carried out in the CIAO wave flume, the depth is $h = 0.50m$, width $2b = 1m$ and $\lambda = 2\pi$. The theoretical progressive standing wave modes (based only on the most progressive wave mode $n = 0$), occur when $\sqrt{k_0^2 - (m\lambda)^2}$ is a positive real number. This condition can only occur for the shortest wave period, for $m = 1$, $L \leq 1m$ and $k_0 \geq \lambda$. To have an intersecting wave train travelling at an angle $\theta$ toward the x-axis, $T \leq 0.8s$. For the interval of wave periods tested, $[0.95 < T(s) < 4.6]$. Thus, it can be assumed that the wave crests impinged the toe of the slope perpendicular to the centerline of the wave flume.

## A.2 Wave propagating on the slope

Once the wave train propagates over the slope, the crest velocity, which is larger than the phase velocity is likely to be relevant to breaking waves in the surf zone (Peregrine, 1983). Kemp (1960) pointed out that the total phase difference across the surf zone is indicative of the type of wave motion. Battjes (1974) proposed that the reflection coefficient depends on the surf similarity parameter, $Ir$. His Figure 2 shows that the relationship deteriorates rapidly as $Ir > 1.2$. Dissipation is the principal signature of the breaking process for very small values of $Ir \leq 0.1$. The local conservation of wave energy equation over the slope is a balance between the incoming wave energy flux and dissipation by wave breaking (neglecting dissipation on the bed).

Conversely, in the intermediate and reflective regimes, $Ir > 1.2$ the importance of the reflection process on the slope and thus on the breaking process and breaker type, cannot be ignored. Laboratory experiments by Iribarren and Nogales (1949) and Miche (1951) showed that collapsing breaker corresponds to a regime about halfway between complete reflection and complete breaking. Bruun and Johannesson (1977) interpreted this type of breaking as a quasi-resonant oscillation on the slope. Thus, the local conservation of wave energy equation over the slope is a balance between the incoming wave energy flux, reflective energy flux, and the dissipation by breaking (ignoring again the dissipation on the bed), (Baquerizo et al., 1997). Now the problem is no longer parabolic, but rather elliptic (or hyperbolic) and BCs at the coastline and at the toe of the slope (or deep water) must be prescribed (Baquerizo et al., 1998).

On the other hand, the breaking process on the slope is quite different than that at a deep and intermediate depth (Barthelemy et al., 2018). Their experimental layout does not change the relative water depth in the domain, and the BC on the landward

side of the domain does not reflect wave energy. Their work is based on McLean et al. (1981), who found that Benjamin and Feir (1967) instability and Longuet-Higgins (1978) instability are two special cases of their three-dimensional instability theory, a theory validated by laboratory experiments (Melville, 1982). Note that the breaking onset threshold criterion proposed by Barthelemy et al. (2018) is based on the progressive (incident) energy flux considerations, and the initial breaking instability occurs within a very compact region centered on the wave crest.

### A.2.1 Surface tension and viscosity on the slope

Battjes (1974) analyzed the phase difference across the surf zone (plane impermeable slope), and following Kemp (1960) suggested that the dimensionless distance, $l_b/L_b$ of the breakpoint (breaking onset) from the mean water line is indicative of type of wave motion; $l_b = h_b \cot\alpha$, and $L_b$ is the wavelength at breaking, except for spilling breakers and perhaps weak plunging, $l_b/L_b \leq 1$. Based on the results obtained for waves down the flume, it can be assumed that the decay of wave height from the toe of the slope to the breakpoint is negligible. It is unlikely that once the wave crest velocity speeds up, the wave crest bends because of bed-wall dissipation or the effect of surface tension.

After the onset of breaking and the full development of the breaker type, the wave front velocities evolve along the slope during the run-up and run-down (Zhang and Liu, 2008). The Reynolds and Weber numbers decay significantly. Regarding the run-up and overland flow for solitary waves, Fuchs and Hager (2012) concluded that no scale effects were expected for water depth in excess of $0.08m$, minimum overland flow Reynolds number, $R_f \geq 6300$, and overland flow Weber number, $W_f \geq 10$ (Equations A.5 and A.6) where $u_f$ is the flow front velocity, and $d_{max}$ is the maximum flow depth.

$$R_f = \frac{u_f d_{max}}{\nu} \tag{A.5}$$

$$W_f = \frac{u_f}{\sqrt{\frac{\tau_s}{\rho d_{max}}}} \tag{A.6}$$

Although their numerical study ignores the surface tension effects, Wei et al. (2018) concluded that the process of wave breaking in deep and intermediate water depth is sensitive to initial velocity perturbations and like many other dynamic processes in nature, exhibits a chaotic behavior. Some of the perturbations could be the pre-existing turbulence or currents and wave reflection. They underline the fact that wave breaking is a deterministic process, and the breaking only occurs when certain criteria are met. Their results show that there are various properties of the breaking process which are reproducible. Our results indicate that breaker types on an impermeable plane slope under regular waves are reproducible, although there are some perturbations because of wave reflection, edge wave generation, and associated nearshore circulation. However, no scale effects because of surface tension and viscosity are expected.

### A.2.2 Edge wave generation and wave breaker types

Bowen and Inman (1969) showed that incident waves generate standing edge waves on a beach of the same frequency as the incoming waves. Rip currents were found to occur at alternate antinodes of the edge waves. The spacing of the rip current was therefore equal to the longshore wavelength of the edge waves. Guza and Inman (1975) showed that one type of beach cusp is linked to incident waves that are surging and mostly reflected. The spacings of some cusps under reflective wave conditions in the laboratory and in the field are consistent with the formation by either subharmonic edge waves of zero-mode number (period twice that of incident waves) or synchronous edge waves of low mode (period equal to that of incident waves). Subharmonic edge wave generation occurs under strongly reflected incident waves. Synchronous edge wave generation can also occur under reflective slopes but its resonance is weaker.

Baquerizo et al. (2002) showed that the presence of the shelf produces a curvature and a cut-off of the dispersion curves, which restricts the possible modes and lowers the frequencies for the longest waves of each mode. The presence of the slope moves off the curves from the vertical lines that correspond to Eckart's solution. This increases the frequency for the shortest waves of each mode and decreases it for the smaller wave numbers.

Kaneko (1985) observed the formation process of beach cusps in the laboratory. Most of the observational spacings agree well with half a wavelength of the zero mode subharmonic edge wave excited on the beach. Furthermore, he suggested that for a given slope there is a critical value of the wave steepness value lower than which subharmonic edge waves might be replaced by synchronous edge waves. The wave length of subharmonic and of synchronous edge waves, can be estimated by the Equations A.7 and A.8.

$$L_c = \frac{L}{2} = gT^2 \frac{\sin \alpha}{\pi} \quad \text{for subharmonic type} \tag{A.7}$$

$$L_c = L = gT^2 \frac{\sin \alpha}{2\pi} \quad \text{for synchronous type} \tag{A.8}$$

where $T$ is the incident wave period, and $\alpha$ is the slope. The development of one of the edge wave type will be favoured when $L_c \approx 2b$, where $2b$ is the width of the flume. The synchronous edge wave length $L_c$ for tests 1 (WB), 6 (SPl), 10 (SB), 12(SPl), 21 (WB) and 26 (SB) is close to 1 m, and for test 9 (WB) close to 2 m. Only test 1 shows the features of the across-slope undulation of the crest and convergence of the up-rush and down-rush flows amid the channel width. The other tests show an incoming, incipient curved crest though the observed up-rush and down-rush fronts are nearly straight. This distinctive behavior can be attributed to the local high friction of the down-rush thin layer of the previous wave with the rubber that seals the joint of the bottom and side wall glasses, (tests WB) 9 and 21. In addition, their wave steepness at the toe of the slope is very small, 0.0013. Tests 6 and 12 are SPl breakers, a type that does not match the predominant mechanisms of synchronous edge wave generation.

On the other hand the subharmonic edge wave length of the tests 2, 14, and 28 are nearly equal to the flume width. From the photograph it is impossible to detect

if the crest is not straight or whether it is rotating as a rigid solid on a vertical axis. For that purpose, and this is an important conclusion, it would be convenient to use transversal arrays of gauges that do not perturb the flow (acoustic or similar).

# B Photographs of the different breaker types

As mentioned previously in Chapter 2, Galvin (1968) identified and quantified nine breaker types on a plane impermeable slope. Galvins classification includes the following types: (1) spilling, (2) plunging, (3) collapsing, and (4) surging. The description of each wave type is represented in Figure B.1. The critical values of the Iribarren number for each type of breaking are shown in the Table B.1.

TABLE B.1: Values of the Iribarren number for each breaker type.

| | | |
|---|---|---|
| Surging or collapsing | if | $3.3 < Ir$ |
| Plunging | if | $0.5 < Ir < 3.3$ |
| Spilling | if | $Ir < 0.5$ |

This Appendix presents additional photographies for the six types of breaking defined in Chapter 2, highlighting the specific characteristics of each type of breaking. Each breaker type was studied in a smooth impermeable 1:10 slope. And it is important to remember, as previously demonstrated, that the Iribarren number does not characterize the six new types of breaking since the relative depth must be taken into account. Thats why the alternate similarity parameter was proposed, valid for each slope angle.

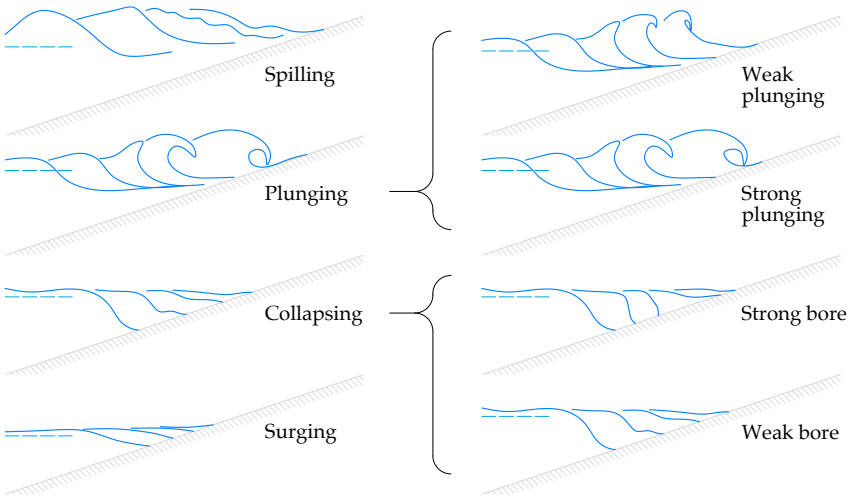


FIGURE B.1: Differences in the time progression of the water surface for the wave breaker types identified by Galvin (1968): spilling, plunging, collapsing and surging; and the new identified breaker types: weak and strong plunging, and weak and strong bore.

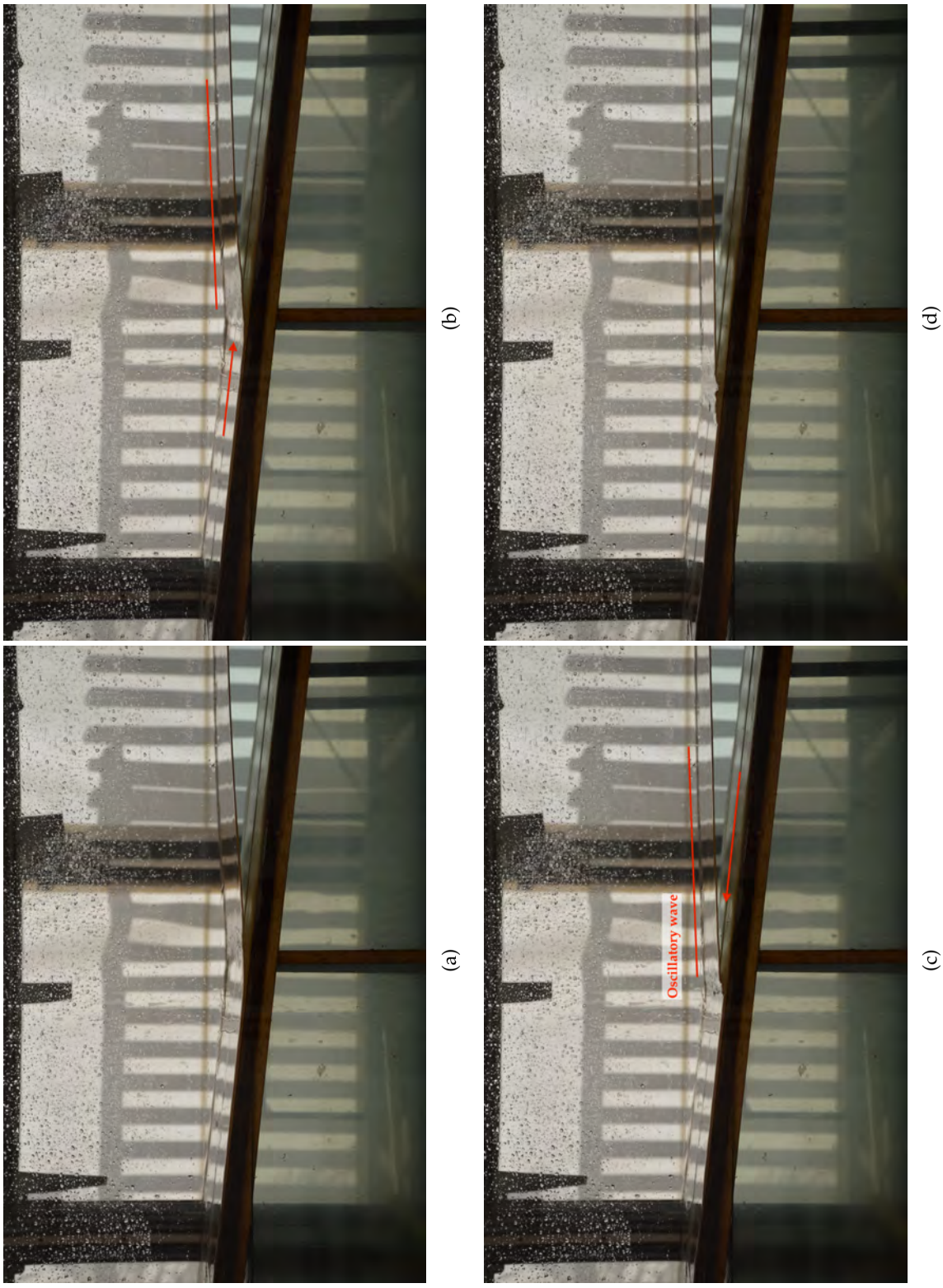


FIGURE B.2: Photographs of the progression of a surging breaker type.

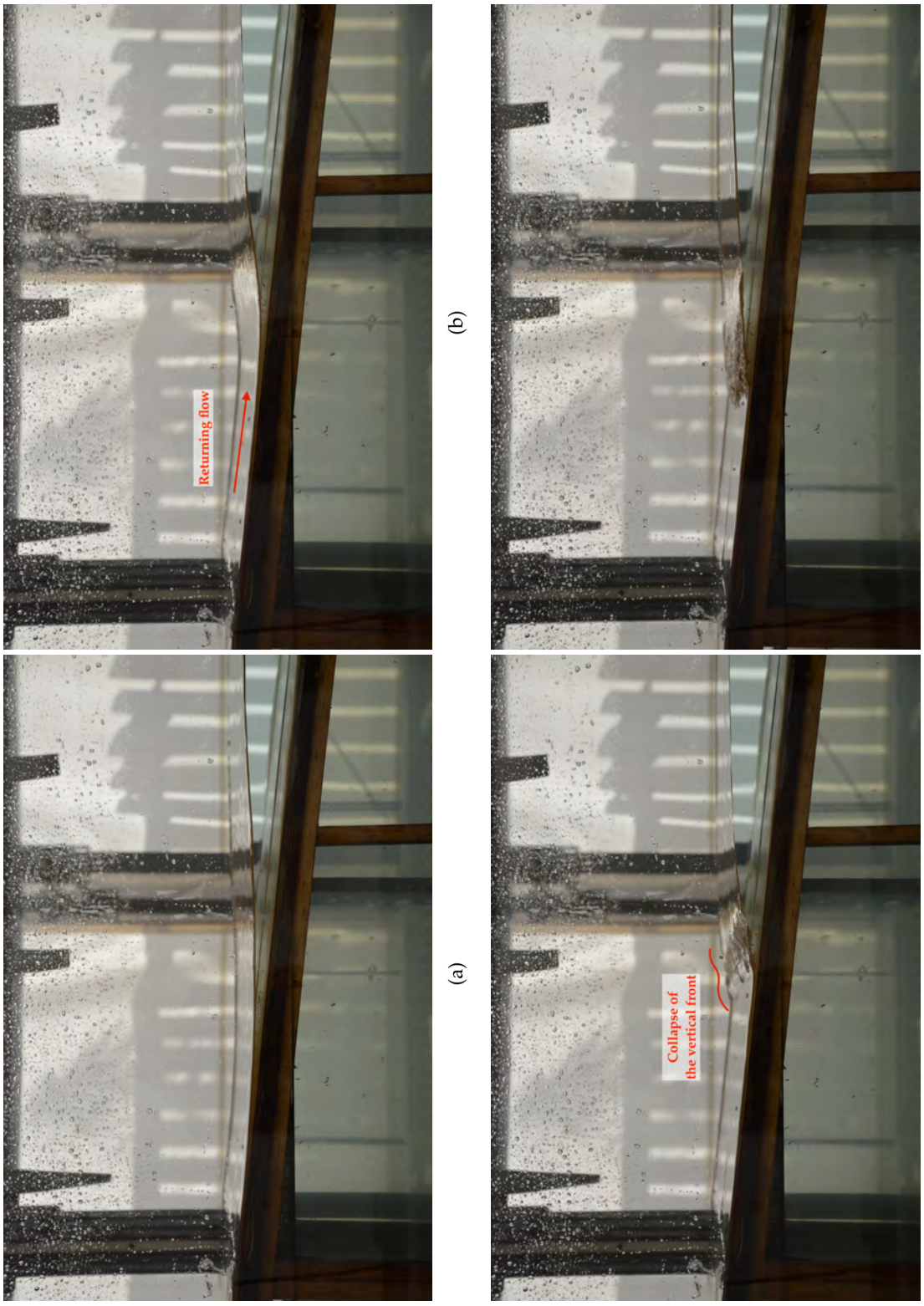


FIGURE B.3: Photographs of the progression of a weak bore breaker type.

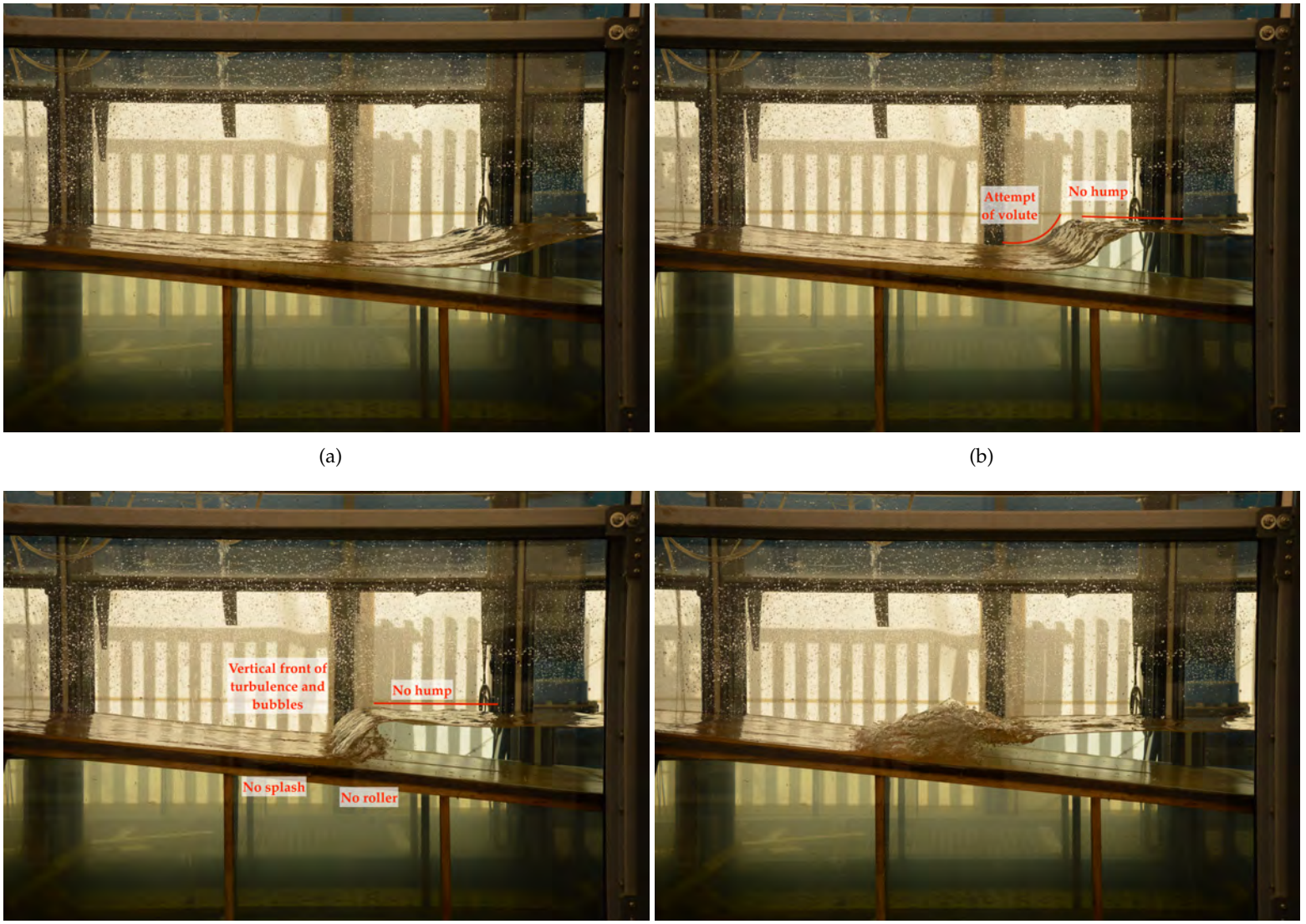


(a) (b)

(c) (d)

FIGURE B.4: Photographs of the progression of a strong bore breaker type.


FIGURE B.5: Photographs of the progression of a strong plunging breaker type.

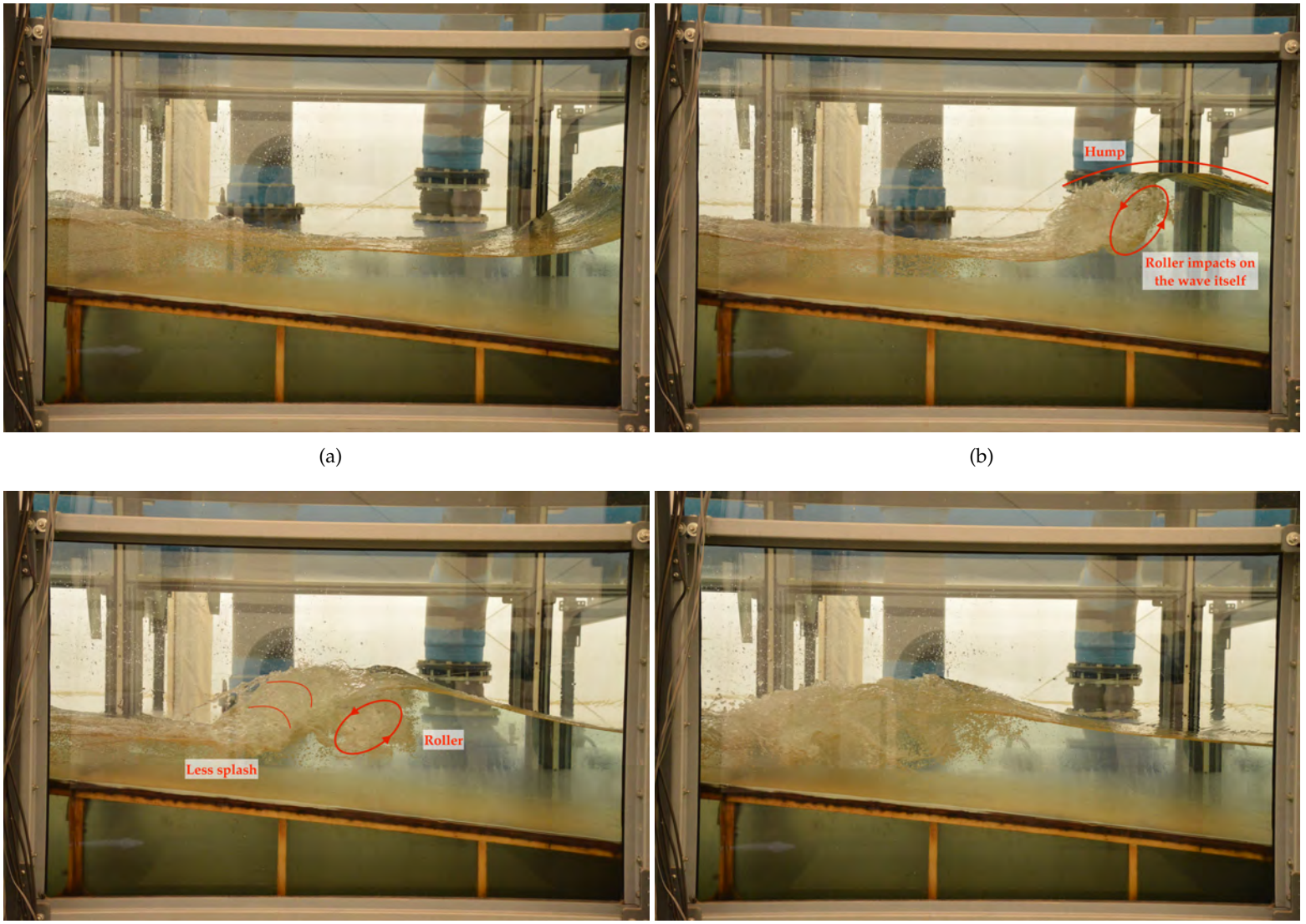


(a) (b)

(c) (d)

FIGURE B.6: Photographs of the progression of a weak plunging breaker type.

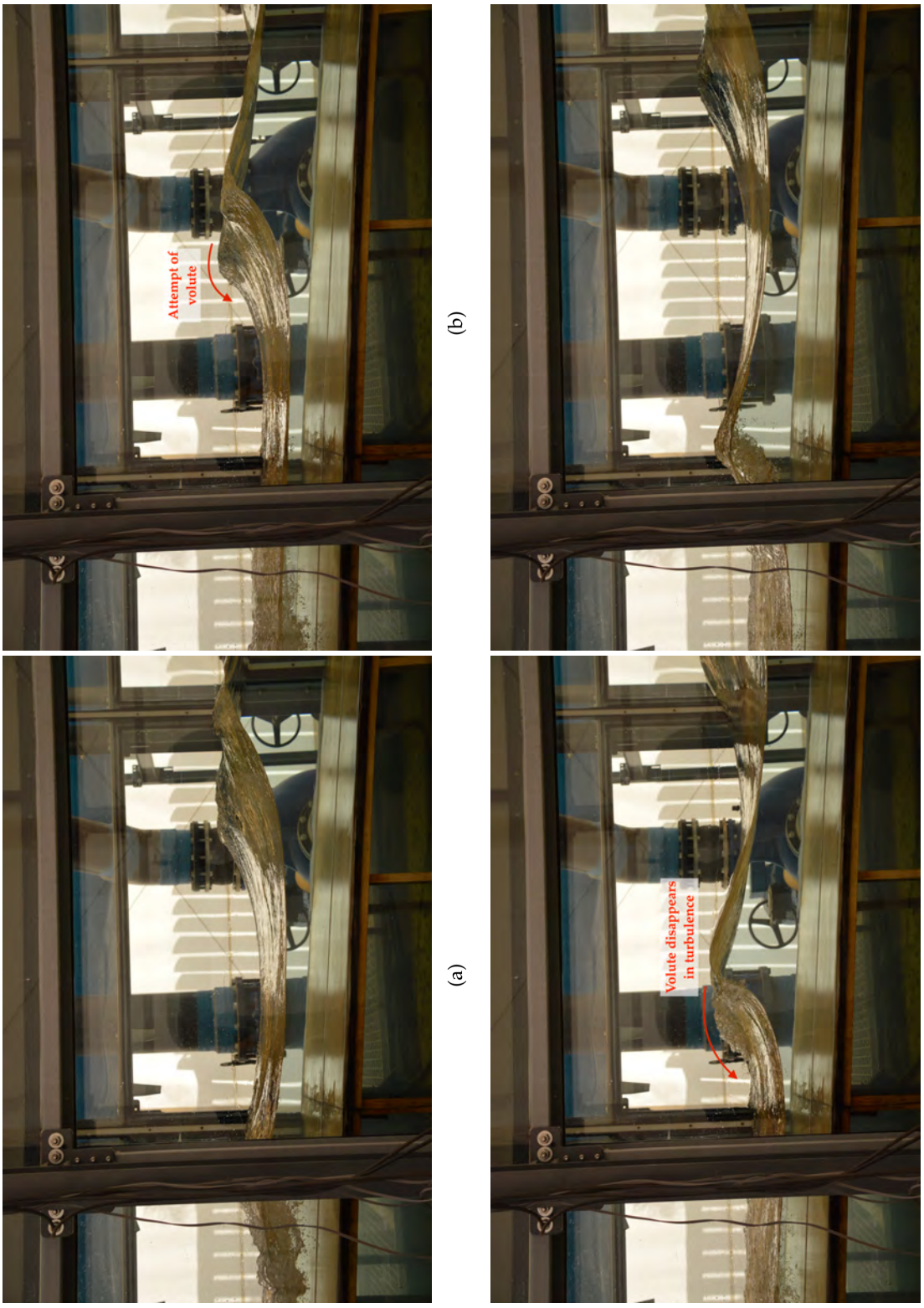


FIGURE B.7: Photographs of the progression of a spilling breaker type.

# Bibliography


0.0-01, R. (2001). *ROM 0.0 Description and Characterization of Project Factors of Maritime Structures*. Puertos del Estado.

1.1-18, R. (2018). *ROM 1.1. Recommendations for Breakwater Construction Projects.* Puertos del Estado.

Addona, F., Loarca, A. L., Chiapponi, L., Losada, M. A., and Longo, S. (2018). "The Reynolds wave shear stress in partially reflected waves." In: *Coastal Engineering* 138, 220 –226.

Agrawal, Y. C., Terray, E. A., Donelan, M. A., Hwang, P. A., Williams, A. J., Drennan, W. M., Kahma, K. K., and Krtaigorodskii, S. A. (Sept. 1, 1992). "Enhanced dissipation of kinetic energy beneath surface waves." In: *Nature* 359.6392, 219–220.

Ahrens, J. P. and McCartney, B. L. (1975). *Wave period effect on the stability of riprap*. Coastal Engineering Research Center Fort Belvoir VA.

Ahrens, J. P. and Titus, M. F. (1985). "Wave Runup Formulas for Smooth Slopes." In: *Journal of Waterway, Port, Coastal, and Ocean Engineering* 111.1, 128–133.

Ahrens, J. P., Seelig, W. N., Ward, D. L., and Allsop, N. (1993). "Wave runup on and wave reflection from coastal structures." In: *Ocean Wave Measurement and Analysis*. ASCE, pp. 489–502.

Ahrens, J. (1981). *Irregular Wave Run-Up on Smooth Slopes.* 81-17. Vicksburg: Coastal Engineering Research Center, Waterways experiment station.

Airy, G. B. (1845). *Tides and waves*. Vol. 5. B. Fellowes.

Allsop, W., Hawkes, P., Jackson, F., and Franco, L. (1985). *Wave run-up on steep slopes - model tests under random waves*. Hydraulics Research Wallingford.

Almar, R., Blenkinsopp, C., Almeida, L. P., Catalán, P. A., Bergsma, E., Cienfuegos, R., and Viet, N. T. (2019). "A new remote predictor of wave reflection based on runup asymmetry." In: *Estuarine, Coastal and Shelf Science* 217, 1–8.

Andersen, T. L., Clavero, M., Frigaard, P., Losada, M., and Puyol, J. I. (2016). "A new active absorption system and its performance to linear and non-linear waves." In: *Coastal Engineering* 114, 47 –60.

Arana, A. M. H. (2017). "Wave run-up on beaches and coastal structures." PhD thesis. University College London.

Babanin, A. (2009). "Breaking of ocean surface waves." In: *Acta Physica Slovaca. Reviews and Tutorials* 59.4, 305–535.

Babanin, A. (2011). *Breaking and dissipation of ocean surface waves*. Cambridge University Press.

Bagnold, R. A. and Taylor, G. I. (1946). "Motion of waves in shallow water. Interaction between waves and sand bottoms." In: *Proceedings of the Royal Society of London. Series A. Mathematical and Physical Sciences* 187.1008, 1–18.

Baquerizo, A., Losada, M. A., and Smith, J. M. (1998). "Wave reflection from beaches: A predictive model." In: *Journal of Coastal Research*, 291–298.

Baquerizo, A., Losada, M. A., and Losada, I. J. (2002). "Edge wave scattering by a coastal structure." In: *Fluid Dynamics Research* 31.4, 275 –287.

Baquerizo, A., Losada, M. A., Smith, J. M., and Kobayashi, N. (1997). "Cross-Shore Variation of Wave Reflection from Beaches." In: *Journal of Waterway, Port, Coastal, and Ocean Engineering* 123.5, 274–279.

Baquerizo, A. (1995). "Reflexión del oleaje en playas: Métodos de evaluación y de predicción." PhD thesis. Universidad de Cantabria.

Baquerizo, A. and Losada, M. A. (2008). "Human interaction with large scale coastal morphological evolution. An assessment of the uncertainty." In: *Coastal Engineering* 55.7, 569 –580.

Barthelemy, X., Banner, M. L., Peirson, W. L., Fedele, F., Allis, M., and Dias, F. (2018). "On a unified breaking onset threshold for gravity waves in deep and intermediate depth water." In: *Journal of Fluid Mechanics* 841, 463–488.

Battjes, J. A. (1974). "Surf similarity." In: *Coastal Engineering*, 466–480.

Bayle, P. M., Blenkinsopp, C. E., Conley, D., Masselink, G., Beuzen, T., and Almar, R. (2020). "Performance of a dynamic cobble berm revetment for coastal protection, under increasing water level." In: *Coastal Engineering* 159, 103712.

Benedicto, M. I. (2004). "Comportamiento y evolución de la avería de los diques de abrigo frente a la acción del oleaje." PhD thesis. Universidad de Granada.

Benjamin, T. B. and Feir, J. E. (1967). "The disintegration of wave trains on deep water Part 1. Theory." In: *Journal of Fluid Mechanics* 27.3, 417–430.

Bowen, A. J. and Inman, D. L. (1969). "Rip currents: 2. Laboratory and field observations." In: *Journal of Geophysical Research (1896-1977)* 74.23, 5479–5490.

Broekhoven, P. J. M. van (2011). "The influence of armour layer and core permeability on the wave run-up." PhD thesis. Delft: Delft University of Technology.

Bruun, P. and Johannesson, P. (1977). "Parameters affecting stability of rubble mounds, Closure. ASCE." In: *Jour. of Waterway, Port and Coastal Ocean Div., WW4*, 533–566.

Bruun, P. and Günbak, A. R. (1977a). "New design principles for rubble mound structures." In: *Coastal Engineering 1976*, pp. 2429–2473.

– (1977b). "Stability of sloping structures in relation to risk criteria in design." In: *Coastal Engineering* 1, 287 –322.

Buccino, M., DAnna, M., and Calabrese, M. (2018). "A study of wave reflection based on the maximum wave momentum flux approach." In: *Coastal Engineering Journal* 60.1, 1–21.

Buckingham, E. (1914). "On physically similar systems. Illustrations of the use of dimensional equations." In: *Physical review* 4.4, 345.

Burcharth, H. F. and Andersen, O. K. (1995). "On the one-dimensional steady and unsteady porous flow equations." In: *Coastal Engineering* 24.3, 233 –257.

Burcharth, H. F. and Lykke Andersen, T (2009). "Scale effects related to small scale physical modelling of overtopping of rubble mound breakwaters." In: *Coastal Structures 2007: (In 2 Volumes)*. World Scientific, pp. 1532–1541.

Burcharth, H. F., Andersen, T. L., and Medina, J. R. (2010). "Stability of Cubipod armoured roundheads in short crested waves." In: *Proceedings of the 32nd International Conference on Coastal Engineering*. International Conference of Coastal Engineering. ASCE.

Capel, A. (2015). "Wave run-up and overtopping reduction by block revetments with enhanced roughness." In: *Coastal Engineering* 104, 76 –92.

Castillo, C., Castillo, E., Fernández-Canteli, A., Molina, R., and Gómez, R. (2012). "Stochastic Model for Damage Accumulation in Rubble-Mound Breakwaters Based on Compatibility Conditions and the Central Limit Theorem." In: *Journal of Waterway, Port, Coastal, and Ocean Engineering* 138.6, 451–463.

Christensen, E. D. and Deigaard, R. (2001). "Large eddy simulation of breaking waves." In: *Coastal engineering* 42.1, 53–86.

Churchill, S. W. and Usagi, R. (1972). "A general expression for the correlation of rates of transfer and other phenomena." In: *AIChE Journal* 18.6, 1121–1128.

Clavero, M., Díaz-Carrasco, P., and Losada, M. (2020). "Bulk wave dissipation in the armor layer of slope rock and cube armored breakwaters." In: *Journal of Marine Science and Engineering* 8.3.

Clavero, M. (2007). "Comportamiento de los diques en talud frente a la acción del oleaje y criterios para el reparto de la probabilidad conjunta de fallo en la vida útil." PhD thesis. Universidad de Granada.

Clavero, M., Vílchez, M., Pérez, D., Benedicto, M. I., and Losada, M. A. (2012). "An unified design method of maritime works against waves." In: *Coastal Engineering Proceedings* 1.33, structures.76.

Dalrymple, R. A., Losada, M. A., and Martin, P. A. (1991). "Reflection and transmission from porous structures under oblique wave attack." In: *Journal of Fluid Mechanics* 224, 625–644.

De Rouck, J, Boone, C, and Walle, B Van de (2001). "The optimisation of crest level design of sloping coastal structures through prototype monitoring and modelling, final report." In: *Ghent University report MAS03/1031*. Publisher: Ghent University.

Dean, R. G. and Dalrymple, R. A. (1991). *Water wave mechanics for engineers and scientists*. Vol. 2. World Scientific Publishing Company.

Del-Rosal-Salido, J., Folgueras, P., Ortega-Sánchez, M., and Losada, M.. (2019). "Beyond flood probability assessment: An integrated approach for characterizing extreme water levels along transitional environments." In: *Coastal Engineering* 152, 103512.

Derakhti, M., Kirby, J. T., Banner, M. L., Grilli, S. T., and Thomson, J. (2020). "A Unified Breaking Onset Criterion for Surface Gravity Water Waves in Arbitrary Depth." In: *Journal of Geophysical Research: Oceans* 125.7, e2019JC015886.

Duncan, J. H. (1981). "An experimental investigation of breaking waves produced by a towed hydrofoil." In: *Proceedings of the Royal Society of London. A. Mathematical and Physical Sciences* 377.1770, 331–348.

Díaz-Carrasco, P, Moragues, M., Clavero, M, Ortega-Sánchez, M, and Losada, M. (2017). "Wave Overtopping on mixed breakwaters and design curves." In: *Proceedings of the 8th International Short Course/Conference on Applied Coastal Research.* Santander, Spain.

Díaz-Carrasco, P. (2020). "Water-wave interaction with mound breakwaters: from the seabed to the armor layer." PhD thesis. Universidad de Granada.

Díaz-Carrasco, P., Moragues, M. V., Clavero, M., and Losada, M.. (2020). "2D water-wave interaction with permeable and impermeable slopes: Dimensional analysis and experimental overview." In: *Coastal Engineering* 158, 103682.

EurOtop (2018). *Manual on wave overtopping of sea defences and related structures. An overtopping manual largely based on European research, but for worldwide application.*

Folgueras, P., Del-Rosal-Salido, J., Moragues, M., Lopez, J., and Losada, M. (2018). "Accumulated damage evolution and investment costs of breakwaters." In: *Coastal Engineering Proceedings* 1.36.

Formentin, S. M. and Zanuttigh, B. (2018). "A new method to estimate the overtopping and overflow discharge at over-washed and breached dikes." In: *Coastal Engineering* 140, 240–256.

Fuchs, H. and Hager, W. H. (2012). "Scale Effects of Impulse Wave Run-Up and Run-Over." In: *Journal of Waterway, Port, Coastal, and Ocean Engineering* 138.4, 303–311.

Galvin, C. J. (1968). "Breaker type classification on three laboratory beaches." In: *Journal of geophysical research* 73.12, 3651–3659.

Giridhar, G. and Reddy, M. G. M. (2015). "Hydrodynamic Study of Energy Dissipation Blocks on Reduction of Wave Run-up and Wave Reflection." In: *Aquatic Procedia* 4, 281–286.

Gislason, K., Fredsøe, J., Deigaard, R., and Sumer, B. M. (2009). "Flow under standing waves: Part 1. Shear stress distribution, energy flux and steady streaming." In: *Coastal engineering* 56.3, 341–362.

Goda, Y. and Suzuki, Y. (1976). "Estimation of incident and reflected waves in random wave experiments." In: *Procceedings of the Fifteenth International Conference on Coastal Engineering*. 15th International Conference on Coastal Engineering. Honolulu, Hawaii, USA, pp. 828–845.

Grilli, A. R., Westcott, G., Grilli, S. T., Spaulding, M. L., Shi, F., and Kirby, J. T. (Sept. 1, 2020). "Assessing coastal hazard from extreme storms with a phase resolving wave model: Case study of Narragansett, RI, USA." In: *Coastal Engineering* 160, 103735.

Gu, Z. and Wang, H. (1991). "Gravity waves over porous bottoms." In: *Coastal engineering* 15.5, 497–524.

Guanche, R., Iturrioz, A., and Losada, I. J. (2015). "Hybrid modeling of pore pressure damping in rubble mound breakwaters." In: *Coastal Engineering* 99, 82–95.

Guza, R. T. and Inman, D. L. (1975). "Edge waves and beach cusps." In: *Journal of Geophysical Research* 80.21, 2997–3012.

Guza, R., Thornton, E., and Holman, R. (1985). "Swash on steep and shallow beaches." In: *Proceedings of the 19th International Conference on Coastal Engineering*. 19th International Conference on Coastal Engineering. Houston (USA), pp. 708–723.

Gómez-Martín, M. E. and Medina, J. R. (2014). "Heterogeneous Packing and Hydraulic Stability of Cube and Cubipod Armor Units." In: *Journal of Waterway, Port, Coastal, and Ocean Engineering* 140.1, 100–108.

Hsu, T.-W., Liang, S.-J., Young, B.-D., and Ou, S.-H. (2012). "Nonlinear run-ups of regular waves on sloping structures." In: *Natural Hazards and Earth System Sciences* 12.12, 3811–3820.

Hudson, R. Y. (1959). "Laboratory investigation of rubble-mound breakwaters." In: *Journal of Waterway, Port, Coastal and Ocean Division* 85.3, 93–122.

Hughes, S. A. (1993). "Laboratory wave reflection analysis using co-located gages." In: *Coastal Engineering* 20.3, 223–247.

– (2004). "Estimation of wave run-up on smooth, impermeable slopes using the wave momentum flux parameter." In: *Coastal Engineering* 51.11, 1085–1104.

Hunt, I. A. (1959). "Design of seawalls and breakwaters." In: *Journal of the Waterways and Harbors Division* 85.3, 123–152.

Iafrati, A. (2011). "Energy dissipation mechanisms in wave breaking processes: Spilling and highly aerated plunging breaking events." In: *Journal of Geophysical Research: Oceans* 116 (C07024).

IPPC (2019). *Climate Change and Land: an IPCC special report on climate change, desertification, land degradation, sustainable land management, food security, and greenhouse gas fluxes in terrestrial ecosystems [P.R. Shukla, J. Skea, E. Calvo Buendia, V. Masson-Delmotte, H.-O. Pörtner, D. C. Roberts, P. Zhai, R. Slade, S. Connors, R. van Diemen, M. Ferrat, E. Haughey, S. Luz, S. Neogi, M. Pathak, J. Petzold, J. Portugal Pereira, P. Vyas, E. Huntley, K. Kissick, M. Belkacemi, J. Malley, (eds.)].*

Iribarren, C. R. and Nogales, C. (1949). "Protection des ports." In: *XVII, International Navigation Congress, Section II, Comm* 4, 27–47.

Iversen, H. W. (1952). "Laboratory study of breakers." In: *Gravity Waves, Circular* 52, 9–32.

Jonsson, I. G. (1966). "Wave boundary layers and friction factors." In: *Proc., 10th International Conference on Coastal Engineering*. International Conference on Coastal Engineering. Tokyo, pp. 127–148.

Kamphuis, J. W. (1975). "Friction factor under oscillatory waves." In: *Journal of the Waterways, Harbors and Coastal Engineering Division* 101.2, 135–144.

Kaneko, A. (1985). "Formation of beach cusps in a wave tank." In: *Coastal Engineering* 9.1, 81 –98.

Kemp, P. (1960). "The relationship between wave action and beach profile characteristics." In: *Coastal Engineering Proceedings* 1.7.

Khoury, A., Jarno, A., and Marin, F. (2019). "Experimental study of runup for sandy beaches under waves and tide." In: *Coastal Engineering* 144, 33 –46.

Kobayashi, N., Santos, F. J. de los, and Kearney, P. G. (2008). "Time-averaged probabilistic model for irregular wave runup on permeable slopes." In: *Journal of waterway, port, coastal, and ocean engineering* 134.2, 88–96.

Kreyenschulte, M., Schürenkamp, D., Bratz, B., Schüttrumpf, H., and Goseberg, N. (2020). "Wave Run-Up on Mortar-Grouted Riprap Revetments." In: *Water* 12.12, 3396.

Kroon, A., Schipper, M. A. d., Gelder, P. H.A.J.M. v., and Aarninkhof, S. G. J. (2020). "Ranking uncertainty: Wave climate variability versus model uncertainty in probabilistic assessment of coastline change." In: *Coastal Engineering* 158, 103673.

Lakehal, D. and Liovic, P. (2011). "Turbulence structure and interaction with steep breaking waves." In: *Journal of Fluid Mechanics* 674, 522–577.

Lara, J. L., Losada, I. J., and Guanche, R. (2008). "Wave interaction with low-mound breakwaters using a RANS model." In: *Ocean engineering* 35.13, 1388–1400.

Lara, J. L., Losada, I. J., Maza, M., and Guanche, R. (2011). "Breaking solitary wave evolution over a porous underwater step." In: *Coastal Engineering* 58.9, 837–850.

Le Méhauté, B. (1976). *An introduction to hydrodynamics and water waves*. Springer Science & Business Media.

Lin, C.-Y. and Huang, C.-J. (2004). "Decomposition of incident and reflected higher harmonic waves using four wave gauges." In: *Coastal engineering* 51.5, 395–406.

Lira-Loarca, A., Baquerizo, A., and Longo, S. (Feb. 2, 2019). "Interaction of Swell and Sea Waves with Partially Reflective Structures for Possible Engineering Applications." In: *Journal of Marine Science and Engineering* 7.2, 31.

Longuet-Higgins, M. S. and Stewart, R. w (1964). "Radiation stresses in water waves; a physical discussion, with applications." In: *Deep Sea Research and Oceanographic Abstracts* 11.4, 529 –562.

Longuet-Higgins, M. S. (1978). "The instabilities of gravity waves of finite amplitude in deep water I. Superharmonics." In: *Proceedings of the Royal Society of London. A. Mathematical and Physical Sciences* 360.1703, 471–488.

Losada, I. J., Losada, M. A., and Martín, F. L. (1995). "Experimental study of wave-induced flow in a porous structure." In: *Coastal Engineering* 26.1, 77–98.

Losada, I. J., Patterson, M. D., and Losada, M. A. (1997). "Harmonic generation past a submerged porous step." In: *Coastal Engineering* 31.1, 281 –304.

Losada, M., Díaz-Carrasco, P., Moragues, M., and Clavero, M. (2019). "Variabilidad intrínseca en el comportamiento de los diques rompeolas." In: *Proceedings of the 15th National Conference of Jornadas Españolas de Puertos y Costas, Torremolinos (Spain)*, pp. 8–9.

Losada, M. A., Roldan, A. J., and Dalrymple, R. A. (1994). "Eigenfunction analysis of water wave propagation down a wave flume." In: *Journal of Hydraulic Research* 32.3, 371–385.

Losada, M. A. and Giménez-Curto, L. A. (1981). "Flow characteristics on rough, permeable slopes under wave action." In: *Coastal Engineering* 4, 187–206.

López, C. (1998). "Influencia de la reflexión del oleaje en la estabilidad de diques en talud." PhD thesis. Universidad de Granada.

Madsen, P. A. and Fuhrman, D. R. (2008). "Run-up of tsunamis and long waves in terms of surf-similarity." In: *Coastal Engineering* 55.3, 209–223.

Mansard, E. P. D. and Funke, E. R. (1980). "The Measurement of Incident and Reflected Spectra Using a Least Squares Method." In: *Proceedings of the 17th International Conference on Coastal Engineering*. Sydney, Australia, pp. 154–172.

Manual, S. P. (1984). *Shore Protection Manual*. Vol. Coastal Engineering Research Center (US). Department of the Army, Waterways Experiment Station, Corps of Engineers

Martins, K., Blenkinsopp, C. E., Deigaard, R., and Power, H. E. (2018). "Energy Dissipation in the Inner Surf Zone: New Insights From LiDAR-Based Roller Geometry Measurements." In: *Journal of Geophysical Research: Oceans* 123.5, 3386–3407.

Mase, H. (1989). "Random wave runup height on gentle slope." In: *Journal of Waterway, Port, Coastal, and Ocean Engineering* 115.5, 649–661.

Mase, H. and Iwagaki, Y. (1984). "Run-up of random waves on gentle slopes." In: *Proceedings 19th International Conference on Coastal Engineering*. 19th International Conference on Coastal Engineering. Houston (USA), pp. 593–609.

Maza, M., Lara, J. L., and Losada, I. J. (2013). "A coupled model of submerged vegetation under oscillatory flow using NavierStokes equations." In: *Coastal Engineering* 80, 16–34.

McLean, J. W., Ma, Y. C., Martin, D. U., Saffman, P. G., and Yuen, H. C. (Mar. 1981). "Three-Dimensional Instability of Finite-Amplitude Water Waves." In: *Phys. Rev. Lett.* 46.13, 817–820.

Melby, J. (2012). *Wave runup prediction for flood hazard assessment*. ERDC/CHL TR-12-24. US Army Engineer R&D Center.

Melville, W. K. (1982). "The instability and breaking of deep-water waves." In: *Journal of Fluid Mechanics* 115, 165–185.

Miche, M. (1951). "Le pouvoir réfléchissant des ouvrages maritimes exposés à l'action de la houle." In: *Annales de Ponts et Chaussées, 121 (285-319)*.

Miche, R. (1944). "Mouvements ondulatoirs des mers en profondeur constante on decroissant." In: *Annals des Points et Chausses, 1U* 2, 25–78.

Moragues, M. V. and Losada, M.. (2021). "Progression of Wave Breaker Types on a Plane Impermeable Slope, Depending on Experimental Design." In: *Journal of Geophysical Research: Oceans* 126, e2021JC017211.

Moragues, M. V., Díaz-Carrasco, P., Clavero, M., and Losada, M.. (2018). "Análisis del rebase sobre diques de abrigo." In: *UHINAK 2018.* 74.

Moragues, M. V., Díaz-Carrasco P., P., Clavero Maria, M., Ortega-Sánchez, M, and Losada, M.. (2019a). "Climate change impact on the hydraulic performance of breakwaters." In: E-proceedings of the 38th IAHR World Congress. Panama City, Panama.

Moragues, M. V., Clavero, M., Diaz-Carrasco, P., and Losada, M. A. (2020a). "Bulk dissipation and flow characteristics in cube armored breakwaters." In: *Proceedings of the 36th International Conference of Coastal Engineering* 36, 40–40.

Moragues, M., Clavero, M., and Losada, M. (2020b). "Wave breaker types on a smooth and impermeable 1:10 slope." In: *Journal of Marine Science and Engineering* 8.4, 296.

Moragues, M., Díaz-Carrasco, P., Clavero, M., and Losada, M.. (2019b). "Sobre el máximo remonte y rebase potencial en diques rompeolas." In: *Proceedings of the 15th National Conference of Jornadas Españolas de Puertos y Costas. Málaga, Spain*.

Muttray, M., Oumeraci, H., and Oever, E. t. (2006). "Wave reflection and wave run-up at rubble mound breakwaters." In: *Proceedings of the 30th International Conference on Coastal Engineering*. International Conference on Coastal Engineering. San Diego (USA), pp. 4314–4324.

Peregrine, D. H. (1983). "Breaking Waves on Beaches." In: *Annual Review of Fluid Mechanics* 15.1, 149–178.

Pinault, J., Morichon, D., and Roeber, V. (2020). "Estimation of Irregular Wave Runup on Intermediate and Reflective Beaches Using a Phase-Resolving Numerical Model." In: *Journal of Marine Science and Engineering* 8.12, 993.

Plant, N. G. and Stockdon, H. F. (2015). "How well can wave runup be predicted? Comment on Laudier et al. (2011) and Stockdon et al. (2006)." In: *Coastal Engineering* 102, 44 –48.

Polubarinova-Kochina, P (1962). *Theory of Ground Water Movement*. Princeton, NJ, USA: Princeton University Press.

Pérez-Romero, D. M. (2008). "Procesos hidrodinámicos en diques mixtos y efectos de escala." PhD thesis. Universidad de Granada.

Pérez-Romero, D. M., Ortega-Sánchez, M., Moñino, A., and Losada, M. A. (2009). "Characteristic friction coefficient and scale effects in oscillatory porous flow." In: *Coastal Engineering* 56.9, 931–939.

Rapp, R. J. and Melville, W. K. (1990). "Laboratory measurements of deep-water breaking waves." In: *Philosophical Transactions of the Royal Society of London. Series A, Mathematical and Physical Sciences* 331.1622, 735–800.

Requejo, S., Vidal, C., and Losada, I. (2002). "Modelling of wave loads and hydraulic performance of vertical permeable structures." In: *Coastal Engineering* 46.4, 249–276.

Sawaragi, T., Iwata, K., and Kobayashi, M. (1982). "Condition and probability of occurrence of resonance on steep slopes of coastal structures." In: *Coastal engineering in Japan* 25.1, 75–90.

Silva, P. Gomes da, Medina, R., Gonzalez, M., and Garnier, R. (2019). "Wave reflection and saturation on natural beaches: The role of the morphodynamic beach state in incident swash." In: *Coastal Engineering* 153. Publisher: Elsevier, 103540.

Sivanesapillai, R., Steeb, H., and Hartmaier, A. (2014). "Transition of effective hydraulic properties from low to high Reynolds number flow in porous media." In: *Geophysical Research Letters* 41.14, 4920–4928.

Sollitt, C. K. and Cross, R. H. (1972). "Wave Transmission through Permeable Breakwaters." In: *Proc., 13th International Conference on Coastal Engineering*. Vancouver, Canada: ASCE, pp. 1827–1846.

Sonin, A. A. (2001). "The physical basis of dimensional analysis." In: *Cambridge MA*.

Stagonas, D., Warbrick, D., Muller, G., and Magagna, D. (2011). "Surface tension effects on energy dissipation by small scale, experimental breaking waves." In: *Coastal Engineering* 58.9, 826 –836.

Stokes, G. (1847). "On the theory of oscillatory waves." In: *Transactions of the Cambridge Philosophical Society* 8.441.

Takahashi, S. (1996). "Design of vertical breakwaters." In: *Port and Airport Research Institute, Japan* Document nž34.

Ting, F. C. and Kirby, J. T. (1995). "Dynamics of surf-zone turbulence in a strong plunging breaker." In: *Coastal Engineering* 24.3, 177–204.

– (1996). "Dynamics of surf-zone turbulence in a spilling breaker." In: *Coastal Engineering* 27.3, 131–160.

Van Der Meer, J. W. (1988). "Rock slopes and gravel beaches under wave attack." PhD thesis. Delft: Delft University of Technology.

– (1992). "Conceptual design of rubble mound breakwaters." In: *Proceeding of a short course on the design and reliability of coastal structures, attached to 23rd Conference of Coastal Engineering.* Short course on the design and reliability of coastal structures,

attached to 23rd Conference of Coastal Engineering. Venice (Italy): Tecnoprint, pp. 447–510.

Van Der Meer, J. W. and Stam, C.-J. M. (1992). "Wave runup on smooth and rock slopes of coastal structures." In: *Journal of Waterway, Port, Coastal, and Ocean Engineering* 118.5, 534–550.

Van Gent, M. R. (2001). "Wave runup on dikes with shallow foreshores." In: *Journal of Waterway, Port, Coastal, and Ocean Engineering* 127.5, 254–262.

Van Gent, M. R. A. (1995). "Wave interaction with permeable coastal structures." PhD thesis. Delft: Delft University of Technology.

Vílchez, M., Clavero, M., Lara, J. L., and Losada, M. A. (2016a). "A characteristic friction diagram for the numerical quantification of the hydraulic performance of different breakwater types." In: *Coastal Engineering* 114, 86–98.

Vílchez, M., Clavero, M., and Losada, M. A. (2016b). "Hydraulic performance of different non-overtopped breakwater types under 2D wave attack." In: *Coastal Engineering* 107, 34–52.

Vílchez, M. (2016). "Unified design method of maritime works against waves." PhD thesis. Universidad de Granada.

Wei, Z., Li, C., Dalrymple, R. A., Derakhti, M., and Katz, J. (2018). "Chaos in breaking waves." In: *Coastal Engineering* 140, 272 –291.

Zanuttigh, B. and Meer, J. W.v. d. (2008). "Wave reflection from coastal structures in design conditions." In: *Coastal Engineering* 55.10, 771 –779.

Zelt, J. A. and Skjelbreia, J. E. (1992). "Estimating Incident and Reflected Wave Fields Using an Arbitrary Number of Wave Gauges." In: *Proceedings of the 23rd International Conference on Coastal Engineering*. 23rd International Conference on Coastal Engineering. Venice (Italy), pp. 777–789.

Zhang, Q. and Liu, P. L.-F. (2008). "A numerical study of swash flows generated by bores." In: *Coastal Engineering* 55.12, 1113–1134.